Novel InP-based Quantum Dots via ZnO Shelling and Ruthenium Doping for Lighting and Antibacterial Applications

by

Güncem Özgün Eren

A Dissertation Submitted to the
Graduate School of Sciences and Engineering
in Partial Fulfillment of the Requirements for
the Degree of

Doctor of Philosophy

in

Biomedical Sciences and Engineering

KOÇ ÜNİVERSİTESİ

July 26, 2023

Novel InP-based Quantum Dots via ZnO Shelling and Ruthenium Doping for Lighting and Antibacterial Applications

Koç University

Graduate School of Sciences and Engineering

This is to certify that I have examined this copy of a doctoral dissertation by

Güncem Özgün Eren

and have found that it is complete and satisfactory in all respects,

and that any and all revisions required by the final

examining committee have been made.

Committee Members:

_____

Assoc. Prof. Sedat Nizamoğlu (Advisor)

_____

Assoc. Prof. Umut Aydemir

_____

Prof. Erdem Alaca

_____

Assoc. Prof. Caner Ünlü

_____

Assoc. Prof. Onur Ferhanoğlu

Date: _____

To my wonderful wife Şule…

ABSTRACT

Novel InP-based Quantum Dots via ZnO Shelling and Ruthenium Doping for Lighting and Antibacterial Applications

Güncem Özgün Eren
Doctor of Philosophy in Biomedical Sciences and Engineering
July 26, 2023

Semiconductor colloidal quantum dots (QDs) have been at the focus of attention in recent years due to their advantageous properties, including emission tunability by quantum confinement effect and material composition, high photoluminescence quantum yield (PLQY), and chemical stability. Thus, QDs are regarded as ideal materials for a wide variety of applications such as light-emitting diodes (LEDs) and photocatalysis.

In the first part of our thesis, we demonstrated highly efficient quasi-type-II InP/ZnO/ZnS core/shell QDs with a PLQY of 91%. It is generally accepted perspective that type-II core/shell QDs, in which electron and hole wavefunctions are spatially separated, exhibit low PLQY. Even though type-II QDs with high PLQY values have been reported recently, they consist of heavy metals which show toxic effects. In our study, we used environmentally benign InP-based QDs as an alternative material compared to cadmium counterparts. After the synthesis of InP core QDs, we grew ZnO shell by thermal decomposition process to obtain type-II heterostructure. Subsequently, multiple ZnS shells were grown by SILAR technique. We integrated as-synthesized core/shell QDs on blue LED die using a novel architecture in liquid-state to minimize the host material effect. The resulting QD-LED exhibited external quantum efficiency (EQE) of 9.4%.

In the second part of thesis, we introduced for the first-time ruthenium doping into InP/ZnS QDs as alternative strategy for efficient red-emitters. To date, various transition metals doping into InP QDs have been investigated, however, ruthenium (Ru) ion doping into InP QDs has not been explored yet. In our study, we synthesized Ru doped InP QDs by hot injection of ruthenium precursor into main solution at elevated temperature. Ru presence was confirmed by optical and structural analysis techniques. Ru doped InP-based QDs displayed higher PLQY in the red spectral region compared to undoped sample. The integration of Ru-doped QDs into LEDs in a liquid matrix led to an external quantum efficiency of 7.9%.

In the last part of thesis, we investigated the potential of InP/ZnO core/shell QDs with type-II band alignment as a novel antibacterial agent. To date, various types of colloidal QDs have been introduced for antibacterial applications, including InP, ZnO, and CdTe. However, antibacterial activity of the type-II based QDs have not been studied yet. In our study, we demonstrated that InP/ZnO QDs exhibited reactive oxygen species (ROS) generation, including superoxide ($^{\bullet}O_2^-$) and hydroxyl radicals ($^{\bullet}OH$). Furthermore, upon low intensity green light stimulation (3 $mW.cm^{-2}$) the optimized core/shell QDs displayed high antibacterial activity of 99% inhibition against *Pseudomonas aeruginosa.*

These findings showed novel InP-based QDs via ZnO shelling and ruthenium doping are efficient material for LED and antibacterial applications.

ÖZET

Aydınlatma ve Antibakteriyel Uygulamalar İçin ZnO Kabuk Kaplamalı ve Rutenyum Doplu Yeni InP Tabanlı Kuantum Noktalar

Güncem Özgün Eren
Biyomedikal Bilimler ve Mühendislik, Doktora
Temmuz 26, 2023

Yarı iletken kolloidal kuantum noktaları (QD), kuantum hapsetme etkisi ve malzeme bileşimi ile emisyon ayarlanabilirliği, yüksek fotolüminesans kuantum verimi (PLQY) ve kimyasal stabilite dahil olmak üzere avantajlı özellikleri nedeniyle son yıllarda ilgi odağı olmuştur. Bu nedenle, kuantum noktalar, ışık yayan diyotlar (LED'ler) ve fotokataliz gibi çok çeşitli uygulamalar için ideal malzemeler olarak kabul edilmektedir.

Bu tez çalışmamızın ilk kısmında %91 gibi yüksek PLQY değerine sahip yarı tip-II InP/ZnO/ZnS çekirdek/kabuk kuantum noktaları gösterdik. Genel kabul görüşe göre elektron deşik dalga boylarının kısmen ayrıldığı tip-II yapısındaki QD'lar düşük PLQY değerine sahiptir. Bu konuda son yıllarda yüksek kuantum verimliliğine sahip tip-II kuantum noktalar rapor edilmiş olsa da toksik etkiye sahip kadmiyum içermektedirler. Bu bağlamda, çalışmamızda kadmiyum içerikli benzerlerine alternatif olarak çevreye zararsız InP tabanlı QD'ler gösterilmiştir. InP çekirdek QD'lerinin sentezinden sonra, tip II heteroyapı elde etmek için ZnO kabuğunu termal ayrıştırma işlemiyle büyüttük. Daha sonra, SILAR tekniği ile çoklu ZnS kabuklarını büyüttük. Ana malzeme etkisini en aza indirgemek için sentezlenmiş olan QD'leri yeni tip dizayn kullanılarak mavi LED'lere entegre ettik. Ortaya çıkan kuantum nokta tabanlı LED'in dış kuantum verimliliği (EQE) %9.4 olarak ölçüldü.

Tez çalışmamızın ikinci kısmında verimli kırmızı yayıcılar için alternatif bir yöntem olarak InP/ZnS QD'lere rutenyum katkılanması ilk kez incelenmiştir. Şimdiye kadar, çeşitli geçiş metallerinin InP kuantum noktalarına doplanması araştırılmış olsa da rutenyum doplanması henüz rapor edilmemiştir. Çalışmamızda, rutenyum doplu InP QD'ler rutenyum solüsyonunun yüksek sıcaklıkta ana solüsyona sıcak enjeksiyonu ile sentezledik. Rutenyum elementi çeşitli karakterizasyon teknikleriyle doğrulandı. Ayrıca, rutenyum doplu örneğin dopsuz olana kıyasla daha yüksek PLQY değerine ve QD tabanlı LED cihazının %7.9 verimliliğe sahip olduğu görüldü.

Tez çalışmamızın son kısmında ise yeni bir antibakteriyel malzeme olarak yarı tip-II InP/ZnO QD'ler araştırıldı. Bugüne kadar, antibakteriyel uygulamalar için InP, çinko oksit (ZnO) ve kadmiyum telerat (CdTe) gibi QD'ler araştırılmış olsa da tip-II QD'lerin antibakteriyel özellikleri rapor edilmemiştir. Bu bağlamda, ilk kez tez çalışmamızda InP/ZnO QD'lerin süperoksit ($^{\bullet}O_2^-$) ve hidroksil ($^{\bullet}OH$) radikalleri olmak üzere reaktif oksijen türleri (ROS) ürettiğini gösterdik. Ayrıca düşük yoğunluklu yeşil ışık uyarılması altında *Pseudomonas aeruginosa*'ya karşı %99 düzeyinde antibakteriyel etki gösterdiği tespit edildi.

Sonuç olarak bu tez çalışması ile ZnO kabuk kaplaması ve rutenyum doplama yoluyla yeni InP tabanlı QD'lerin LED ve antibakteriyel uygulamalar için etkili malzemeler olduğu gösterilmiştir.

ACKNOWLEDGMENTS

First of all, I would like to start by thanking Prof. Sedat Nizamoğlu, my supervisor and the head of Innovative DEvices and interfAces LABoratory (IDEALAB) at Koç University. I am incredibly fortunate to have the opportunity to work in his lab for the past five years. Not only did he provide me with such a lab environment with high standards, but he also constantly helped me with endless support, knowledge, and patience throughout my PhD. Being a member of his group is truly an honor for me, so I owe him many thanks.

I would also like to say many thanks to my beloved wife Şule for her limitless patience, understanding, and support throughout the five years at Koç University. Without her, I would never have come to this point. My sincere thanks also go to my parents who always support and encourage me to pursue my interests.

I would like to thank Assoc. Prof. Umut Aydemir and Prof. Erdem Alaca for valuable scientific discussions as my thesis committee members. I also sincerely thank Assoc. Prof. Caner Ünlü, and Assoc. Prof. Onur Ferhanoğlu for giving me the honor to be my thesis committee member and providing helpful suggestions and comments for improving the thesis.

I would like to express my gratitude to Prof. Alphan Sennaroğlu, Prof. Önder Metin, Prof. Cleva W. Ow-yang from Sabancı University, Prof. Mehmet Şahin from Abdullah Gül University, Prof. Füsun Can, Asst. Prof. Safacan Kölemen, Dr. Rainer T. Lechner from the University of Leoben, Dr. Işınsu Baylam, and Dr. Nazlı Ataç for their indispensable scientific contributions and helpful suggestions. I am also grateful to Dr. Hadi Jahangiri and Dr. Barış Yağcı from Koç University Surface Science and Technology Center (KUYTAM) and Dr. Gülcan Çorapçıoğlu from Koç University Nanofabrication and Nanocharacterization Center for Scientific and Technological Advanced Research (n^2STAR) for the measurements and characterization.

A special thanks to my former colleagues, especially, Dr. Houman Bahmani Jalali, Dr. Sadra Sadeghi, Dr. Rustamzhon Melikov, Dr. Onuralp Karatüm, Dr. Itır Bakış Doğru Yüksel, Dr. Erdost Yıldız, and Mertcan Han, who collaborated with me for publishing many papers. I also owe many thanks to my current group colleagues especially, Asım Önal, Lokman Kaya, Rıdvan Balamur, Saad Ullah Khan, Muhammad Hassnain, Hümeyra

Nur Kaleli, Tarık Safa Kaya for their efforts and contributions. I am also grateful to colleagues, Dr. Melek Şermin Özer, Dr. Zafer Eroğlu, and Buse Sündü who gave valuable efforts and suggestions to my papers.

I also would like to express my gratitude to Prof. Gönül Alpay Tekin from Harvard University and Prof. Günay Kut from Boğaziçi University. Despite their areas of expertise are totally different from my own, their moral support during PhD was irreplaceable.

Finally, I acknowledge the Scientific and Technological Research Council of Turkey (TUBITAK) (119F363), European Research Council (ERC, Grant Agreement 101045289), European Research Council (ERC Grant Agreement 639846), and Marie Skłodowska-Curie (STIMULUS, Grant Agreement 955664) for the financial support.

TABLE OF CONTENTS

LIST OF TABLES

LIST OF FIGURES

ABBREVIATIONS

QD	Quantum dot
PLQY	Photoluminescence quantum yield
LED	Light-emitting diode
LE	Luminous efficiency
LER	Luminous efficacy of radiation
PCE	Power conversion efficiency
EQE	External quantum efficiency
CCE	Color conversion efficiency
CCT	Correlated color temperature
CRI	Color rendering index
SSL	Solid-state lighting
CIE	Commission on illumination
FWHM	Full width at half maximum
ML	Monolayer
XRD	X-ray diffraction
SAXS	Small angle x-ray scattering
XPS	X-ray photoelectron spectroscopy
TAS	Transient absorption spectroscopy
TEM	Transmission electron microscopy
SEM	Scanning electron microscopy
HRTEM	High-resolution transmission electron microscopy
EDX	Energy dispersive x-ray
ICP-MS	Inductively coupled plasma mass spectroscopy
STEM	Scanning transmission electron microscopy
SILAR	Successive ionic layer adsorption and reaction
TRPL	Time-resolved photoluminescence
ROS	Reactive oxygen species
DFT	Density functional theory
PDMS	Polydimethylsiloxane
MTT	3-(4,5-dimethylthiazol-2-yl)-2,5-diphenyltetrazolium bromide
XTT	sodium 3′-[1-[(phenylamino)carbonyl]-3,4-tetrazolium]-bis(4-methoxy-6-nitro)benzene sulfonic acid hydrate

Chapter 1: Introduction

Solid-state lighting (SSL) sources such as light-emitting diodes (LEDs) are developing energy-efficient lighting technologies due to their high brightness, long operational lifetime, and low energy consumption. The utilization of this technology has a large potential impact on energy saving and it is assumed that by replacing LEDs with conventional lighting technologies such as incandescent bulbs or fluorescent lamps the global electricity which is consumed for lighting would be reduced more than 50% [1]. The global LED lighting market grew by 3.2% from 2018 to almost 60BEuro in 2019 [2]. Thus, it is expected that LEDs will dominate the majority of lighting technologies in the near future. According to the US Department of Energy, by transition to LED technology energy savings will be around 40% by 2030. Currently, phosphors which are made of rare-earth ions are mostly used as down conversion materials in solid-state LED application. However, they lack of tunable and large emission bandwidth, which decreases the efficiency of the LEDs at near infrared wavelength region where the human eye is not sensitive anymore [3]. Hence, the need for finding alternative materials which possess narrow emission bandwidth and tunable luminescence for efficient LEDs continues.

Bacterial infections pose a global threat to public health and cause severe economic issues [4, 5]. Since their discovery in the twentieth century, antibiotics have been extensively used againts bacterial infections due to their highly effective bactericidal ability and low toxicity to host cells [6]. However, in recent times, the misuse of antibiotics together with the rapid mutation and evolution of bacteria caused the emergence of resistance in these microorganisms. According to a recent report of The World Health Organization (WHO), nearly 700,000 deaths are caused by antibiotic-resistant bacteria every year [7] and it is predicted that this number will increase to 10 million by 2050 [8]. Therefore, considerable research against antibiotic-resistant bacteria has been conducted [9]. However, in the last 20 years, only two new classes of antibiotics were approved by international regulatory agencies [10]. Semiconductor-mediated photocatalysis is based on production of reactive species (ROS) and it is considered as a promising and emerging modality in developing potential disinfection strategies against several hostile microorganisms [4, 11]. To date, titanium dioxide (TiO_2) has been proven to be an effective semiconductor photocatalyst

in various studies [12]. However, it can only be excited by ultra-violet or near ultra-violet due to its high bandgap (3.2 eV). As a result, the search of novel materials which have tunable emission is a key requisite.

Colloidal quantum dots (QDs) offer great potential for LED and photocatalysis applications due to their tunable emission bandwith, high photoluminescence quantum yield (PLQY), thermal and photostability properties [13-16]. For QD-based LED applications, reabsorption and integration of QDs affect the efficiency of the final device. In order to address the host material effect issue, one possible solution is the direct integration of as-synthesized QDs into the LED architecture. On the other hand, to obtain low reabsorption loss, it is important to separate the absorbance and emission peak by chosing appropiate core/shell heterostructure (type-II) or doping of host nanostructure with numerous transition metals. It is generally accepted perspective that type-II core/shell QDs, in which electron and hole wavefunctions are spatially separated, exhibits low PLQY. Even though, in recent times, colloidal type-II QDs with high PLQY were reported in previous studies, they possess disadvantages such as consisting of cadmium as heavy-metal [17, 18]. Instead, indium phosphide (InP) offers great potential as an environmentally benign and non-toxic host material for QD-based LED technologies. Transition metal doping of colloidal QDs also leads to high PLQY, reduced self-absorption and longer luminescence lifetime. To date, there are various transition metals such as copper (Cu) [19] and silver (Ag) [20] are doped into InP crystal structure. However, ruthenium which is a widely used in supercapacitors [21], catalysis [22], and optoelectronic neural interfaces [21] have not been reported yet.

More recently, colloidal QDs have gained significant interest as potential semiconducting materials to combat antibiotic-resistant bacteria. To date, various types of QDs such as InP [15], CdSe [23], and $AgBiS_2$ [24] have been demonstrated as effective ROS generators. However, the effect of type-II QDs on antibacterial activity has not been explored yet.

This thesis demonstrates the synthesis of InP-based QDs and utilization in 2 different applications: (1) light-emitting devices (LEDs), (2) antibacterial application. The organization of the thesis is as follows:

In the first chapter of the thesis, we make an introduction about colloidal quantum dots (QDs) and their light-emitting diodes (LEDs) and photocatalysis-based antibacterial applications.

In the second chapter of the thesis, we provide the basic background knowledge about colloidal QDs, including the synthesis methods, optical and structural properties. Afterwards, we continue with QD-based LEDs and the corresponding working mechanisms, optical analysis and measurement techniques. Finally, we focus on photocatalysis mechanism and antibacterial application of colloidal QDs.

In the third chapter, we cover InP-based QDs. In this regard, we provide background knowledge about the synthesis methods, surface chemistry, and defect states of InP QDs. We also describe InP-based core/shell QDs and biocompatibility properties.

In the fourth chapter of the thesis, we describe our study which is based on InP-based type-II core/shell QDs and their LED application. We first focus on highly efficient cadmium-free InP/ZnO/ZnS QDs' optical and structural properties, followed by QD-LED device efficiency fabrication and measurement.

In the fifth chapter, we introduce our study about ruthenium doped InP-based QDs and LED application for efficient red-emission. We first demonstrate the effect of ruthenium dopant incorporation on optical and structural properties of InP QDs. We also investigated the effect of ruthenium presence on PLQY of QDs in the red spectral region. Then, we demonstrated ruthenium doped InP-based QD-LED device fabrication and characterization.

In the sixth chapter of the thesis, we demonstrated for the first time quasi-type-II InP/ZnO core/shell QDs with multiple ZnO shells as efficient photocatalysts for the generation of reactive oxygen species (ROS). Following the ligand exchange process, we also examine the ZnO shell effect on the ROS efficiency of sulfide capped InP/ZnO core/shell QDs. Finally, we showed antibacterial activity of the optimized QDs against *Pseudomonas aeruginosa* upon stimulation with low intensity green light.

In the seventh chapter, we conclude our thesis by describing and remarking our achievements.

Chapter 2: Scientific Background

2.1 Colloidal Quantum Dots

Colloidal quantum dots (QDs) are semiconductor nanocrystals, typically with a diameter in the range of 1-10 nanometers, which possess size, shape, and chemical-composition dependent 'quantum confinement effect' due to their small size comparing to bulk counterparts. In bulk semiconductors, the conduction and valence bands are separated by energy-gap. When the size of bulk semiconductor is decreased towards nanometer scale, the size of the crystal becomes smaller than the exciton Bohr radius (e.g. for ZnSe, CdSe, and InP QDs exciton Bohr radius values are 4.1 nm, 4.6 nm, and 10 nm, respectively). As a result, upon decreasing the nanocrystal size, the bandgap of the semiconductor increases and it leads to formation of discrete energy levels. Due to the quantum confinement effect, as the QD size decreases, the nanocrystal emits at shorter wavelengths (towards blue); however, as the QD size increases, the emitted light shifts towards the red region of the spectrum (Figure 2.1) [25]. Therefore, the bandgap tunability of these materials plays a vital role in the advancement and investigation of QDs-based optoelectronic and biomedical applications, including light-emitting diodes, photodetectors, lasers, solar cells, displays, transistors, photo-catalysis, neural photosimulation, imaging, sensing, and bio-labeling.

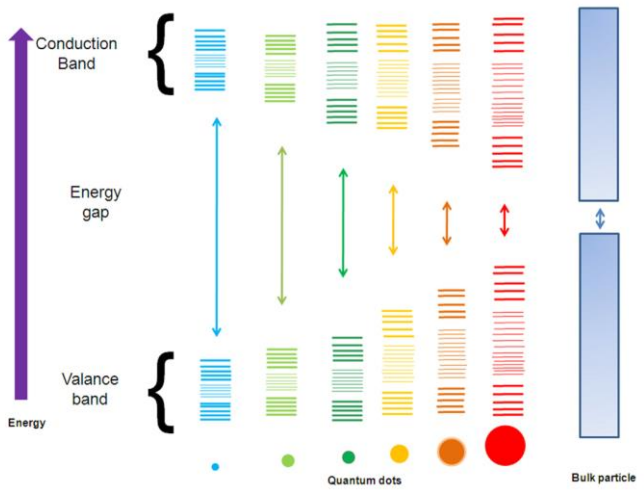

Figure 2. 1: The schematic representation of size tunable optical properties of quantum dots. As the quantum dot size increases emission wavelength shifts towards red spectral region [25].

Structurally, colloidal QDs consist of an inorganic semiconducting core, covered with an organic ligand shell (Figure 2.2) [26, 27]. Inorganic semiconducting core is constructed mostly by the III-V (e.g. InP, InAs), II-VI (e.g. CdSe, ZnSe), and IV-VI (e.g. PbS, PbSe) group nanocrystals. On the other hand, organic capping ligands which are used for QD synthesis are made up of head group and tail group. During colloidal QD synthesis organic ligands form a shell around nanocrystals. The head group binds to the nanocrystal surface and control the growth and size of the nanocrystals, whereas tail groups cause to repel each other, resulting in colloidal stability of formed nanocrystals.

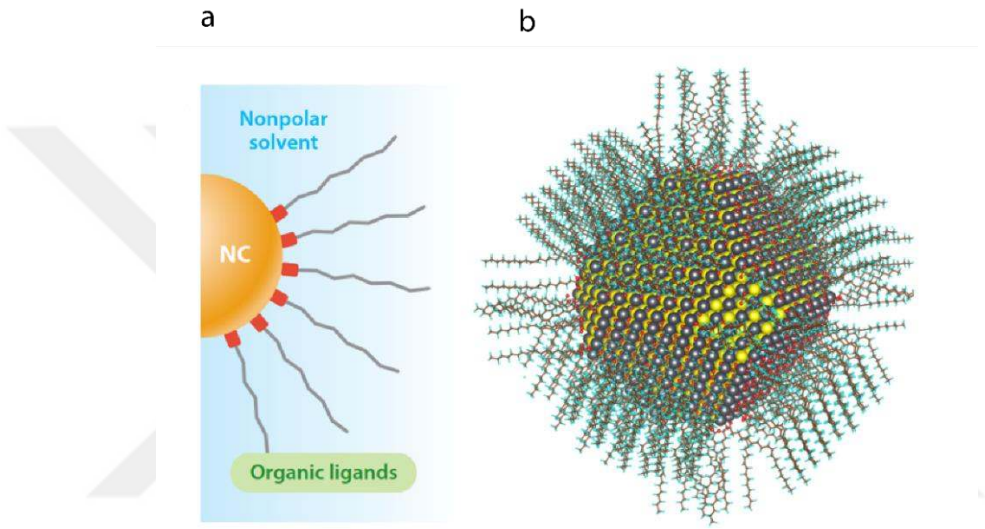

Figure 2. 2: (a) Schematic illustration of semiconductor QDs capped with organic ligand [27]. (b) A computational model of lead sulfide (PbS) QDs. The inorganic semiconducting core (PbS) is covered by organic ligands [26].

2.1.1 The nucleation and growth mechanism of colloidal QDs

In a wet-chemistry synthesis of colloidal QDs, the formation mechanism of nanocrystal is explained by LaMer model, which is typically divided into four stages: (1) monomer accumulation, (2) nucleation, and (3) growth. At the stage (1), the starting precursors generates smallest building blocks of nanocrystals, termed as monomers. When the monomer concentration exceeds a critical value ($C_{saturation}$), the nucleation starts to take place by collection of monomers in stage (2). At the stage (3), due to the nucleation process the consumption of the monomers occurs and the monomer concentration drops below critical saturation limit $C_{saturation}$. The remaining monomers deposit on the formed nanocrystals, termed as growth step. When the monomer concentration reaches

equilibrium value small nanocrystals start to dissolve and deposit on bigger nanocrystals, resulting in increase of polydispersity. This process is called 'Ostwald ripening' (Stage 4) (Figure 2.3) [28].

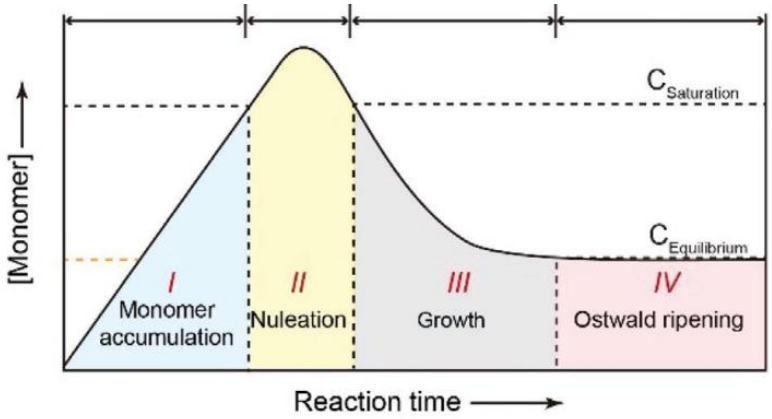

Figure 2. 3: Schematic drawing of a LaMer model for the colloidal QDs formation mechanism [28].

2.1.2 The synthesis of colloidal QDs

For the synthesis of colloidal QDs with various size, shape, and chemical compositons, the most common approaches are hot-injection, heat-up, co-precipitation, successive ionic layer adsorption and reaction (SILAR), and cation-exchange methods.

Hot injection technique

This technique is one of most widely used methods for the synthesis of high quality colloidal QDs. In a typical hot-injection technique, the precursor solution at room temperature is rapidly injected into a hot reaction solution. Therefore, monomer formation and nucleation process are initiated and be followed by growth of nanocrystals. Overall, the resulting QDs synthesized by hot-injection technique generally exhibit monodispersity, narrow size distribution, a relatively high photoluminescence quantum yield (PLQY), and colloidal, chemical, and photostability. Moreover, the size and morphology of synthesized QDs can be modified by optimizing reaction parameters such as injection temperature, precursor molar ratios, and surfactant selection (Figure 2.4) [28].

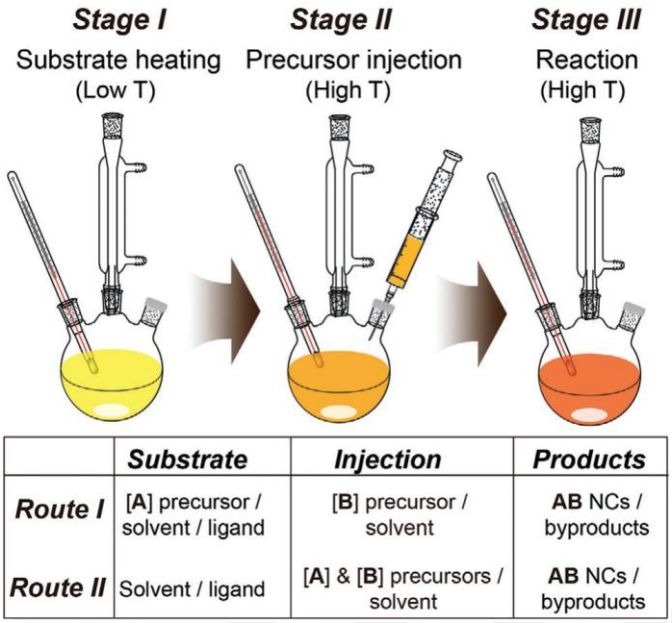

	Substrate	Injection	Products
Route I	[A] precursor / solvent / ligand	[B] precursor / solvent	AB NCs / byproducts
Route II	Solvent / ligand	[A] & [B] precursors / solvent	AB NCs / byproducts

Figure 2. 4: Schematic illustration of hot-injection technique for synthesis of colloidal QDs. In a typical hot-injection approach the precursor solution [B] at room temperature is quickly injected into a hot reaction solution [A] or injecting both [A] and [B] precursors into a hot medium. Therefore, monomer formation and nucleation process are initiated and be followed by growth of nanocrystals [28].

Heat-up method

Heat-up method is an alternative technique, in which all precursors containing metal salts, ligands, and solvents are mixed in a flask and the main solution is quickly heated to elevated temperature. In this technique, monomers are generated upon heating, followed by nucleation and growth steps. Comparing to hot-injection technique, the heat-up method is more reproducible and is easier to scale-up for large scale production (Figure 2.5) [29].

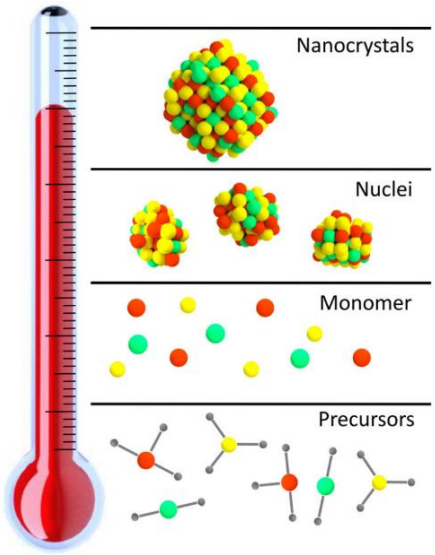

Figure 2. 5: Schematic illustration of heat-up technique [29].

SILAR technique

Successive ionic layer adsorption and reaction (SILAR) technique is commonly used to synthesize core/shell nanocrystal heterostructures. In this method, cation and anion precursor solutions are prepared at room temperature and subsequently added to the as-prepared QD core solution at elevated temperature. This approach allows us to control shell thickness by varying the precursor solution amounts. Therefore, giant core/shell QDs can be produced by SILAR method (Figure 2.6) [30].

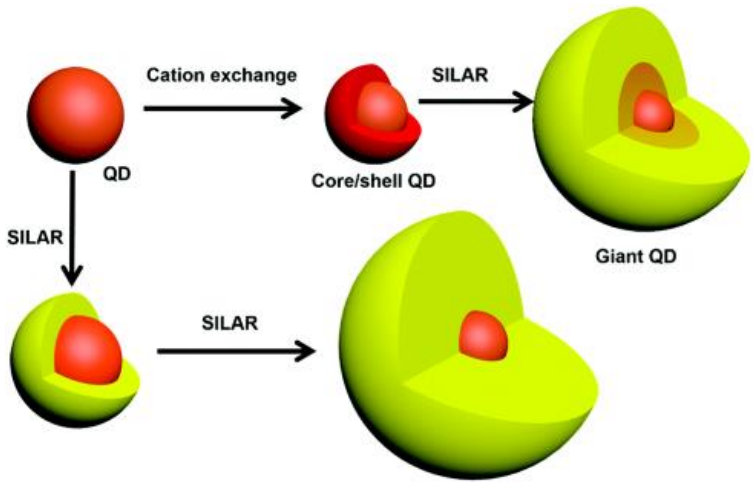

Figure 2. 6: Schematic representation of the synthesis of core/shell colloidal QDs by SILAR technique [30].

Co-precipitation technique

The co-precipitaion technique is generally used to synthesize ternary I–III–VI_2 (such as $CuInS_2$) semiconductors. Despite the sizes of QDs can be effectively controlled through the reaction temperature and time, the resulting QDs' size distribution produced by this approach becomes broader comparing to hot-injection technique due to continuous nucleation and growth process.

Cation exchange

In order to grow shell on core structure, cation exchange process can be used as an alternative technique. It is based on replacement of cation ions from main nanocrystal by guest ions dissolved in organic or aqueous solvent. This process specifically might be an option when the core and shell materials have large lattice mismatch. The solvation energy and Lewis acid-base interactions govern the cation exchange reaction. This method is used for different core/shell structures. For instance, Donega and co-workers synthesized ZnSe/CdSe QDs using cation exchange of Zn^{+2} by Cd^{+2} ion in colloidal ZnSe QDs [31].

2.1.3 Transition metal doped QDs

Doping of semiconductor nanocrystals with transition metals is attracting significant attention in various applications such as light-emitting diode (LED) [32, 33], luminescent solar concentrator (LSC) [34, 35] due to their unique, optical and magnetic properties [36]. For instance, a major feature in doped QDs is the Stokes-shift between emission and absorption peaks, which gives the doped nanocrystals with suppressed reabsorption property. Moreover, doping of QDs with transition metals causes separation of photogenerated electrons and hole wavefunctions, thus it leads to longer photoluminescence lifetime compared to pure host nanocrystals. In colloidal QD doping, dopant incorporation is governed by kinetics and thermodynamic. kinetics determines whether a dopant will incorporate into the host nanocrystals, while thermodynamics determine the doping mechanism of dopant ion. It should be also pointed out that in case of absence of a shell or the distance of the dopant location from the surface of QDs lattice diffusion and eventually lattice ejection of the dopants can occur upon thermal treatment [36]. General synthetic approaches of the doped nanocrystals are divided into three categories as (1) nucleation doping, (2) growth doping, and (3) ion diffusion doping.

Nucleation doping

In nucleation doping approach, all precursors including the dopant precursor are mixed during the nucleation step. Before host nanocrystals formation, dopant nucleate first. Then, core dopant nuclei are overcoated by host material. Pradhan *et al.* showed manganese doped zinc selenide (Mn:ZnSe) QDs using this technique. First, they synthesized MnSe nuclei 1-2 nm in diameter, then they added zinc precursor solution to grow ZnSe [37].

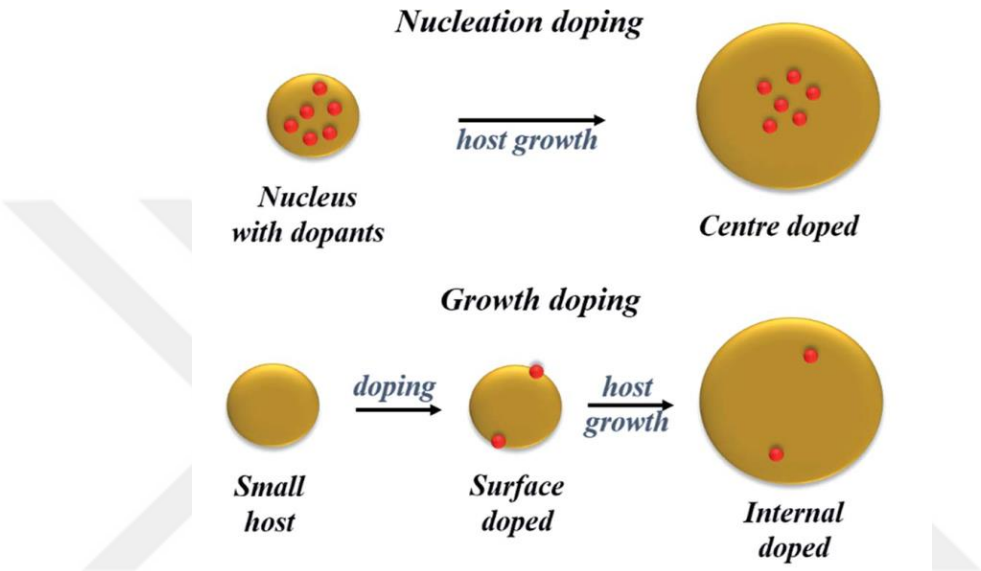

Figure 2. 7: Schematic drawing of nucleation and growth doping approaches [38].

Growth doping approach

In growth doping technique, host nanocrystals are formed before injection of dopant ions. Then, dopant precursor solution is added to adsorb the dopant ions on surface of QDs. Afterwards, the dopant ions are encapsulated by overgrowing of a shell. Pradhan *et al.* synthesized copper doped ZnSe (Cu:ZnSe) QDs using growth doping approach [37]. The same technique was also used by Gamelin and co-workers to obtain cobalt doped cadmium sulfide (Co:CdS) nanocrystals [39]. In that study, after formation of CdS nanocrystal, they injected Co dopant precursor to adsorb the dopant ions. Then, Co:CdS was encapsulated by an isocrystalline shell. Schematic illustration of nucleation and growth doping approaches is given in Figure 2.7 [38].

Ion diffusion doping

Ion diffusion doping is a particular case of growth doping. For the first time, Saha *et al.* designed a core shell material which consists of a small magnetic iron oxide core (Fe_3O_4) overcoated with a thick shell of semiconductor nanocrystal (CdS) [40]. After annealing of the core/shell structure at high temperature, iron (Fe) dopants diffused towards interface and semiconductor shell. As a result, uniformly doped Fe:CdS QD was produced. Chen et al. synthesized copper and manganese doped ZnSe QDs through ion diffusion doping. In that study, the injected dopant ions adsorb on the surface of QDs at relatively low temperature. Then, above a certain critical temperature, dopant ions diffuse into the crystal structure of the host nanocrystal (Figure 2.8) [41].

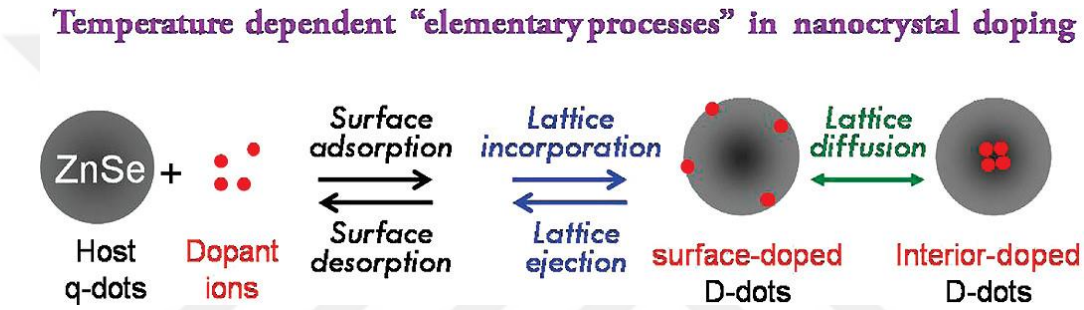

Figure 2. 8: Schematic illustration of temperature-dependent ion diffusion doping [41].

Cation exchange reactions, in which dopant cation is exchanged with host cation through diffusion mechanism are also applied for doping of nanocrystals. The extent of the cation exchange reactions can also be adjusted by changing the concentration of dopant ions and ligands present in the solution. Gamelin and co-workers investigated high-quality colloidal $Cd_{1-x}Mn_xSe$ nanocrystals by diffusion doping of preformed CdSe nanocrystals and they showed that diffusion of Mn ions into the host nanocrystal is governed by the excess amount of Se ions [42].

2.1.4 The optical properties of QDs

Exciton behavior in QDs

The fundamental exciton behaviors observed in colloidal QDs structures are illustrated in Figure 2.9. When a photon of excitation light is absorbed by a QD, an electron is excited from the valence band (occupied orbitals) to the conduction band (unoccupied orbitals) and it generates hot electron (hole) in conduction and valence bands as shown in 'Step 1'.

For hot electron and holes, there are two main pathways to take place. If the trap state energy levels are at proper positions, hot electron (hole) might be trapped by those states (illustrated as Step 5). These trap states may cause non-radiative recombination or may back-transfer the charge carriers (Step 6) to regenerate an exciton that can be followed by radiative (Step 3) or non-radiative electron-hole recombinations (Step 4). As a second possibility, hot electron and hole might relax to lowest unoccupied molecular orbital (LUMO) and highest occupied molecular orbital (HOMO) levels through Step 2 and form band-edge exciton. As a result, electron and hole may undergo recombination by radiative process, resulting in emitting a photon (emission) [43].

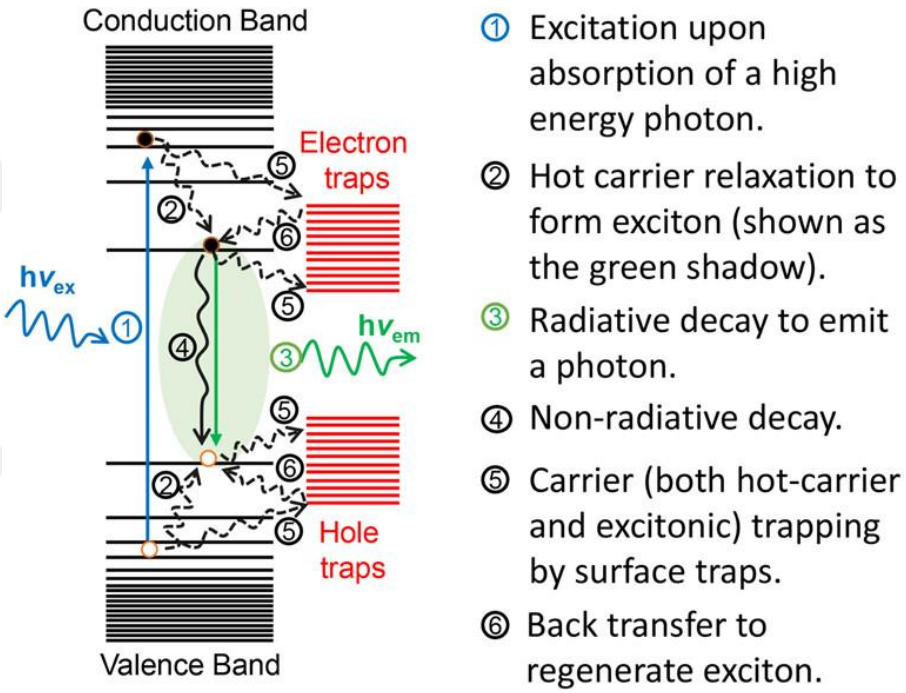

Figure 2. 9: Schematic illustration of fundamental exciton behavior in a QDs [43].

Absorbance, photoluminescence (PL) and photoluminescence quantum yield (PLQY)

The optical properties of QDs are size, shape, and composition-dependent. When the QD size decreases, the energy-gap increases, thus the ability to control the size of QDs yields size-dependent different colored nanocrystals. The smaller a QD, closer to the blue end of the spectrum. There are three main optical properties can be described for colloidal QDs: (1) absorbance, (2) emission, and (3) photoluminescence quantum yield (PLQY). These optical properties can be adjusted by synthesizing nanocrystals which have

different size, shape, and composition for specific applications. Typical absorbance and PL spectra of the QDs are demonstrated in Figure 2.10 [13].

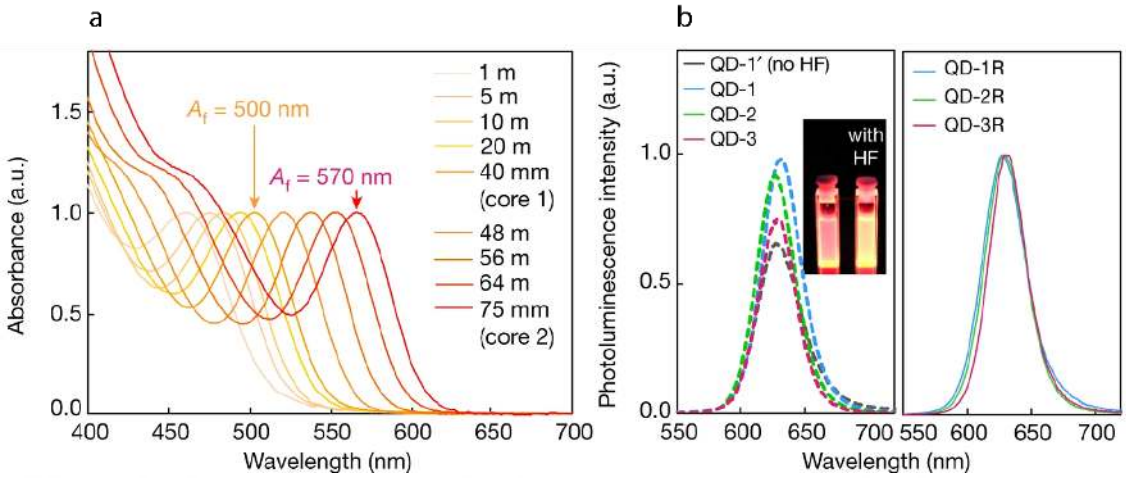

Figure 2. 10: (a) The absorbance of InP QDs; (b) PL emission of InP/ZnSe/ZnS core/shell/shell QDs sythesized by seed-assisted hot-injection method [13].

Photoluminescence quantum yield (PLQY) is defined as the ratio of number of emitted photons (per time and volume unit) relative to the number of absorbed photons. This metric is related to fluorescence efficiency of the QDs. If a QD contains surface trap states, it causes non-radiative losses, resulting in decrease of PLQY.

Fluorescence lifetime

The fluorescence lifetime is defined as average time a QD stays in its excited state before returning to the ground state upon excitation. In terms of formulation, this characteristic time of a QD is given by Equation (2.1).

$$\tau = \frac{1}{k_f + k_{nr}} \tag{2.1}$$

which τ corresponds to the average lifetime; whereas k_f and k_{nr} are radiative and non-radiative decay rates, respectively. Typical fluorescence lifetime of a ZnCdSe based QDs before and after surface treatment is given in Figure 2.11 [44].

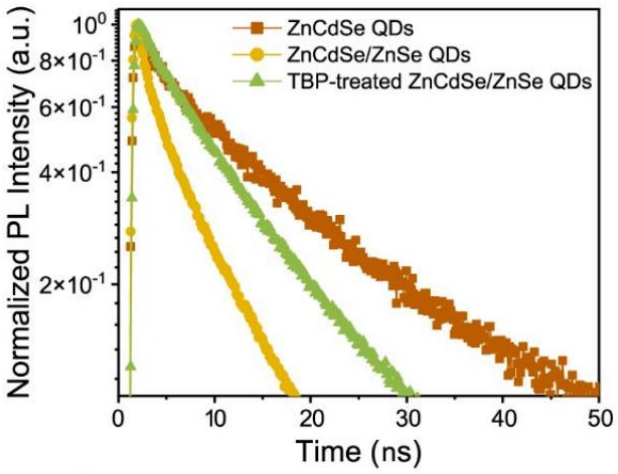

Figure 2. 11: The PL decay dynamics of ZnCdSe based QDs before and after treatment with tributylphosphine (TBP) [44].

Nonlinear absorption properties of QDs

Understanding the charge carrier dynamics in QDs is highly essential for their various applications. The mechanism of nonlinear absorption properties is analysed by transient absorption spectroscopy (TAS) measurement. This technique is based-on excitation of QD sample by two laser beams (probe and pump) and measurement of absorbance simultaneously. Basically, the high intensity pump laser beam is used to excite the QD to higher energy level, which alters the ground state population. Next, a white light probe laser is passed through the sample to measure the absorption. Therefore, the change in absorption which is related to charge carrier dynamics can be analysed by TAS technique. Schematic illustration of TAS measurement principle is shown in Figure 2.12 [45].

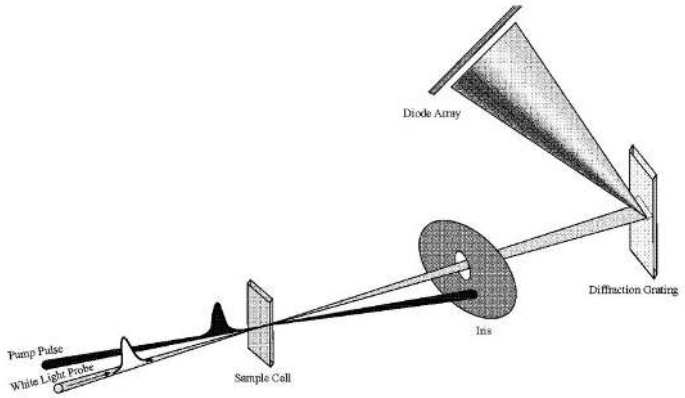

Figure 2. 12: Schematic illustration of TAS measurement principle [45].

Stokes-shift in QDs

One of the dominant factor that affects the efficiency of QD-based applications is reabsorption property which leads to energy loss. The Stokes-shift (red-shift) is the separation between the excitation and emission spectra of the QDs and it is one of the most important parameter that determine the optical properties of QDs for their applications. Several approaches have been proposed to decrease the reabsorption of QDs by Stokes-shift engineering [46-48]. For instance, Sadeghi et al. synthesized quasi-type II InP/ZnO core/shell QDs as non-toxic material and it has been shown that due to transition from a type-I to a quasi-type-II carrier localization the spectral emission and absorption overlap decreased [48]. Alternatively, Stokes-shift engineering is performed by doping the host material with variable transition metal ions such as copper (Cu), manganese (Mn) etc. [19, 49-51]. The represantation of Stokes-shift is given in Figure 2.13 [52].

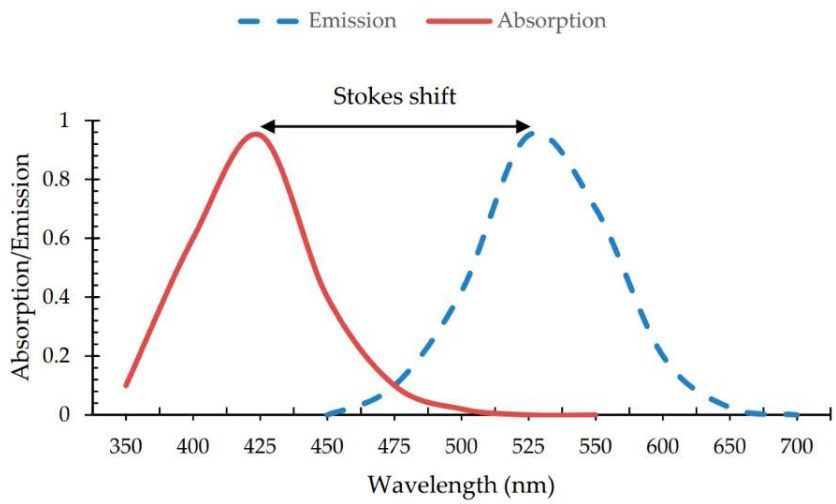

Figure 2. 13: The represantation of Stokes-shift observed in QDs [52].

Energy band alignment of core/shell QD

According energy band alignment of the conduction band valence band edges of the core and shell, semiconductor core/shell QDs are classified into three main subgroups as type-I, type-II, and reverse type-I heterostructures. In type-I structure, the bandgap of the core semiconductor is smaller than the bandgap of shell material, leading to confinement both electron and hole in the core region. For this type of heterostructures, shell is used to passivate the surface trap states of core structure to obtain high PLQY, high photo and

thermal stability for their applications such as LED. In type-I structures, emission is mainly dominated by the core due to localization of electron and hole in the core region. On the other hand, in type-II structures one of the band edges (either is valence or conduction band edge) of the shell is located in the bandgap of core semiconductor. This band alignment of the conduction and valence band edge leads to spatial separation of electron and hole wavefunctions, thus significant Stokes-shift can be observed with respect to type-I core/shell structures. For type-II structure, due to reduced overlap between electron and hole wavefunctions electrons and holes can be separated, which makes them excellent candidates for solar cell and photodetector applications. In the case of quasi-type-II configuration, one type of carrier is confined in the core; while the other carrier is delocalized entire core/shell QDs. Reverse type-I is the opposite of type-I structure, in which charge carriers are delocalized in the shell. An overview of energy band alignment of the core/shell heterostructured core/shell QDs is shown in Figure 2.14 [53].

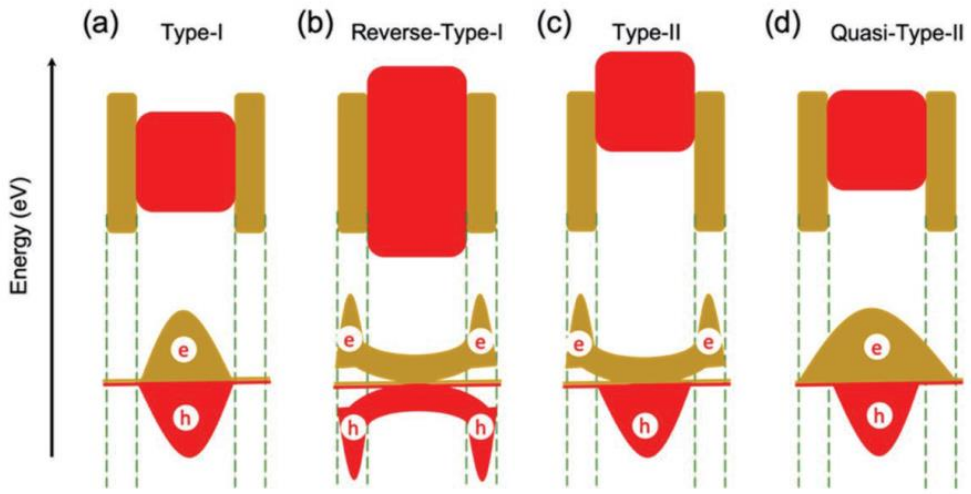

Figure 2. 14: Schematic represantation of band alignment for different type of core/shell structures [53].

2.1.5 Structural and optical characterization of QDs

Structural characterization of QDs

Semiconductor QDs exhibit different type of crystal structure such as zinc blende (e.g. InP, CdSe), wurtzite (e.g. CdS, ZnS), and perovskite crystal structure. In order to analyse the structural properties of QDs several characterization techniques are performed such

as X-ray diffraction (XRD), transmission electron microscopy (TEM), high-resolution transmission electron microscopy (HRTEM), X-ray photoelectron spectroscopy (XPS), inductively coupled plasma-mass spectroscopy (ICP-MS), inductively coupled plasma-atomic emission spectroscopy (ICP-AES), small angle X-ray scattering (SAXS). As an example, HRTEM images of ZnCdSe/ZnSe core/shell QDs and InAs/ZnSe core/shell QDs are demonstrated in Figure 2.15.

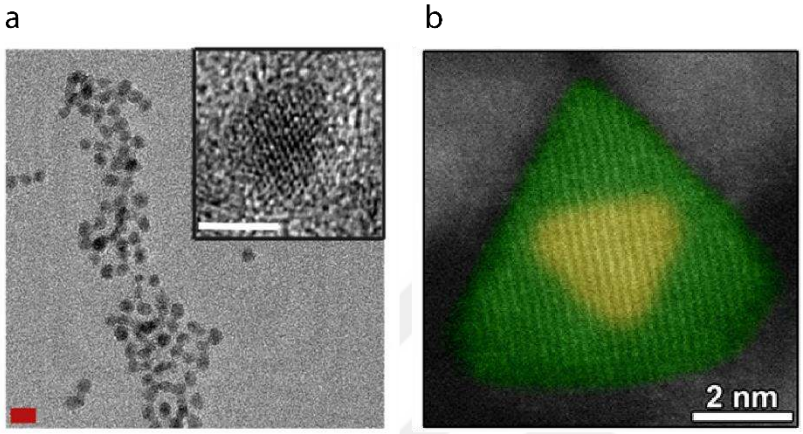

Figure 2. 15: HRTEM images of (a) ZnCdSe/ZnSe core/shell QDs [44]; (b) InAs/ZnSe core/shell QDs [54].

Optical characterization of QDs

The main optical properties including absorbance, PL emission, and PLQY of the QDs are measured steady-state optical analysis methods. For the photoluminescence lifetime measurement Picoquant MicroTime 100 Time-resolved Fluorescence Microscope was used. As excitation source, A PDL 800-D diode laser driver for picosecond pulses combined with a 375 nm laser head was used. The repetition rate was 8 MHz.

To characterize the nonlinear absorption properties, transient absorption spectroscopy (TAS) measurement is carried out. For TAS measurement, QDs were excited with 320 nm femtosecond pulses, generated with an optical parametric amplifier (MKS Spectra-Physics TOPAS), which was pumped with a regeneratively amplified Ti:sapphire laser delivering 120 fs pulses (MKS Spectra-Physics, Spitfire Ace).

2.2 Light-emitting diodes (LEDs)

Historical records about the incandescent light bulbs dates back to 18th century. As a revolutionary step, Thomas Edison invented electric light bulb, which transforms

electricity as the primary source for lighting. In 1962, Nick Holonyak, Jr. From General Electric invented the first red-emitting LED which is made up a semiconductor alloy gallium arsenide phosphide ($GaAs_{1-x}P_x$) [55]. In the following years, by great interest and research in the LED field came up with a groundbreaking achievement which is the first efficient InGaN/AlGaN based blue-emitting LED was produced by Nakamura, Akasaki, and Amano [56]. This breakthrough won the aforementioned researchers the 2014 Nobel Prize in Physics.

2.2.1 Quantum dot-based light-emitting diodes (QD-LEDs)

Quantum dot based light-emitting diodes (QD-LEDs) offer a lot of potential as next-generation color converters for displays and lighting sources. The working principle which is based on QD excitation mechanism of QD-LEDs is classified into two main group: (1) electroluminescent QD-LEDs, (2) photoluminescent QD-LEDs. In electroluminescent QD-LEDs, QDs are excited through charge injection. In photoluminescent QD-LEDs, also known as color conversion QD-LEDs, the mechanism is based on the generation of photoluminescence from the optical excitation of QD material by LED chip.

Solid-state quantum dot-based light-emitting diodes (QD-LEDs)

The first QD based LED device was produced by Alivisatos and co-workers in 1994 [57]. As an electroluminescent QD-LED, they fabricated a hybrid organic/inorganic device which consist of cadmium selenide (CdSe) QDs and semiconducting p-paraphenylene vinylene (PPV) polymer. Eunjoo Jang and co-workers showed InP based QD-LED devices which exhibit excellent value for the EQE (21.4%) (Figure 2.16a) [13]. Recently, Hens and co-workers demonstrated green, amber, and red-emitting color conversion QD-LED devices using InP-based QDs. By implementing near-unity InP/ZnSe/ZnS core/shell QDs in photocurable thiol–ene resin, the QD-LEDs exhibited color conversion efficiency over 50% with nearly complete blue light rejection for green-emitting QDs (Figure 2.16b) [14].

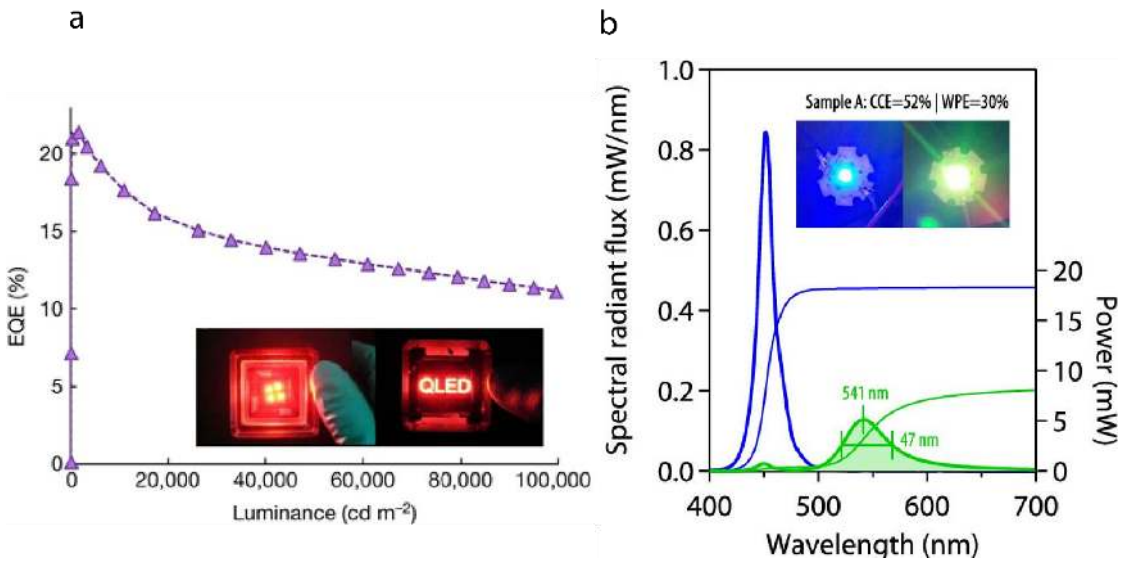

Figure 2. 16: (a) External quantum efficiency (EQE)–luminance profile of InP/ZnSe/ZnS QD based QD-LED device [13]. (b) Spectral radiant flux of (blue) the blue pump LED and (green) a green QD-on-chip LED both driven by a current of 10 mA together with the integrated power. CCE is color conversion efficiency, while WPE is wall plug efficiency [14].

Liquid-state quantum dot-based light-emitting diodes (QD-LEDs)

In the fabrication of solid-state QD-LED structures, QD materials are transformed from liquid to solid form. During transformation, the QDs' efficieny might drop due to several effects such as reabsorption losses [58, 59] and host-material effect [60, 61]. In order to overcome this issue, integration methods of QDs in liquid-state were presented as alternative routes. For instance, Sadeghi *et al.* showed liquid-state color conversion QD-LED which has white emission spectrum. In this study, they synthesized red-emitting CdSe/CdS/ZnS core/shell/shell and green-emitting CdSeZnS/CdSZnS alloyed core/alloyed shell QDs. Then, they fixed semi-sphere polydimethylsiloxane (PDMS) polymer on blue LED chip using UV curable polymer. After curing, they injected the QD solution inside LED device as shown in Figure 2.17 [62].

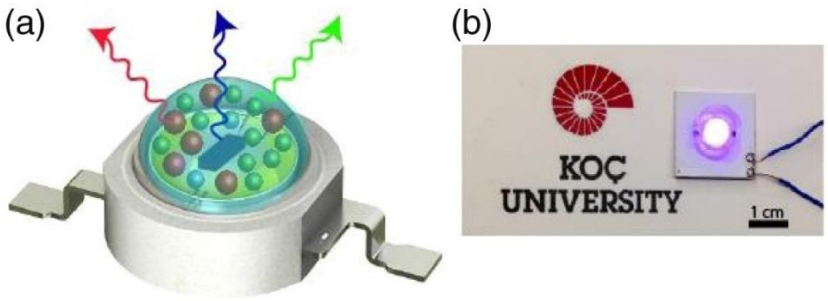

Figure 2. 17: (a) Schematic representation of liquid-state QD-LED device; (b) The image of fabricated liquid-state QD-LED device. When the QD-LED is turned on it emits white with a luminous efficiency of 200 lumen/watt [62].

Similarly, high-performance white light-emitting diodes over 150 lm/W was demonstrated by Onal *et al.* For that they synthesized green- and red-emitting ZnCdSe/ZnSe core/shell QDs with high PLQY of 94% [44]. Afterwards, they injected the QD solutions using microsyringe into LED device which was prepared via same methodology described above (Figure 2.18).

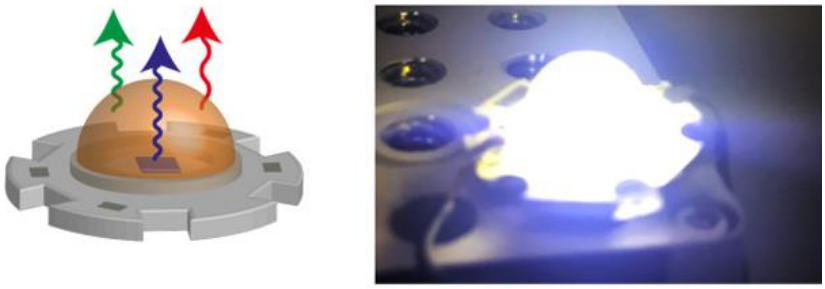

Figure 2. 18: (a) Schematic representation of liquid-state QD-LED device; (b) Image of fabricated white light-emitting QD-LED device when LED is turned on [44].

2.3 Optical analysis of quantum dot based light-emitting diodes (QD-LEDs)

The optical analysis of QD-LED devices is determined by variety of parameters such as luminous efficiency (LE), luminous efficacy of radiation (LER), correlated color temperature (CCT), color rendering index (CRI), color gamut coverage and ratio, (x, y) coordinates of light in the tristimulus color coordinates, external quantum efficiency (EQE) and power conversion efficiency (PCE).

2.3.1 Luminous efficiency (LE)

Luminous efficiency (LE) is defined as the effectiveness of a light source that converts electrical power to optical power sensed by human eye. The luminous efficiency refers to the ratio of the luminous flux emitted by the source to the electrical input power and it is measured using Equation (2.2) as follows:

$$LE = \frac{\Phi_{lum}}{IV} \tag{2.2}$$

where Φ_{lum} is the luminous flux which is a measure of light power of a source perceived by the human eye; whereas I and V are the forward injection current and voltage of the LED, respectively. Luminous flux can be calculated using Equation (2.3) given below [63].

$$\Phi_{lum} = 683 \frac{lm}{W} \int P(\lambda)\, V(\lambda)\, d(\lambda) \tag{2.3}$$

where $P(\lambda)$ is the power spectral density, $V(\lambda)$ is the eye sensitiviy function centered at λ= 550 nm (Figure 2.19) [63].

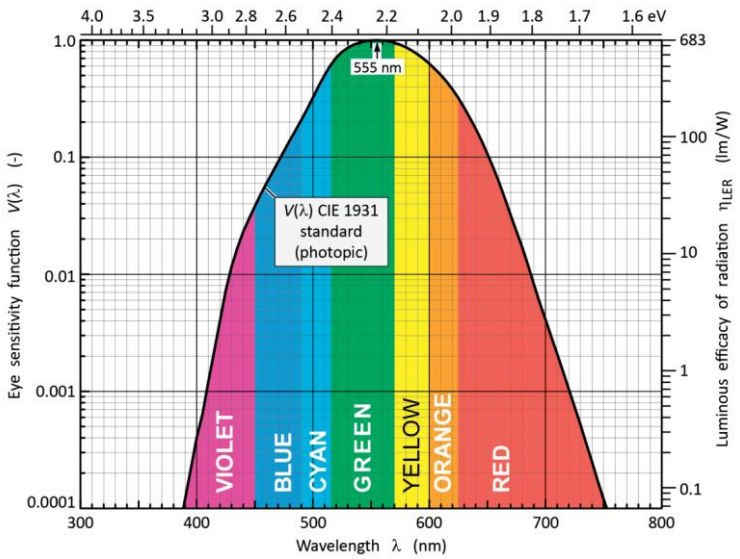

Figure 2. 19: Eye sensitivity function [63].

2.3.2 Luminous efficacy of radiation (LER)

The luminous efficacy of radiation is defined as the efficiency with which the emitted light can be converted to the perceived brightness by the human eye and it can calculated based on Equation (2.4) as follows [63].

$$LER = \frac{\Phi_{lum}}{P} \tag{2.4}$$

where P is the optical power from the light source.

2.3.3 External quantum efficiency (EQE)

The external quantum efficiency of the LED devices is defined as the ratio of number of photons emitted to number of electrons injected (Equation (2.5)) [63].

$$\eta_{ext} = \frac{P_{LED}/h\nu}{I/e} \tag{2.5}$$

2.3.4 Power conversion efficiency (PCE)

Another important parameter that defines the optical property of QD-LEDs is the power conversion efficiency (PCE) and it is calculated by using Equation (2.6).

$$PCE\,(\%) = \eta_{ext}\left(\frac{\lambda_1}{\lambda_2}\right) \tag{2.6}$$

where λ_1 and λ_2 are the wavelength of the photons absorbed and emitted by the LED, respectively.

2.3.5 Color gamut

The color gamut is the range of colors that can be produced by combining red, green, and blue. Color gamut is an important parameter in terms of image quality because it indicates the number of colors that a LED device can display. The most common way to depict the color gamut is as an area on a CIE xy chromaticity diagram that displays all the colors a typical human can see as shown in Figure 2.20.

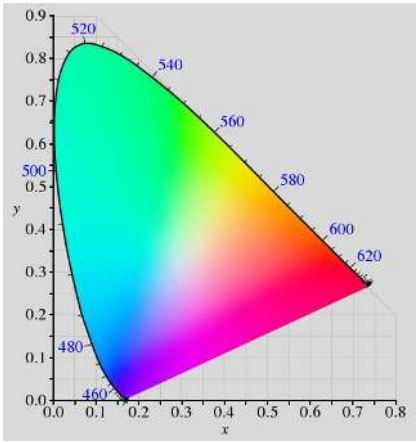

Figure 2. 20: The representation of color gamut.

2.3.6 The Photometric analysis of LEDs

LED measurements were performed with a multi-port Ocean Optics integrating sphere. The detector was an Ocean Optics Torus with an optical resolution of 1.6 nm FWHM over the spectra range. The signal to noise ratio was 250:1. In order to calculate the optical parameters, the intensity spectra was input inside the OSRAM Calculator software (Figure 2.21).

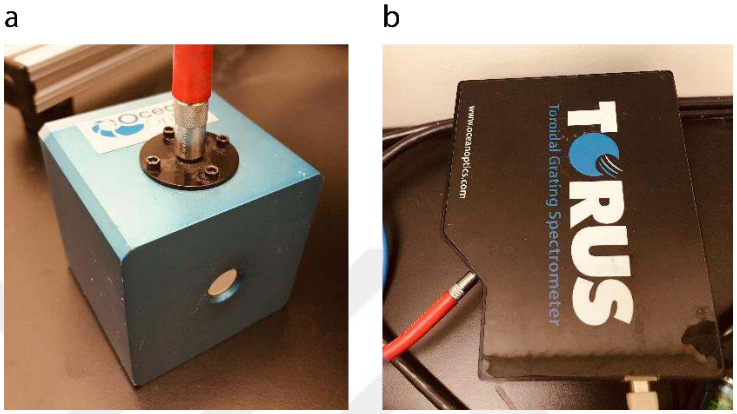

Figure 2. 21: (a) the integrating sphere; (b) optical detector.

2.4 Photocatalytic activity of semiconductor QDs

Since the first discovery over 90 years ago, photocatalysis has emerged as an effective technique in numerous fields such as antibacterial applications, the production of hydrogen fuel, and self-cleaning of building materials. In 1972, titanium dioxide (TiO_2) electrode is used for the first time for photocatalytic splitting of water by Fujishima and Honda [64]. In recent years, with the development of new materials more studies have been developed on semiconductor-based antibacterial applications. Among them, QDs have attracted great interest over the past decade owing to their great optical and chemical properties. Recently, different types of QDs such as indium phosphide (InP) [15], InP/ZnS core/shell structures [65], carbon nanodots (CDs) [66], silver bismuth sulfide ($AgBiS_2$) [24], are studied as efficient photocatalytic materials for various applications.

2.4.1 Photocatalysis mechanism in semiconductor QDs

Photocatalysis reaction is defined as the chemical reaction that takes place under the joint action of light and the photocatalyst. From the point of semiconductor photochemistry, photocatalysis mechanism is based on light-induced redox reaction caused by

photoinduced electrons (e^-) and holes (h^+) generated on the surface of the semiconducting materials such as QDs. As a result of excitation with light which is greater than the band-gap of the QDs, electron is excited from valence band to conduction band, leaving a hole in valence band. While electrons in the conduction band migrate towards the surface of QDs and they are involved in reduction reaction; whereas holes in the valence band move towards surface of QDs, causing oxidation reaction.

Water and oxygen are highly crucial parameters for photocatalysis reaction since photocatalysts are used in water vapor under aerobic conditions. After illumination with light, the redox reactions generate reactive oxygen species (ROS) which are defined as the chemical species formed upon incomplete reduction of oxygen [67]. There are mainly four types of reactive oxygen species generated in the photocatalytic redox reaction of oxygen and water, including (1) superoxide anion ($^{\bullet}O_2^-$), singlet oxygen ($^1O_2$), hydroxyl radical ($^{\bullet}OH$), and hydrogen peroxide (H_2O_2) as depicted in Figure 2.22 [68].

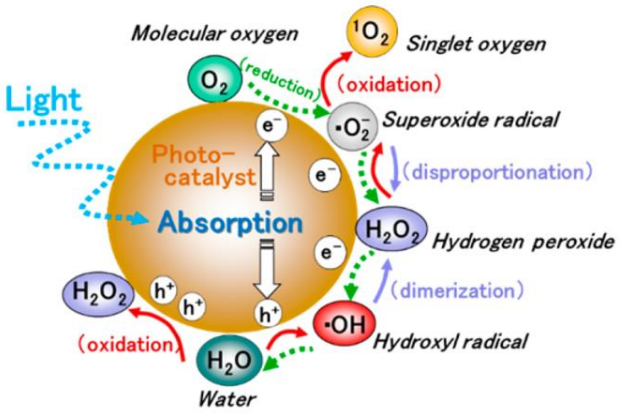

Figure 2. 22: Illustration of formation of reactive oxygen species in the photocatalytic redox reaction [68].

2.4.2 Superoxide radical ($^{\bullet}O_2^-$)

The amount of superoxide radical ($^{\bullet}O_2^-$) generated in aqueous medium is related to trapped electrons and holes on the surface of QDs. The reduction of O_2 with the conduction band electron (e^-) or the oxidation of H_2O_2 with a photo-induced valence band hole (h^+) causes the formation of superoxide radical ($^{\bullet}O_2^-$) as given in Equation (2.7) and Equation (2.8), respectively.

$$O_2 + e^- \rightarrow {}^{\bullet}O_2^- \tag{2.7}$$

$$H_2O_2 + h^+ \rightarrow {}^{\bullet}O_2^- + 2H^+ \quad (2.8)$$

Hydrogen peroxide formation depicted in Equation (2.8) is formed by the two-step oxidation of water or two electron reduction of O_2 as given in Figure 2.22.

2.4.3 Hydrogen peroxide (H_2O_2)

Comparing to other reactive oxygen species, hydrogen peroxide (H_2O_2) is the most stable molecule. In terms of generation of (H_2O_2), there are two mechanisms. Those mechanisms include the two-electron reduction of O_2, and the two-hole oxidation of water (Equation 2.9) as shown in Figure 2.22. After a one-electron reduction process, O_2 becomes superoxide radical ($^{\bullet}O_2^-$) as given in Equation (2.7). For the generation of hydrogen peroxide (H_2O_2), superoxide radical ($^{\bullet}O_2^-$) may undergo two reduction paths, involving the disproportionation of superoxide radical ($^{\bullet}O_2^-$) (Equation 2.10) or reduction of superoxide radical ($^{\bullet}O_2^-$) by photo-induced conduction band electron (Equation 2.11) [68].

$$2H_2O + 2h^+ \rightarrow H_2O_2 + 2H^+ \quad (2.9)$$

$$^{\bullet}O_2^- + {}^{\bullet}O_2H + H_2O \rightarrow H_2O_2 + O_2 + OH^- \quad (2.10)$$

$$^{\bullet}O_2^- + e^- + 2H^+ \rightarrow H_2O_2 \quad (2.11)$$

2.4.4 Hydroxyl radical ($^{\bullet}OH$)

Hydroxyl radical ($^{\bullet}$OH) is often regarded as the main effective reactant for oxidation processes in photocatalysis reactions. Photocatalytic oxidation of H_2O with the valence band holes (Equation 2.12) or reduction of hydrogen peroxide (H_2O_2) with conduction band electrons (Equation 2.13) generate the hydroxyl radical ($^{\bullet}$OH). Furthermore, hydroxyl radical ($^{\bullet}$OH) is formed by reaction of hydrogen peroxide (H_2O_2) with superoxide radical ($^{\bullet}O_2^-$) as given in Equation 2.14 [68].

$$OH^- + h^+ \rightarrow {}^{\bullet}OH \quad (2.12)$$

$$H_2O_2 + e^- \rightarrow {}^{\bullet}OH + OH^- \quad (2.13)$$

$$H_2O_2 + {}^{\bullet}O_2^- \rightarrow {}^{\bullet}OH + O_2 + OH^- \quad (2.14)$$

2.4.5 Singlet oxygen ($^1O_2$)

Singlet oxygen radical ($^1O_2$) is the lowest excited electronic state of molecular oxygen. It is usually generated by an energy transfer mechanism from the excited state of a given material. There are several groups of materials which have the ability to generate singlet oxygen radicals ($^1O_2$) reported in the literature. For instance, it has been shown that graphene quantum dot (GQDs) passivated with polyethylene glycol derivatives produce singlet oxygen radicals ($^1O_2$) by the excitation with blue light [69].

Chapter 3: Indium Phosphide (InP) Quantum Dots

3.1 Indium phosphide-based quantum dots (InP-QDs)

Among III-V semiconductor nanocrystals indium phopshide (InP) QDs have attracted great attention due to tunability of fluorescence emission throughout the visible and near-infrared range by changing the size [13, 15, 70]. InP has the zinc-blende crystal structure and a bulk-band gap of 1.35 eV which is corresponding to ≈920 nm in wavelength [71]. Furthermore, due to its environmentally benign and non-toxic property compared to cadmium (Cd) and lead (Pb)-based QDs counterparts InP QDs is considered as promising material in various applications [72-74].

3.1.1 History of InP QD synthesis

The studies of InP synthesis date back 1980s [75]. For the first time, Healy *et al.* synthesized InP crystals by using indium(III) chloride ($InCl_3$) and tris(trimethylsilyl) phosphine ($P(SiMe_3)_3$) as precursors. In the following years, controlling over the reaction kinetics was enhanced by the availability of novel synthetic techniques and reagents. In 1994, high-quality InP nanocrystals were reported by Nozik and co-workers [76]. In their study, InP nanocrystals were synthesized by mixing chloroindium oxalate complex with ($P(SiMe_3)_3$) at room temperature and heating the precursor solution in the presence of trioctylphosphine oxide (TOPO) and trioctylphosphine (TOP). However, these studies resulted in InP nanocrystal formation with weak quantum confinement and poor emission properties. Recently, advances in nanotechnology have led to development of highly efficient and monodisperse InP-based QDs [13, 77]. There are several procedures for InP QDs synthesis.

3.1.2 Synthesis methods of InP QDs

Hot-injection method

Similar to other semiconductor nanocrystals the formation of InP nanocrystals is explained by LaMer model. In the light of this model, Peng and co-workers synthesized InP QDs by rapid injection of $P(SiMe_3)_3$ precursor to an octadecene (ODE) solution which consists of indium acetate and fatty acids [78]. Moreover, they indicated that good size distribution and well-distinguished absorption features which are related to ligand type and concentration used during synthesis. In 2019, the same group introduced

stoichiometry controlled InP-based QDs which possess near-unity photoluminescence quantum yield (PLQY), mono exponential decay dynamics, narrow line width using similar reagents for QD-LED application [79].

Until 2013, the synthesis of InP QDs is mostly based on injection of $P(SiMe_3)_3$ precursor at elevated temperature. However, the rapid depletion of this phosphorus source prompted researchers to explore alternative phosphorus precursors to be used in the synthesis of InP QDs.

Alternative phosphorus source for InP QDs synthesis

For InP QDs synthesis, tris(trimethylsilyl) phosphine ($P(SiMe_3)_3$) precursor has been dominant phosphorus source for more than 30 years. However, tris(trimethylsilyl) phosphine ($P(SiMe_3)_3$) precursor has problematic attributes such as being expensive and explosive in contact with air. Nowadays, amino phosphines are emerging precursors compared to silyl phosphines as economic and safe-to-use under ambient conditions for the synthesis of efficient InP nanocrystals [80, 81]. Basically, in this technique indium halides and zinc halides are dissolved in a primary amine solvent such as oleylamine (OAm) [80]. Song et al. first demonstrated InP QDs by employing amino phosphine [82]. More recently, Hens and co-workers synthesized InP-based core/shell QDs with more than 90% of PLQY covering all visible spectrum using amino phosphine as phosphorus source [77].

Heat-up method

The first heat-up method-based InP QDs with a mean diameter of around 26 nm in size was introduced by Mićić *et al* in 1994 [83]. In their procedure, they used chloroindium oxalate and $P(SiMe_3)_3$ as the raw materials. They treated the raw materials with a mixture of trioctylphosphine oxide (TOPO) and trioctylphosphine (TOP) at 270º C for several days. Later, Reiss and co-workers demonstrated one-pot synthesis of InP/ZnS core/shell QDs by heating all precursors, including indium myristate, zinc stearate, dodecanethiol, and ($P(SiMe_3)_3$) together in ODE [84].

Seeded growth

The seeded growth technique is defined as the introduction of seed nanocrystals into the reaction medium to initiate the nucleation of the target nanocrystals. A schematic illustration of this technique is given in Figure 3.1 [28].

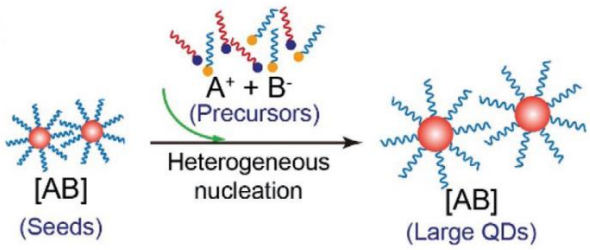

Figure 3. 1: The schematic illustration of the seeded growth method [28].

One of the most prominent advantage of this method is exceptional controlling the size and morphology of nanocrystals. As an example, InP/ZnSe/ZnS core/shell/shell QDs which possess near-unity PLQY of 100% with full width at half maximum (FWHM) of 35 nm were synthesized via seed-assisted hot injection method (Figure 3.2) [13].

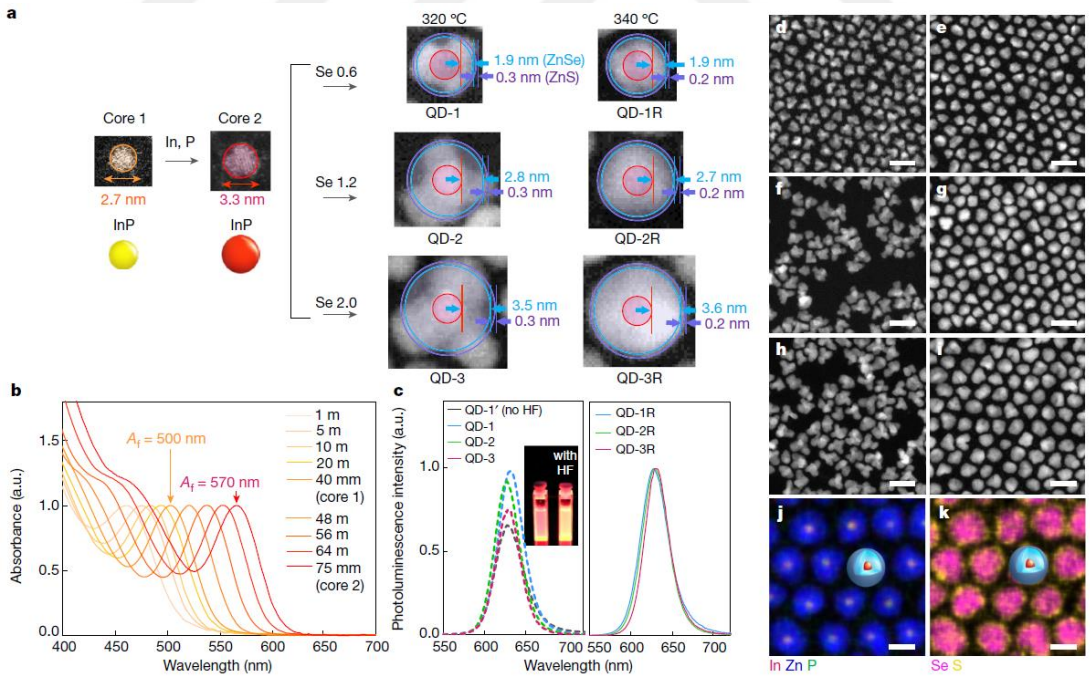

Figure 3. 2: Uniform, highly symmetrical and near-unity emitting InP/ZnSe/ZnS QDs synthesized by seed-assisted hot injection method [13]. (a) Preparation of InP cores and InP/ZnSe/ZnS QDs with different morphology and shell thickness. The amounts of Se

precursor for QD-1, QD-2 and QD-3 were 0.6 mmol, 1.2 mmol and 2.0 mmol, respectively, per 10 ml of solvent. The estimated size, based on inductively coupled plasma-atomic emission spectroscopy (ICP-AES) data, was projected on the STEM image of each QD. (b) Ultraviolet–visible absorption spectra of the aliquots, taken during the InP core synthesis. a.u., arbitrary units. (c) Photoluminescence spectra of QD-1′ (prepared without HF addition), QD-1, QD-2, QD-3, QD-1R, QD-2R and QD-3R. Inset, photograph of QD-1′ (no HF) and QD-3 taken under 365 nm illumination. (d-i) STEM images of QD-1, QD-1R, QD-2, QD-2R, QD-3 and QD-3R (scale bar, 20 nm). (j, k) Electron diffraction spectroscopy mapping of In, Zn, P, Se, and S for QD-3R (scale bar, 10 nm).

Cation exchange

Cation exchange process for the synthesis of InP QDs was performed by Beberwyck and Alivisatos in 2012 by incubating Cd_2P_3 QDs and $InCl_3$ in TOP medium at 270° C [85]. Later, InP QDs were prepared by cation exchange using $Cu_{3-x}P$ template instead of a Cd_2P_3 template. Manna and co-workers used $Cu_{3-x}P$ nanocrystals as material template to synthesize hexagonal wurtzite InP QDs in the presence of TOP and ODE. They also showed that cationic diffusion started from the peripheral corners of $Cu_{3-x}P$ nanocrystals and gradually evolves toward the center [86]. Similarly, Ji and co-workers demonstrated wurtzite monodisperse InP QDs with controllable size through cation exchange of Cu_3P nanocrystals. Moreover, they grew a gradient ZnSeS shell on wurtzite InP core structure, producing fluorescent QDs that emit peak wavelength between 674 and 754 nm (Figure 3.3) [87].

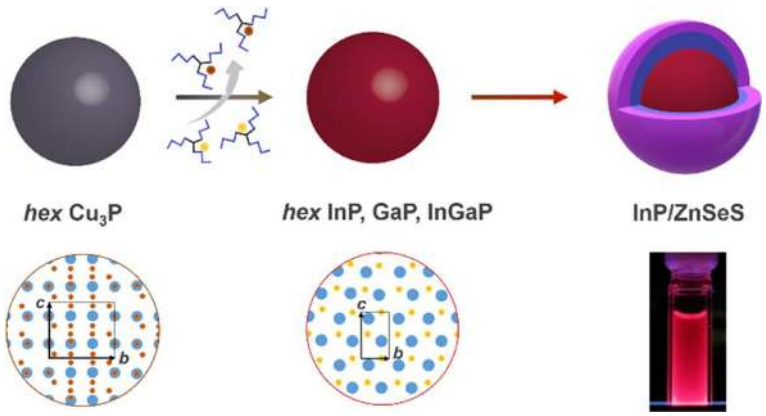

Figure 3. 3: Schematic illustration of wurtzite InP QDs which were synthesized through cation exchange process. After growth of gradient ZnSeS shell, the resulting core/shell QDs emitted peak wavelength between 674 and 754 nm [87].

Microwave-assisted synthesis

In this rapid technique, high-power microwaves are applied to polar solvents to force rotate and collide, resulting in heating of reaction medium [28]. Mostly, the QDs synthesis can be completed in less than 5 min. Hence, this technique holds great potential for the large-scale synthesis of InP QDs. Additionally, it can provide uniform heating for the synthesis process compared to conventional techniques. One of the first study based on microwave-assisted InP synthesis was performed by Strouse and co-workers in 2005 and the PLQY of the generated InP QDs was %4 [88].

Conversely, microwave-assisted technique also has some drawbacks. First, it lacks synthesizing InP-based core/shell structures such as InP/ZnS QDs. Second, it is hard to analyse the intermediate products formed during synthesis.

Continuous injection synthesis

High anion precursor reactivity (phosphorus source) during InP QDs synthesis leads to the rapid depletion of the precursor. Thus, it prevents the formation of monodispersed InP QDs. To address the aforementioned issue, Bawendi and co-workers introduced a novel continuous injection strategy that does not require any initial hot-injection or heat-up step for large InP QDs with low polydispersity. Therefore, the nucleation and growth of InP QDs are initiated by single continuous injection step. The resultant InP QDs exhibited absorption peak at 631 nm with a half width at half-maximum of 81 meV [89].

3.1.3 Surface chemistry of InP QDs

Types of surface ligands

For the InP QDs synthesis and their various applications, different types of surface ligands are used. The types of surface ligands are divided into three main categories based-on the theory of coordination chemistry: (1) L-type ligands; (2) Z-type ligands; (3) X-type ligands. L-type ligands such as primary amines (e.g., Oleylamine-OLA, hexadecylamine-HDA), phosphines (PR_3), and phosphine oxides (OPR_3) bind as neutral two-electron donors (Lewis bases) to unoccupied surface metal atoms (Lewis acids) [90]. These type

of ligands are neutral donors. Z-type ligands are neutral acceptors which consist of metal cation and inorganic anion such as $InCl_3$ [91]. Finally, X-type ligands such as carboxylates ($RCOO^-$), thiolates (RS^-), sulfide (S^-) provide one electron to bond with metal ions present on the surface of QDs [90].

According to hydrophobicity and hydrophilicity properties, they can also be classified into two main categories. Hydrophobic ligands typically consist of long alkyl chains such as oleic acid (OA), stearic acid (SA), myristic acid (MA), and trioctylphosphine (TOP). These ligands make QDs soluble only in nonpolar solvents such as octadecene (ODE). Hydrophilic ligands have bifunctional groups, in which surface-anchoring and hydrophilic end groups are both present. Therefore, the QDs which are capped with these ligands can be dissolved in water. Typical examples for this type of ligand are 3-mercaptopropionic acid (MPA), cysteine [90].

Ligand exchange

The ligands which are used to synthesize colloidal QDs are mostly soluble in non-polar solvents such as ODE and OLA [13, 81]. However, according to specific applications after synthesis of InP QDs, it is required to ligand exchange to make water soluble QDs. For instance, Yu *et al.* introduced sulfide-capped InP core and InP/ZnS core/shell QDs as an alternative and non-toxic material photosensitizer for the photocatalytic hydrogen evolution in 2018. First, InP core and InP/ZnS core/shell QDs were synthesized using oleylamine (OLA) as long alkyl chain. Then, the QDs were ligand exchanged with sulfide (S^-) in the presence of formamide (FA) or N-methylformamide (NMF), resulting in highly photocatalytic material [65]. In another study, Lee and co-workers showed highly efficient MPA capped InP QDs against various bacterial species, including *Staphylococcus aureus, Bacillus cereus, Escherichia coli and Pseudomonas aeruginosa* for photodynamic treatment [92].

Water-induced surface oxidation

InP QDs exhibit oxophilic property, which makes them highly sensitive to oxidation during synthesis [93, 94]. In previous studies, it has been shown that water presence significantly induces the oxidation of the QDs. As a pioneering study, Cros-Gagneux et al. investigated the surface chemistry of the InP QDs, and they showed that dialkyl ketone was formed during the synthesis process via a decarboxylative coupling route and

provides oxidative conditions [95]. The resulting QD was a structure composed of InP/InPOx/palmitate ligand. Later, Virieux and et al. studied InP/ZnS core/shell QD and its surface and interface. They obtained that in a typical synthesis of InP QDs, ketonic decarboxylation of the carboxylic acids produces water as a byproduct which oxidizes the surface of nanocrystal during process. As a result, an amorphous mixed oxide phase which was made of $InPO_x$, In_2O_3, and $InO_y(OH)_{3-2y}$ formed as illustrated in Figure 3.4 [93].

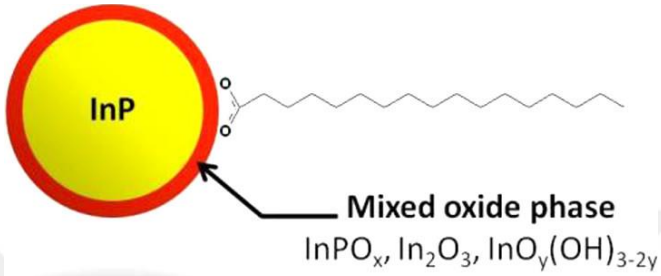

Figure 3. 4: Schematic illustration of oxide layer which is formed on the surface of InP QDs. Ketonic decarboxylation of the carboxylic acids causes water formation during synthesis process at elevated temperature. As a result, an amorphous mixed oxide phase, including $InPO_x$, In_2O_3, and $InO_y(OH)_{3-2y}$ forms [93].

Hydrofluoric acid (HF) treatment

Hydrofluoric acid (HF) treatment has been known as an effective technique for increasing the PLQY of InP QDs over 20 years [96]. There are several explanations on the etching mechanism of HF treatment. It is thought that HF treatment passivates the traps at undercoordinated surface phosphorus atoms and removes the oxidized phosphorus layer from the surface of QDs [97]. Won *et al.* demonstrated a significant increase in PLQY value due to removing of the phosphorus based oxide layer after HF treatment for the synthesis of InP/ZnSe/ZnS QDs (Figure 3.5) [13]. Interestingly, when they perform HF treatment step before ZnSe shell growth it resulted in poor passivation. Instead, they added HF solution at an early stage of shell growth. As an alternative HF mechanism, which is studied by Alivisatos and co-workers, fluorine ions directly bind to surface indium dangling bond of the In-based QDs (InAs) and removing the bulkier carboxylate ligands [98].

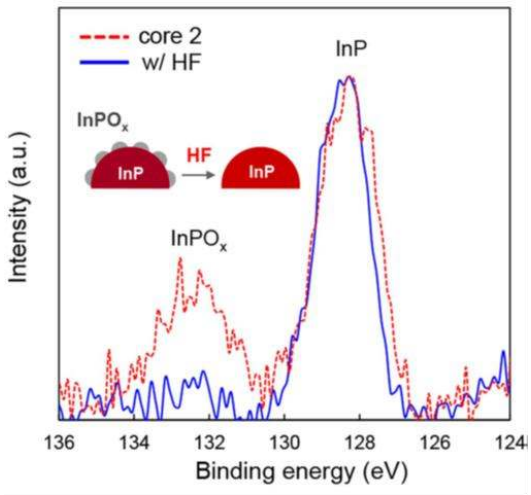

Figure 3. 5: X-ray photoelectron spectroscopy (XPS) result of the InP QDs before and after HF treatment. After removing of the phosphorus oxide layer by HF treatment, XPS peak which is related to $InPO_x$ disappears [13].

3.1.4 Defects of InP QDs

Colloidal QDs possess inherent, multiple dangling bonds (DB) on their surface as a result of intrinsic weak bonding nature and steric hindrance of organic ligands [99]. These dangling bonds cause the formation of surface trap states that can have detrimental effects on photoluminescence properties. In previous studies, it has been shown that InP QDs have two type dangling bonds (D), including indium (In-DBs) and phosphorus (P-DB)[99]. For InP core QD, both In-DB and P-DB create invariant DB energy levels at -3.947 eV and -5.717 eV regardless of the core size. Moreover, In-DB and P-DB generate deep and shallow trap levels in the photoluminescence spectra, respectively.

Based on the density functional theory (DFT) calculations [99], HOMO level of InP increases; whereas LUMO level decreases as the QD size increases due to the quantum confinement effect as given in Figure 3.6.

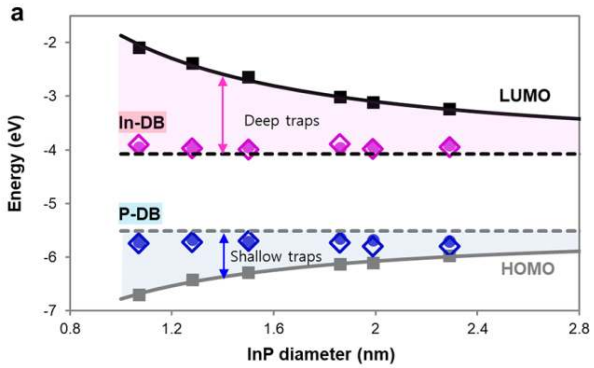

Figure 3. 6: Energy levels of HOMO, LUMO, In-DBs, and P-DBs of InP QDs based on the DFT calculations. When the QD size increases HOMO level increases; whereas LUMO level decreases. Regardless of the QD size, indium and phosphorus dangling bonds are at levels of -3.947 eV and -5.717 eV, respectively [99, 100].

3.1.5 Core/shell InP QDs

In order to passivate the surface trap states, it is required to form a core/shell structure by embedding the InP core QDs into another semiconductor material. InP-based core/shell structures are divided into three categories based on the energy band alignment of core and shell material: (1) type-1, (2) type-2, and (3) reverse type-I. For the type-I core/shell structure, electron-hole pair is confined in the InP region. Furthermore, the epitaxial shell growth on core is highly important, thus the lattice mismatch between core and shell material should be minimized. Typical and widely used InP-based type-I core/shell structures are InP/ZnSe, InP/ZnS, and InP/ZnSe/ZnS QDs. The growth of ZnS shell on InP by seeded growth technique was introduced by Weller and co-workers in 2001 [101]. Later, Peng and co-workers synthesized InP/ZnS core/shell QDs with a PLQY of 40%. In that work, they grew ZnS shell by adding the zinc and sulfur precursor solutions at low temperature and heating to high temperatures for several cycles [102].

The lattice mismatch between InP and ZnS (7.6%) results in formation of lattice strains, which causes broadening of the emission peak. Thus, adding an interlayer which has lower lattice mismatch (e.g., for ZnSe 3.4%) between InP and ZnS is an effective approach to increase the PLQY of the core/shell QDs. Similarly, alloyed shells such as $ZnSe_{1-x}S_{x}$[103] and $Zn_xCd_{1-x}Se$ [104] are also used to minimize the strain effects for highly efficient QDs. Recently, Hens and co-workers reported InP/Zn(Se,S)/ZnS QDs covering the visible spectrum with near unity PLQY [77].

For the InP-based type-II QDs, one charge carrier is confined in the core, whereas the other charge carrier is confined in the shell structure. Consequently, electron and hole wavefunctions are spatially separated, causing ref-shift in PL emission. Lian *et al.* synthesized quasi-type-II InP/CdS core/shell QDs for the first time in 2013 [105]. In 2018, Sadeghi et al. introduced heavy metal-free quasi-type-II InP/ZnO core/shell QDs. Although the lattice mismatch between InP and ZnO is relatively high (around 11%) they demonstrated that due to reduced reabsorption loss InP/ZnO core/shell QD is promising material for luminescent solar concentrator (LSC) application [48]. In the same year Bahmani et al. used the same material for neural photostimulation application [106]. Reverse type-I core/shell/shell structure consisting of ZnSe/InP/ZnS QDs were developed by Kim and co-workers [107]. They showed that by adjusting the InP layer thickness the emission color was tuned from violet to red.

3.1.6 Transition metal doped InP QDs

To date, various transition metals such as copper (Cu), manganese (Mn), and silver (Ag) were incorporated into InP QDs [19, 20, 108-110]. Among them, Cu doped InP/ZnSe (Cu:InP/ZnSe) QDs with tunable emission ranging in the red and near-infrared regions (NIR) (630−1100 nm) has been first introduced by Peng and co-workers in 2009 [19]. They synthesized Cu:InP QDs by investigating several key parameters, including reaction temperature, copper concentration, etc. They observed that the optimum temperature for effective surface adsorption of copper dopant ions on InP QD surface was around 130° C, indicated by PL quenching of InP core. Subsequently, the temperature was increased to 210° C at a rate of 2° C/min, resulting in a dramatic increase of the dopant PL intensity which shows the incorporation of copper ions into InP crystal structure.

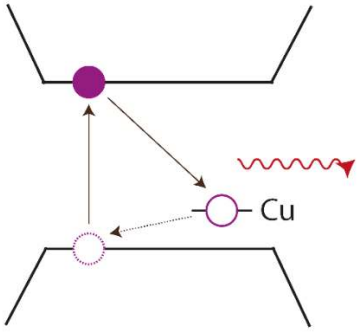

Figure 3. 7: Energy diagram of Cu:InP QDs.

When properly doped in InP crystal structure, Cu^+ dopant ion generates intragap energy level which is located above valence band of InP (Figure 3.7). Upon excitation of host nanocrystal copper acts as hole acceptor and the photo-generated electrons recombine with holes localized at Cu^+ trap state, resulting in red-shift in PL emission [19]. Thus, copper dopant emission can be tuned by adjusting the host nanocrystal size. On the other hand, for the manganese doped QDs, the emission is not affected by the size of host nanocrystals due to the forbidden intrashell (d-d) transition of the Mn^{2+} ion as demonstrated in Figure 3.8 [108]. The radiative transition results from the recombination of electrons located at $^4T_1$ with holes localized at the $^6A_1$ (Figure 3.8).

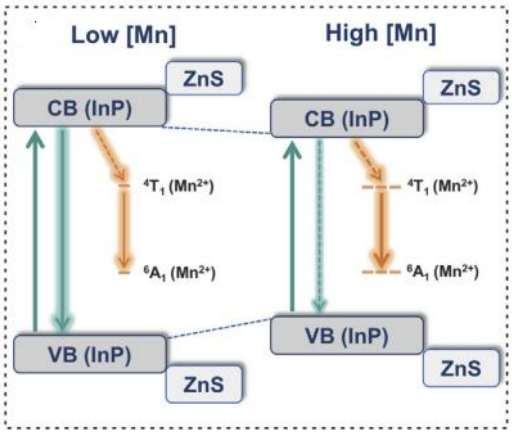

Figure 3. 8: The schematic recombination mechanism of Mn:InP/ZnS QDs [108].

Mei et al. synthesized Mn and Cu doped InP/ZnS QDs, via nucleation growth technique at different Cu:Mn ratios [108]. The resulting Mn:InP/ZnS QDs exhibited PLQY of 71.6% with 5 milisecond (ms) fluorescent lifetime.

3.1.7 Biocompatibility of InP QDs

InP-based QDs have emerged as promising materials to be used in biomedical applications due to their less toxicity alternative to cadmium-based counterparts. Different surface modifications and dose are also crucial considering the toxicity of InP QDs. Chen *et al.* reported the concentration dependent cytotoxicity of the InP/ZnS QDs modified with different surface groups, including amine (NH_2), carboxyl (COOH), and hydroxyl (OH). According to MTT (3-(4, 5-dimethylthiazolyl-2)-2, 5-diphenyltetrazolium bromide) assay results, they obtained that the cell viability remained above 90% for InP-NH_2 and InP/ZnS-OH groups and above 80% for InP/ZnS-COOH

groups, respectively [111]. Prasad and co-workers showed bioconjucated InP/ZnS core/shell QDs with high quality and bright luminescence for imaging pancreatic cells [112]. First, they synthesized InP/ZnS QDs using hot-injection and SILAR techniques. Then, the surface of the QDs were functionalized with mercaptosuccinic acid, followed by pancreatic cancer specific monoclonal antibodies. The viability of treated cells with QDs remained the range of 80-90% relative to that of untreated cells for 24 and 48 h.

Recently, Bahmani Jalali et al. showed InP-based QDs' (InP/ZnO and InP/ZnS QDs) viability and biocompatibility for neural photostimulation application [106, 113]. MTT assay results showed that the photoelectrode which consists of InP/ZnO core/shell QDs did not exhibit any toxic effect Neuro2A cells under either in the dark or blue light exposure. Similarly, to investigate the biocompatibility of InP/ZnS QD-based biointerfaces mitochondrial activity and membrane integrity are measured using MTT and lactate dehydrogenase (LDH) assay using SH-SY5Y cells a neuroblastoma cell line. It has been shown that the resulting QD-based biointerfaces did not affect the cell viability and membrane permeability of cells.

Chapter 4: Cadmium-free and Efficient Type-II InP/ZnO/ZnS Quantum Dots and Their Application for LEDs

This section is based on the publication ''*Cadmium-free and Efficient Type-II InP/ZnO/ZnS Quantum Dots and Their Application for LEDs*'' G.O. Eren, S. Sadeghi, H. Bahmani Jalali, M. Ritter, M. Han, I. Baylam, R. Melikov, A. Onal, F. Oz, M. Sahin, C. W. Ow-Yang, A. Sennaroglu, R. T. Lechner, and S. Nizamoglu, ACS *Applied Materials & Interfaces* 13.27 (2021): 32022-32030. Reproduced (or "Reproduced in part") with permission from American Chemical Society Copyright 2021.

It is a generally accepted perspective that type-II nanocrystal quantum dots (QDs) have low quantum yield due to the separation of the electron and hole wavefunctions. Recently high quantum yield levels were reported for cadmium-based type-II QDs. Hence, the quest for finding non-toxic and efficient type-II QDs is continuing. Herein, we demonstrate environmentally benign type-II InP/ZnO/ZnS core/shell/shell QDs that reach to a high quantum yield of ~91%. For that ZnO layer was grown on core InP QDs by thermal decomposition, which was followed by ZnS layer via successive ionic layer adsorption. The small angle x-ray scattering (SAXS) shows that spherical InP core and InP/ZnO core/shell QDs turn into elliptical particles with the growth of the ZnS shell growth. To conserve the quantum efficiency of QDs in device architectures, InP/ZnO/ZnS QDs were integrated in-liquid state on blue LEDs as down-converters that led to an external quantum efficiency (EQE) of 9.4% and power conversion efficiency (PCE) of 6.8%, respectively, which is the most efficient QD-LED using type-II QDs. This study pointed out that cadmium-free type-II QDs can reach high efficiency levels, which can stimulate novel forms of devices and nanomaterials for bioimaging, display, and lighting.

4.1 Introduction

Semiconductor nanocrystal quantum dots (QDs) have attracted significant attention for light-generating devices such as luminescent solar concentrators [48, 114, 115], light-emitting diodes [13, 116-118] and lasers [119, 120]. They show advantageous properties such as tunable emission color due to quantum confinement effect, high photochemical stability, and solution processability [121-124]. Especially, high photoluminescence quantum yield (PLQY), defined as the ratio of the number of photons emitted to the total number of generated excitons, is a key figure of merit. To reach high PLQYs, type-I

quantum dots with straddling alignment that localize the electron and hole inside the core are the most widely investigated heterostructures.

Alternatively, type-II QDs have conduction and valence band extrema in different materials, and it is a generally accepted perspective that type-II QDs result in low PLQYs. So far, a wide variety of type-II heterojunctions composed of CdSe, CdS, CdTe, and ZnTe (e.g., CdTe/CdSe, ZnTe/CdSe) have been examined [125-128]. However, their PLQY remained low, which is attributed to the spatial separation of the electrons and holes that leads to the increase of the nonradiative recombination rates and decrease of PLQY. Recently, high PLQY values of 61% [17], 68% [18], and 88% [129] were achieved with ZnSe/CdS/ZnS, CdSe/CdTe, $Cd_xZn_{1-x}S$/ZnSe/ZnS type-II QDs, respectively. But, the aforementioned type-II QDs have highly toxic heavy metal of cadmium [130-132]. Alternatively, there were also a few cadmium-free QDs (e.g., ZnTe/ZnSe) investigated, but their PLQY reached up to 36% [106, 133]. Therefore, the quest for finding efficient and Cd-free type-II QDs, which can find widespread use to form environmentally benign light-generating devices and biocompatible luminescent markers, is continuing.

In this section, we demonstrate InP/ZnO/ZnS core/shell/shell QDs, which have type-II staggered line-up heterojunctions. We synthesized ZnO shell with thermal decomposition and grew subsequent multiple ZnS shells with SILAR method. We optimized the ZnO and ZnS shell thickness that led to a high efficiency PLQY of 90.8%. Moreover, QDs were integrated in liquid-state on blue LEDs and QD-LEDs demonstrated EQE and PCE of 9.4% and 6.6%, respectively.

4.2 Results and Discussion

4.2.1 Synthesis of InP/ZnO/ZnS core/shell/shell QDs

InP core QDs were synthesized via hot-injection method [48, 134, 135]. For that, zinc undecylenate was used to passivate InP cationic dangling bonds and decrease trap states [134], [136], and oleylamine (OAM) and oleic acid (OA) were used as stabilizing agents. In brief, indium chloride ($InCl_3$), OAM, OA, and zinc undecylenate were dissolved in the 1-octadecene (ODE) solvent in glovebox at room temperature. After degassing and heating to 200° C, tris-(trimethylsilyl)phosphine ($P(TMS)_3$) was injected into reaction mixture to initiate the nucleation and growth. To generate a type II band alignment ZnO shell was selected; by considering the successful growth of CdTe/ZnSe core/shell QDs

with a lattice mismatch of 14% [137] ZnO growth on InP with a lattice mismatch of 11% is also feasible [48, 106, 138]. In this regard, ZnO was grown on InP core by thermal decomposition of zinc acetylacetonate ($Zn(acac)_2$) [139, 140]. During the synthesis, OAM was used as the stabilizing agent in order to hinder ZnO aggregation [141]. Furthermore, a different amount of ZnO precursor solution was added for reaching the highest PLQY (see Appendix A). To further increase the PLQY we performed ZnS growth on InP/ZnO core/shell structure by using SILAR technique. For that, the reaction solution of InP/ZnO was cooled down to 170° C and zinc stearate-ODE ($Zn(St)_2$-ODE) and sulphur- trioctylphosphine (S-TOP) stock solutions were added to reaction solution and temperature was increased to 250° C for 30 min. Similarly, to grow additional ZnS shells the temperature followed the same thermal cycling.

4.2.2 Quantum mechanical calculations and optical analysis

To understand the optical properties of the synthesized QDs we calculated their quantum mechanical properties by self-consistently solving Poisson-Schrödinger equations in the effective mass approximation (Figure 4.1b, Figure 4.1c, and Figure 4.1d) and correlated them with the optical measurements (Figure 4.2) [106]. InP core QD has type-I band alignment that led to the confinement of electron and hole in the same spatial core region with a high overlap of the wavefunctions of ~90% (Figure 4.1b). After ZnO shell growth, the band alignment of the nanostructure transit from type-I to type-II, and while hole wavefunction is confined completely in the core region like in InP core QD, electron wavefunction expands towards to ZnO shell that reduces the wavefunction overlap to 60% (Figure 4.1c) [142]. Since the delocalization of the electron decreases the confinement energy level within the conduction band and the exciton binding energy, the photoluminescence peak red-shifted from 585 nm to 613 nm while the FWHM maintained at ~74-75 nm for core and core/shell nanostructures. We investigated the PLQY of ZnO shell growth under different ZnO molar ratio, PLQY reached 25.8% (see Figure 4.2a & Appendix A).

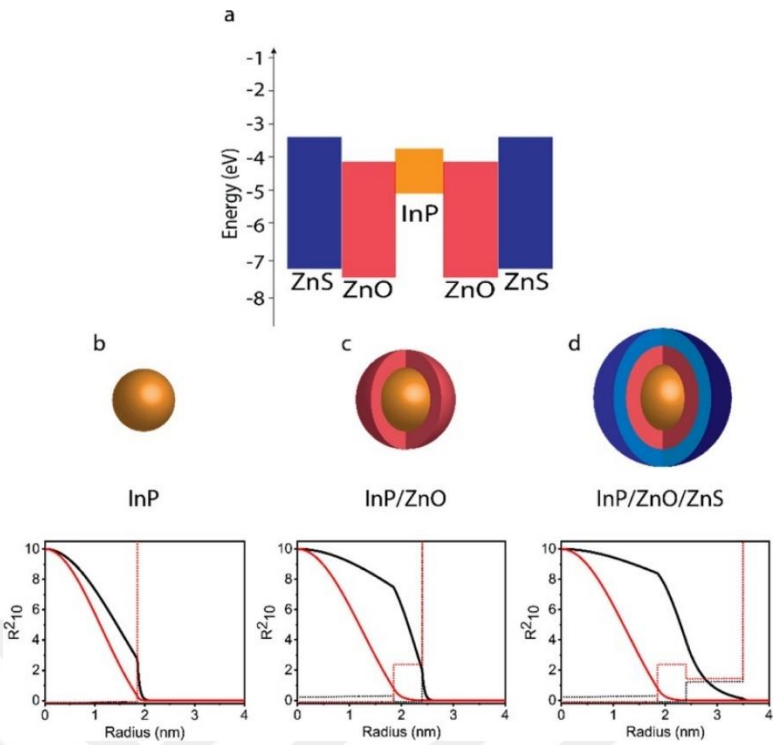

Figure 4. 1: (a) Energy band diagram of InP/ZnO/ZnS core/shell/shell QDs. Quantum mechanical simulations of (b) InP core, (c) InP/ZnO core/shell, and (d) InP/ZnO/ZnS core/shell/shell QDs. Black lines correspond to the radial probability distribution of electrons, while red lines show the radial probability distribution of holes. Black and red dashed lines correspond to confinement potential profile for electrons and holes, respectively.

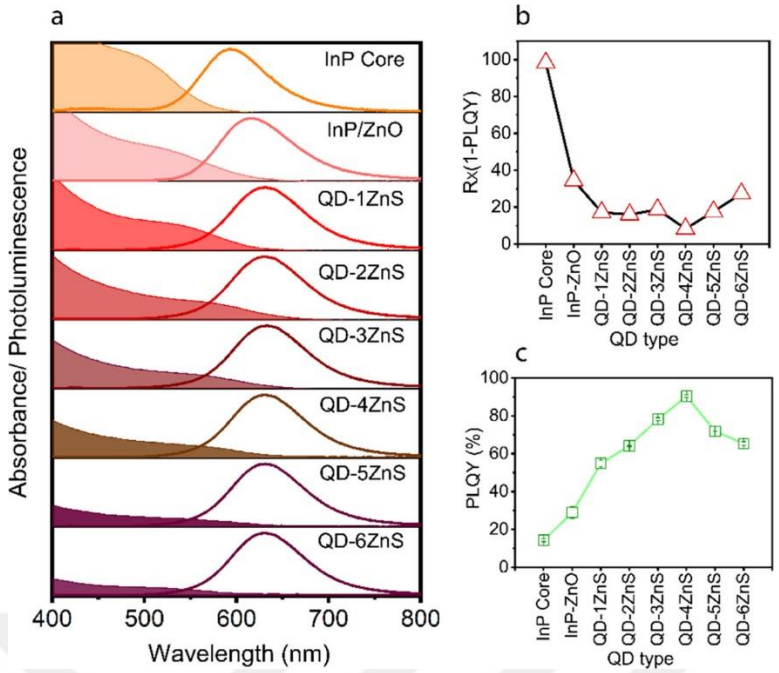

Figure 4. 2: (a) Absorbance and PL spectra of InP, InP/ZnO, and InP/ZnO/ZnS QDs with multiple shells. Here, QD refers to the InP/ZnO core/shell QDs and #ZnS refers to the number of SILAR growth cycles. (b) Normalized quenching factor of the QD-4ZnS core/shell NCs calculated by multiplication of reabsorption R and (1-PLQY). (c) PLQY (%) of QDs in hexane. Errors bars represent the standard deviation from three measurements.

Afterwards to reach higher PLQYs, a variety of ZnS shell thickness was investigated. From 1 to 4 cycles of ZnS shell growth, the PLQY increased due to effective confinement of electron-hole pairs in the InP-ZnO nanostructure and surface passivation (Figure 4.2c) [143]. After the fourth growth cycle of ZnS, PLQY of InP/ZnO/4ZnS nanocrystals (QD-4ZnS NCs) started to decrease, possibly due to higher interfacial strain caused by dislocations [137, 144]. By the fourth ZnS shell, PLQY reached the maximum level of 90.8%. QD-4ZnS showed a PL peak at 618 nm, which is slightly red-shifted (5 nm) with respect to InP/ZnO QDs due to the lower wavefunction overlap of 49%. We also investigated the effect of ZnO and ZnS shell growth on the normalized quenching factor (reabsorption x (1-PLQY)) [34] for core and core/shell structures to select the appropriate nanostructure (Figure 4.2b). After ZnO shelling due to red shifting of the PL peak quenching factor decreased, and the minimum value is observed at QD-4ZnS NCs.

4.2.3 Structural analysis

To understand the size and shape of the quantum dots we performed SAXS measurement in ethanol [145] by probing up to 10^6 individual particles. The scattering data after subtracting the ethanol background are shown in Appendix A, which are plotted versus the reciprocal scattering vector *q*. In Figure 4.3a we plotted instead of the reciprocal form factor *P(q)* directly its Fourier transform, the pair distance distribution function (PDDF) in real space [145, 146]. The PDDF is the distribution of all distances within all single particles of the probed sample volume, which also contains the mean particle dimensions of the whole ensemble. From the maximum dimension found within the PDDF, we derive the maximum dimension found within the particle ensemble. The bell-like PDDFs of the InP-core and the InP/ZnO core/shell QDs indicate spherical quantum dot shapes, whereas the asymmetric shape of the QD-4ZnS-PDDF is a hint for an elongated mean shape. The change from a spherical shape for the InP and InP/ZnO QDs to a more elliptical one for the QD-4ZnS NCs can be also seen in the fact that only the first two SAXS curves could be fitted with monomodal distributions of spheres as shown in Figure 4.3b. In these distributions, we derive from the peak positions directly the mean radii and hence the mean diameters of the QDs, from the widths of the size distributions. For the InP-core we get a sphere diameter of 3.6±0.8 nm and for the InP/ZnO core/shell QDs 4.4 ± 0.9 nm with size distributions between 9-10%, which is in excellent accordance with the TEM data shown in the inset of Figure 4.3c and Figure 4.3d. The asymmetric PDDF of QD-4ZnS NCs, however, indicates a *prolate* like mean particle shape [147]. The short diameter is only a bit larger than the spherical diameter of 4.4 nm found for the InP/ZnO NCs as can be deduced from the slightly shifted peak of the QD-4ZnS-PDDF with respect to InP/ZnO-PDDF (see Figure 4.3a). The long axis is derived from the long tail within the PDDF, from which we deduce maximum values between 9 to 10 nm. Most of the QDs within the ensemble depicts long axis values between 6-7 nm, which is within the broader mean size distribution found by TEM with a maximum at 7.02±0.9 nm (Figure 4.3e). The elongated shape of the QD-4ZnS NCs together with their chain-like fractal aggregation (see Appendix A) can be explained by a slightly inhomogeneous growth of the ZnS shell resulting in an overall prolate like NC shape. This kind of elliptical NC shape can be found also for other core/shell NC systems with thick shells, where the shell growth along specific crystallographic directions is energetically favored [148]. The ellipsoidal shape

of nanoparticles can potentially lead to radiation polarization [148] and additionally allowed transitions forbidden in spherical QDs [149].

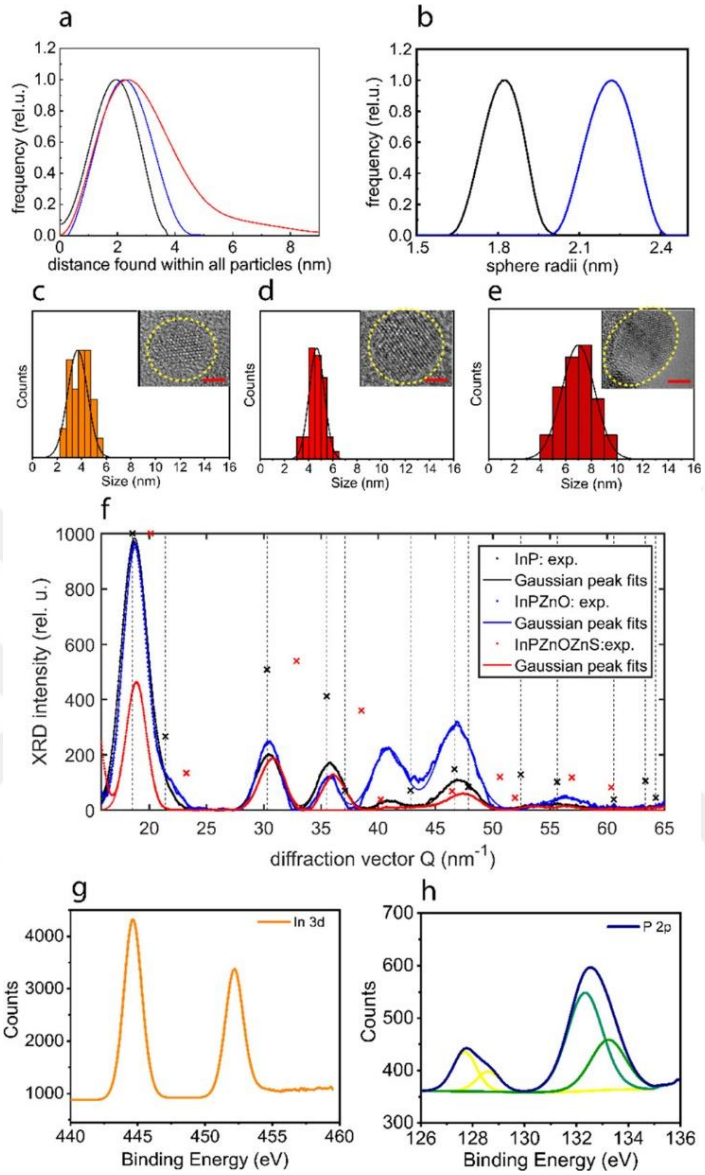

Figure 4. 3: (a) Pair distance distribution functions (PDDFs) of the InP core (black), InP/ZnO core/shell QD (blue) and QD-4ZnS core/shell/shell NCs (red) as resulting from the P(q)-curves shown in Appendix A. (b) Distributions of spheres that can describe the measured SAXS curves of the InP core and InP/ZnO- core/shell QDs. Size distribution histograms of the (c) InP core (inset: TEM image, scale bar is 2 nm), (d) InP/ZnO core/shell (inset: TEM image, scale bar is 2 nm), and (e) QD-4ZnS core/shell/shell NCs (inset: TEM image, scale bar is 2 nm) by HR-TEM measurements. Total number of 200 quantum dots are counted for size distribution. (f) XRD of InP, InP/ZnO and

InP/ZnO/4ZnS core/shell/shell NCs. XPS analysis of InP core QDs, (g) In 3d spectrum and (h) P 2p spectrum.

The crystal structure of the resulting QDs was investigated by analyzing the XRD patterns (see Figure 4.3f & Appendix A). The black vertical dashed lines and black crosses mark the positions of InP bulk peaks (ICDD 00-032-0452), the blue crosses of hexagonal ZnO (ICDD 00-036-1451), and the red crosses mark the positions of the cubic sphalerite phase of ZnS (a=5.4093 Å ICDD 00-65-0309), respectively. From the only core QDs, we observe that the crystal structure corresponds to zinc blende (a=5.869 Å, ICDD 00-32-0452). For InP/ZnO NCs, we still observed the InP zinc blende crystal structure, but due to the thin ZnO shell (~0.2-0.3 nm) its diffraction peak (ICDD 00-036-1451) cannot be detected. This is not surprising as only one monolayer (ML) shell material on a crystalline core can grow epitaxially by maintaining the lattice constant of the core [150]. For the InP/ZnO/ZnS NCs, a shift of the InP peaks occurred in direction of the position of ZnS in the cubic sphalerite phase (ICDD 00-65-0309). This shift can be explained by the situation that the first MLs of the ZnS-shell initially maintains epitaxial registry with the lattice parameter of InP and with subsequent ML of ZnS, tends to reach its bulk lattice constant [150]. Because of the cubic lattice constant of ZnS is smaller than that of InP, the InP core is compressively strained, reflected by peak shifts to larger Q-values or diffraction angles (see Figure 4.3f). Additionally, we observe different peak-shift values as well as peak width values for the InP core along different crystallographic directions, indicating that the influence of the ZnS shell on the InP core is not isotropic. This result is suggestive of asymmetric ZnS shell growth as already derived from the SAXS analysis.

XPS analysis was performed to confirm the elemental surface chemistry of the InP core, InP/ZnO core/shell, and QD-4ZnS core/shell/shell NCs, respectively. For the analysis, all of the peaks have been spectrally corrected according to the carbon-1s standard peak. For the InP core QDs, the In-3d spectrum exhibits two peaks located at 444.5 eV ($3d_{5/2}$) and 452.1 eV ($3d_{3/2}$) (Figure 4.3g and Figure 4.3h), which can be assigned to InP [151-153]. The P-2p spectrum shows two doublets, which are related to the two different chemical environments of the phosphorus atoms. The first pre-dominant doublet that present at 127.8-128.9 eV ($2p_{3/2}$) is the characteristic peak for InP [154, 155]. The doublet in 132.4 eV – 133.4 eV range is associated with the P atoms in an oxidized medium, most probably $InPO_X$ [151, 156]. In the XPS spectra of InP/ZnO core/shell QDs, the peaks corresponding

to Zn 2p are observed which indicates the Zn^{+2} bound to oxygen in the ZnO [157-159]. The Zn $2p_{3/2}$ and $2p_{1/2}$ peaks are at 1022.09 eV and 1045.8 eV, respectively (see Appendix A). For the InP/ZnO core/shell QDs, the In-3d peak shifts to higher binding energies located at 444.7 eV ($3d_{5/2}$) and 452.5 eV ($3d_{3/2}$), compared to the InP core QD (see Appendix A). Furthermore, shifting to higher binding energies located at 127.9 eV and 132.4 eV also occurs in P-2p spectrum (see Appendix A). Similarly, O-1s peak shifted to higher binding energy from 530.9 eV to 531.3 eV after formation of the ZnO shell coating (see Appendix A). The possible reason for this type of shifting is due to the additional oxidation process during the ZnO shelling procedure [151]. For the QD-4ZnS core/shell/shell NCs the S-2p spectrum exhibited two peaks located at 161.2 eV-162.6 eV (see Appendix A). It was previously reported that these binding energies are associated with S^{2-} anions present in the ZnS [151, 160, 161]. In addition, after the ZnS shell formation, In-3d peaks shifted to lower binding energies located at 444.4 eV ($3d_{5/2}$) and 452.0 eV ($3d_{3/2}$) (see Appendix A). Similarly, binding energies of Zn-2p and O-1s (see Appendix A) had also displaced to lower values after ZnS shelling due to decrease of the InP-O bonds formed by oxidation [162].

4.2.4 Ultra-fast decay dynamics

The effect of shell growth on the ultrafast decay dynamics and the nonlinear absorption of QDs was further investigated by using femtosecond pump-probe spectroscopy [34, 163]. In the experiments, the QD solutions (InP core, InP/ZnO core/shell, and QD-4ZnS core/shell/shell NCs) were excited with a 320-nm, femtosecond pump pulses (incident fluence is 480 $\mu J.cm^{-2}$) and the difference between the pumped and unpumped absorbance (ΔA) of the QDs was measured over the 450-800 nm spectral range by using a femtosecond visible continuum probe. Figure 4.4 summarizes the results of the femtosecond transient absorption (TA) measurements. Measured ΔA spectrum, temporal evolution of ΔA at the wavelength of maximum bleaching, and 2-dimensional variation of ΔA as a function of probe delay and wavelength are shown in Figure 4.4a-c, Figure 4.4d-f, and Figure 4.4g-i for InP, InP/ZnO, and QD-4ZnS NCs, respectively. The peak wavelength of the measured ΔA spectra of the QDs exhibited a red-shift as a function of the probe delay due to the intra-band decay of the excited carriers to the conduction band edge [164] (Figure 4.4a, Figure 4.4d, and Figure 4.4g). The TA measurements showed that for the InP core, the steady state absorption peak wavelength was at 490 nm and the

peak wavelength of bleach was at 520 nm (Figure 4.4a). However, after the growth of ZnO or ZnS shell over InP core, the peak wavelengths of steady-state absorption and bleach became nearly equal (Figure 4.4a, Figure 4.4d, and Figure 4.4g), which can be explained based on the reduction of the biexciton and carrier-trap induced stark effect [165]. The ultrafast temporal evolution of the carriers was further investigated for probe wavelengths at which the measured ΔA showed the maximum amount of bleach (520 and 585 nm) for the InP, InP/ZnO, and QD-4ZnS NCs. As can be seen from Figure 4.4b, Figure 4.4e, and Figure 4.4h, following an initial rise, a bi-exponential decay occurred, which could be characterized by the decay times τ_1 and τ_2 [166, 167]. Here, the decay times τ_1 and τ_2 are due to shallow and deeper traps, which originate due to the P and In dangling bonds [100]. The decay times of τ_1 and τ_2 for the InP, InP/ZnO, and QD-4ZnS NCs were determined by performing a bi-exponential fit to the measured ultrafast decay data. The fit results showed that τ_1 and τ_2 both increased from 1 to 1.5 ps and from 65.7 to 76.5 ps, respectively, after the shell growth of ZnO on the InP core. Furthermore, for the case of QD-4ZnS NCs, τ_1 and τ_2 became 3.4 and 84.3 ps, respectively, indicating further passivation of the shallow and deeper traps as a result of shell growth [165, 168-170]. Note that the measured ΔA did not vanish completely for the longest probe delay of 80 ps, since the carrier recombination for the QDs occur over ns time scales (see Appendix A).

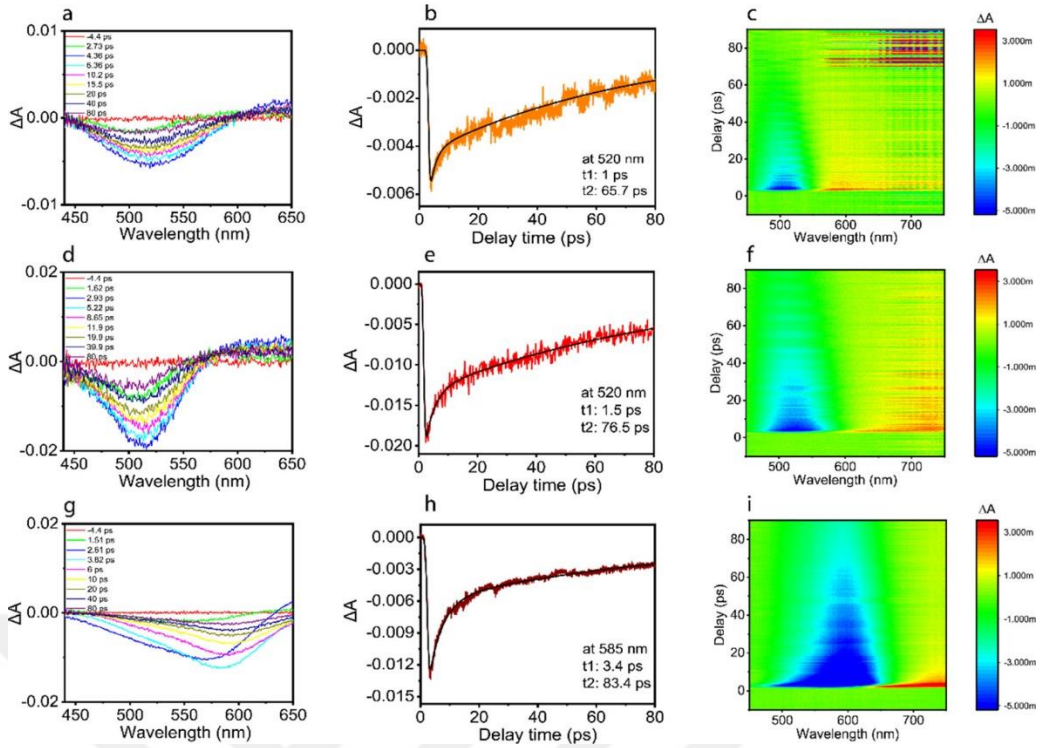

Figure 4. 4: Measured ΔA spectrum, temporal evolution of ΔA at the wavelength of maximum bleaching, and 2-dimensional variation of ΔA as a function of probe delay and wavelength for: InP core (a)-(c), InP/ZnO (d)-(f), and QD-4ZnS (g)-(i) NCs for InP, InP/ZnO, and QD-4ZnS NCs, respectively. Measured transient absorption spectra of (a) InP core; (d) InP/ZnO and (g) QD-4ZnS at different probe delays. The excitation wavelength was 320 nm. The measured peak wavelength of the nonlinear absorption changed and matched the bleach peak after the shell growth which can be explained by the reduction of the carrier-trap induced stark effect. (b), (e) and (h) show the measured and fitted temporal evolution of the carrier decay times at the probe wavelengths of 520 nm and 585 nm. For the InP core the first excitonic peak was at 520 nm and the τ_1 and τ_2 values were determined to be 1 and 65.7 ps. The ZnO shell growth reduced the trap states and hence, τ_1 and τ_2 increased to 1.5 and 76.5 ps, respectively. The multiple ZnS shell growth caused further trap passivation, resulting in short (τ_1) and long (τ_2) lifetimes of 3.4 and 84.3 ps, respectively. (c), (f) and (i) surface plots of the measured ΔA with respect to the probe delay and wavelength.

4.3 LED application

To prevent any efficiency drop due to host material effect, we designed an architecture [62] that can maintain QD solution in liquid-state on top of the blue LED (Figure 4.5a).

For that we used a transparent polymeric lens made of polydimethylsiloxane (PDMS) due to its scalable and low cost fabrication [171, 172]. We placed the lens on top of the blue LED chip and sealed the edges with the UV-curable polymer. After the curing process was finished, we injected red-emitting QDs by using a microsyringe into the blue LED capped with a PDMS polymeric lens. When the blue LED is turned on, the blue electroluminescence generated from the blue LED die optically pumps the QDs in solution-state, which generates photoluminescence in the red spectral region (Figure 4.5a and Figure 4.5b). To analyze the optical performance of the fabricated QD-LED, we injected the QD solution with different optical densities. While the optical density increases, red emission becomes stronger in comparison with the blue electroluminescence (Figure 4.5c). Finally, the (x,y) tristimulus coordinates reached to red region on the CIE chromaticity diagram by integrating QDs with an optical density of 0.4 (Figure 4.5d). The intensity spectra remained almost constant with a slight change of the PL peak position of 3 nm while the current injection level increases from 5 mA to 150 mA (Figure 4.5e). The EQE was measured as 28.6%, 25.3%, 19.2%, 13.4% and 9.43% for the optical densities of 0.04, 0.07, 0.13, 0.20 and 0.4, respectively. Moreover, PCE is calculated by the relation of $PCE=\eta_{ext.}\lambda_{1.}(\lambda_2)^{-1}$ (Equation (4.1)) [173] where λ_1 and λ_2 are the emission peak wavelength of the blue EL and emission peak wavelength of the QDs, respectively. PCE of LEDs corresponded to 21.62%, %, 18.85%, 13.99%, 9.85% and 6.86% for the respective OD values, respectively.

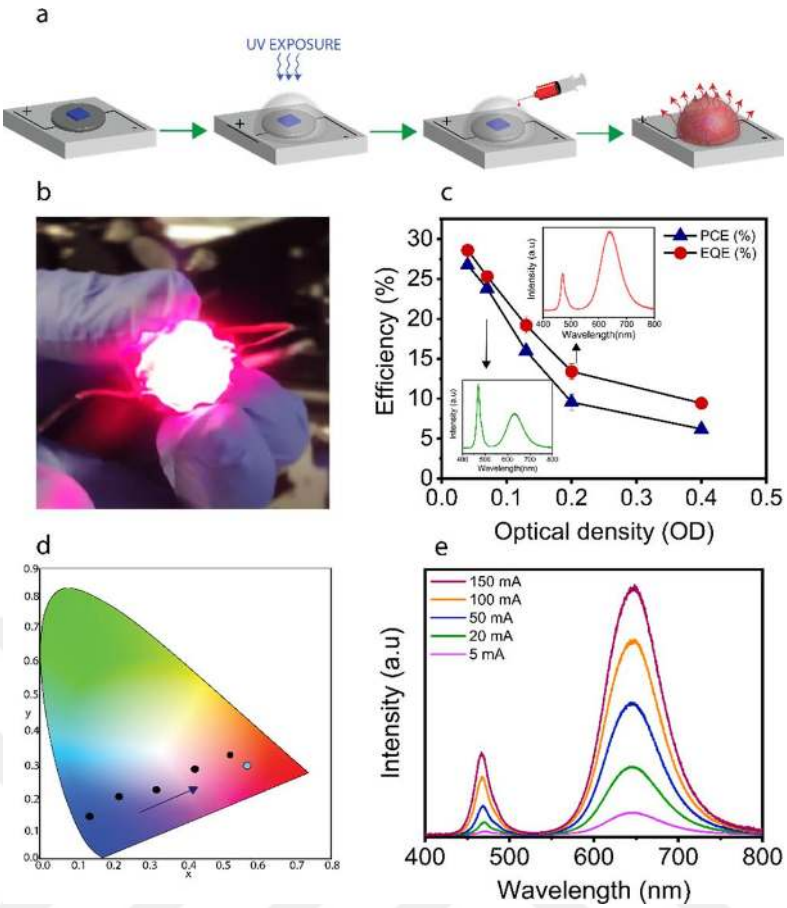

Figure 4. 5: (a) Schematic of the QD based LED fabrication. (b) Photograph of the LED when it is turned on. (c) PCE (%) and EQE (%) at different OD values. Inset: Intensity spectra of red-emitting QD-based LEDs at different optical densities of 0.07 and 0.2. (d) The (x,y) color coordinates of the QD-LEDs at different optical densities with an injection current of 10 mA. (e) Intensity spectra of the red-emitting QD-based LED with the optical density of 0.4 at different current injection levels ranging from 5 mA to 150 mA.

To date, in terms of type-II QD based LED studies, Jin *et al.* synthesized green-emitting alloyed $Cd_xZn_{1-x}S$/ZnSe type-II QDs and these LED results demonstrated EQE of 8.78% [129]. Moreover, Lin *et al.* reported deep-red LEDs based on CdTe/CdSe core/shell QDs with a maximum EQE of 6.19% [18]. Instead of cadmium-based QDs, Karatum *et al.* integrated InP/ZnO core/shell QDs as an emissive layer into LED application resulting in EQE of 0.53% [138]. Comparatively, the LED using InP-based type-II QDs in this study reached to EQE level approaching to 10% due to the high efficiency in synthesis batch and conserving their efficiency levels by direct integration in liquid state.

4.4 Conclusion

In summary, we demonstrated cadmium-free and efficient type-II InP/ZnO/ZnS core/shell/shell QDs. For that, initially InP core QDs with emission in the red spectral region were synthesized by hot injection technique. Then, the sequential growth of ZnO and ZnS shells led to a high PLQY of 90.8%. ZnO and ZnS shell formation was confirmed by optical analysis that is supported by quantum mechanical simulations. Moreover, SAXS measurement showed that the ZnS shell induced the transition of the nanocrystal ensemble from spherical to elliptical shapes. Finally, we integrated the core/shell/shell QDs into LED die in liquid form to reduce host-material effect. The fabricated liquid-LED device demonstrated 9.4% of EQE and 6.8% of PCE, respectively, which is the most efficient type-II QD based LED reported to date. Type-II QDs show high promise for future bioimaging, display and laser applications.

Chapter 5: Ruthenium Doped InP QDs For Efficient Red Emission

This section is based on the publication ''*Ruthenium Doped InP Quantum Dots for Efficient Red Emission''* G. O. Eren, A. Onal, O. Karatum, H. Jahangiri, M. S. Ozer, Z. Eroglu, B. Sundu, L. Kaya, A. B. Burcak, U. Aydemir, O. Metin, A. Sennaroglu, and S. Nizamoglu, *ACS Applied Nano Materials* 6.12 (2023): 10044-10053. Reproduced (or "Reproduced in part") with permission from American Chemical Society Copyright 2023.

The synthesis of various transition-metal doped InP quantum dots (QDs) such as copper, manganese, and silver for enhanced optoelectronic properties has been reported to date. Herein, we introduce ruthenium doping into InP QDs. After the Ru doping, InP QDs showed a significant red-shift up to 325 meV due to the introduction of mid-gap states. The optimization studies of the ZnS shell formation on Ru-doped InP core QDs led to a high photoluminescence quantum yield (PLQY) of 77.6% in red spectral region, while without ruthenium doping the PLQY reached a maximum level around 60% via the same synthetic approach. Elemental mapping, mass spectrometry, and lattice change confirmed the incorporation of ruthenium inside the InP QDs. Moreover, the integration of Ru-doped QDs into LED in liquid matrix led to an external quantum efficiency (EQE) of 7.9%. This study demonstrates that ruthenium doping can be an alternative strategy for efficient red emitters.

5.1 Introduction

Colloidal semiconductor quantum dots (QDs) have gained significant industrial and academic interest for a wide variety of applications such as light-emitting diodes (LEDs), lasers, luminescent solar concentrators (LSC), solar cells, and photocatalysts [13, 116, 174-179]. The interest in the QDs mainly originates from their tunable energy levels, which can be controlled via quantum confinement effect, alloying and ligand engineering. Besides, transition-metal ion doping of QDs is one of the most effective strategies to add new and enhanced properties. It can be achieved by kinetic factors at relatively low synthesis temperatures (<400° C) [36] and leads to high photoluminescence quantum yield (PLQY) [34, 180], improved thermal and chemical stability [19, 181], longer radiative lifetime [181], reduced self-absorption [182], and tunable emission spectral width [37] depending on the choice of the dopant.

To date, cadmium-based host materials have been doped with different transition metals [166, 183, 184]. However, cadmium suffers from its inborn heavy-metal toxicity, which raises concerns for its practical use [130]. As non-toxic alternatives, zinc chalcogenide QDs (e.g., ZnSe, ZnSeTe, ZnS) were used for different transition-metal doping [181, 185-187], but their spectral tunability range is limited up to the orange spectral range. Instead, indium phosphide (InP) possesses great potential as environmentally benign and non-toxic host material for QD-based technologies [188, 189]. To date, incorporation of Cu, Mn, and silver (Ag) into InP QDs [19, 20, 108-110] have been investigated, but to the best of our knowledge ruthenium (Ru) ion doping into InP QDs has not been explored yet, which has been a popular element for supercapacitors [190, 191], catalysis [22] photodynamic therapy [192, 193], and optoelectronic neural interfaces [194, 195]. Similar to other transition-metals, by introducing Ru as a dopant ion into the host semiconductor nanocrystal, it is possible to generate efficient centers for the recombination of the excited carriers in the bandgap of the semiconductor. Furthermore, ruthenium doping can enhance the photocatalytic activity of semiconductor QDs [196].

In this section, we introduce ruthenium doping into InP quantum dots. The X-ray-based techniques (X-ray diffraction (XRD), X-ray photoelectron spectroscopy (XPS), and energy dispersive X-ray analysis (EDX)) confirmed the doping of ruthenium into the InP structure. To decrease the surface traps and increase the PLQY, a zinc sulfide (ZnS) shell was grown on ruthenium doped InP structure. Optimization of ruthenium doping and ZnS shell led to a high PLQY of 77.6% in red spectral range. Finally, Ru:InP/ZnS core/shell QD solutions were integrated into a LED device architecture and the resulting red LED exhibited an external quantum efficiency (EQE) of 7.9%. Doping of InP QDs with ruthenium points out an alternative strategy for efficient red emitters.

5.2 Results and Discussion

5.2.1 Synthesis of Ru-doped InP quantum dots

Green-emitting InP (G-InP) QDs were synthesized via the hot injection of tris(trimethylsilyl)phosphine $P(TMS)_3$ into indium chloride ($InCl_3$) containing organic solution in the presence of stearic acid (SA) and hexadecylamine (HDA) surfactants under argon environment [180]. Next, ruthenium acetylacetonate ($Ru(acac)_3$) was injected into the as-synthesized InP QDs and the resultant mixture was heated to 230° C for ensuring

Ru doping. To reduce the surface trap states and increase the PLQY of the QDs, a ZnS shell was grown on the yielded Ru-doped InP QDs via injection of zinc oleate and sulfur (S) in trioctylphosphine (TOP) into the QDs solution at 160° C via dropwise (at a rate of 2 mL/h) and following heating up the mixture to 220° C (Figure 5.1).

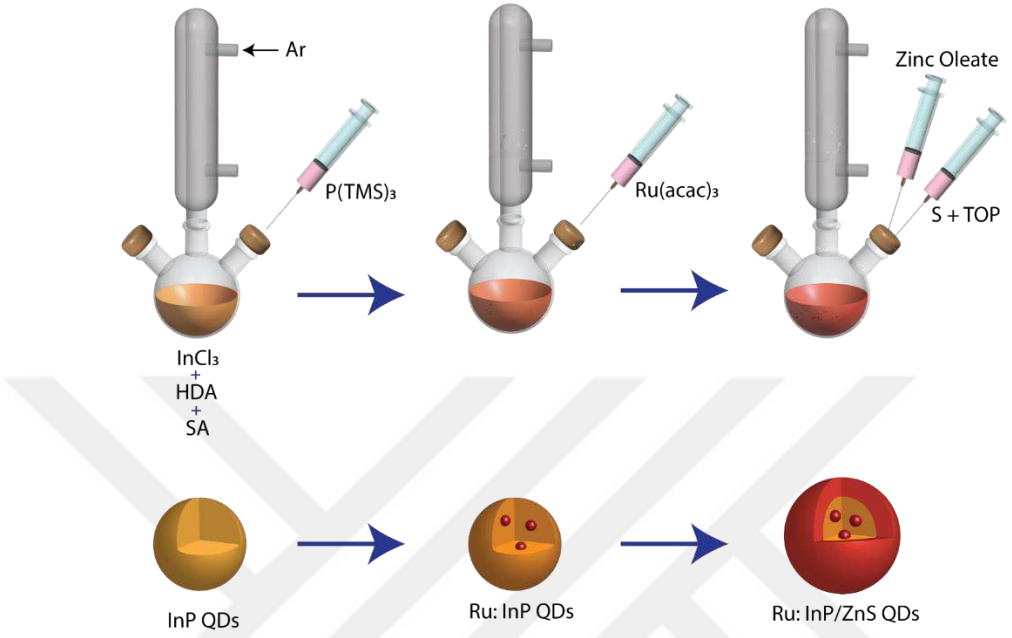

Figure 5. 1: Schematic illustration of the synthesis process.

The average size of the spherical G-InP QDs was calculated as 2.82 nm (Figure 5.2a). After the introduction of the Ru dopant at Ru:In ratio of 0.003, the size of the QDs slightly increased to 2.94 nm (Figure 5.2b). Upon the growth of ZnS shell, a clear increase in the size of the core/shell QDs was observed and they exhibited an average size of 5.83 nm (Figure 5.2c), indicating the formation of ZnS shell with an average shell thickness of 1.45 nm, which equals 4.6 monolayers (ML), on Ru-doped InP QDs [197].

5.2.2 Structural characterization

To confirm the successful doping of Ru into the G-InP QDs, we performed scanning TEM (STEM) energy-dispersive X-ray spectroscopy (EDX) elemental mapping analysis (Figure 5.2d). The signals of Ru are clearly observed in the QDs along with In and P. To further investigate the presence of Ru dopant in the InP crystal structure, inductively coupled plasma mass spectrometry (ICP-MS) analysis for the Ru:InP QDs (Ru:In ratio of 0.003) was performed. The measurements showed that In:Ru:P weight ratio was 0.36:0.005:0.071 showing the presence of Ru inside InP QDs (see Appendix B). XRD

patterns of the InP core, Ru:InP, and Ru:InP/ZnS core/shell QDs are shown in Figure 5.2e. The broadened diffraction peaks of all samples are observed due to the small size of the QDs. The XRD pattern for InP core QDs exhibited three well-defined peaks observed at 2θ values of 26.70º, 44.09º, and 52.58º, attributing to the (111), (220), and (311) planes of the zinc-blende crystal structure of InP (JCPDS32-0452). After the Ru incorporation (Ru:In ratio of 0.003), the diffraction peaks shifted to lower 2θ values of 26.54º, 43.90º, and 52.28º that indicate lattice filling of Ru dopant at the interstitial sites of the InP host structure [198, 199]. Furthermore, the lattice constant slightly increased from 5.822(9) Å to 5.830(5) Å due to the small amount of Ru doping concluded by ICP-MS. Such a small change does not significantly affect the lattice mismatch between the core and shell. For InP core and Ru:InP QDs, we observed an additional peak around ~33º which is related to indium oxide (In_2O_3) (JCPDS06-0416) (Figure 5.2e). We consider that rapid oxidation of InP QDs and their transformation into In_2O_3 was realized upon their exposure to air after synthesis process [200]. After the ZnS shell growth on the Ru-doped InP QDs, the diffraction peaks shifted toward higher 2θ values (26.79º, 45.21º, and 53.22º, respectively) of the cubic ZnS phase (JCPDS 80-0020). Furthermore, no diffraction peaks of separate ZnS phase is observed, indicating that ZnS shell successfully formed on Ru:InP QDs [201]. XRD and TEM results of Ru doped InP (G-InP) at higher Ru:In ratios (0.005 and 0.01) are also given in Appendix B, indicating the similar trends for Ru:InP sample with Ru:In ratio of 0.003.

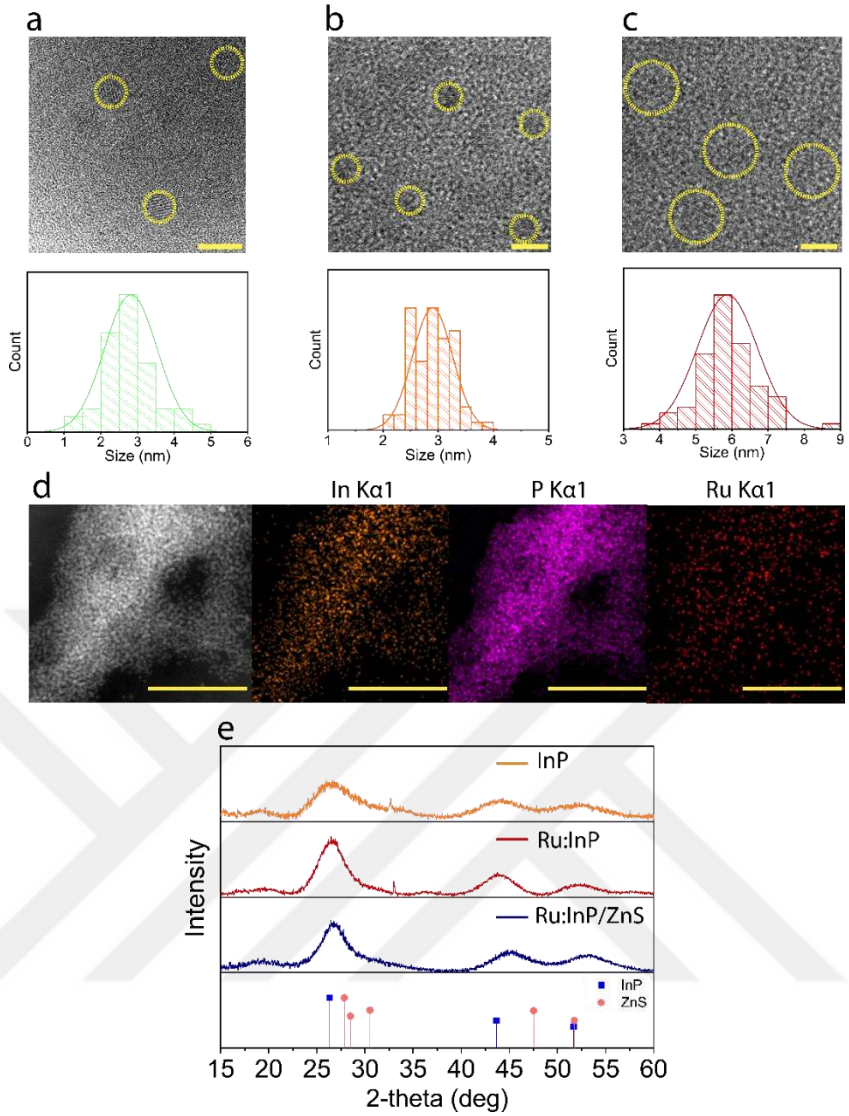

Figure 5. 2: HRTEM and size distribution of the synthesized (a) G-InP core (2.82 nm ± 0.45), (b) Ru:InP (2.94 nm ± 0.37) (Ru:In ratio of 0.003), and (c) Ru:InP/ZnS core/shell QDs (5.83 nm ± 0.81). For the particle size distribution, a minimum of 200 particles were counted. The scale bar of the HRTEM images is 5 nm. (d) STEM image and EDX elemental maps of In, P, and Ru. The scale bar is 100 nm. (e) XRD pattern for the InP core, Ru:InP (Ru:In ratio of 0.003), and Ru:InP/ZnS core/shell QDs that have the final PLQY of 77.6%.

5.2.3 Optical characterization

After the structural characterization of the synthesized materials, the effect of Ru doping on the optical properties of InP/ZnS QDs was investigated. First, it is reported that InP QDs doped with transition metals such as Ag, Cu and Mn showed enhanced PLQY due

to the lattice incorporation of the dopants [19, 20, 41]. While the PLQY of G-InP QDs were around 2%, after Ru doping, the PLQY increased to 26.7% with Ru:In injection ratio of 0.003. We consider two potential mechanisms that can increase the PLQY of the InP core QDs after ruthenium doping. First, it is previously shown that oxides (e.g., ZnO) on InP can increase the PLQY of the core QDs [106, 201]. Hence, the measured Ru-O-P oxide phase on the surface of QDs (see discussion part) may also increase the PLQY of the InP core QDs. In addition, the potential diffusion of the dopant ions from the surface to the inside of QDs can passivate the nonradiative traps. Such enhancement is also observed for copper [19], manganese [202], and silver [203] doping as well . Moreover, as a control group, we also synthesized InP QDs without Ru. In this regard, we followed the same procedure as conducted for the Ru doping process and we only observed a PLQY of only 10.5% with a slight change (Figure 5.3a). Hence, this finding suggests that like other dopant ions, Ru doping also suppresses non-radiative recombination centers of QDs and increases PLQY [204].

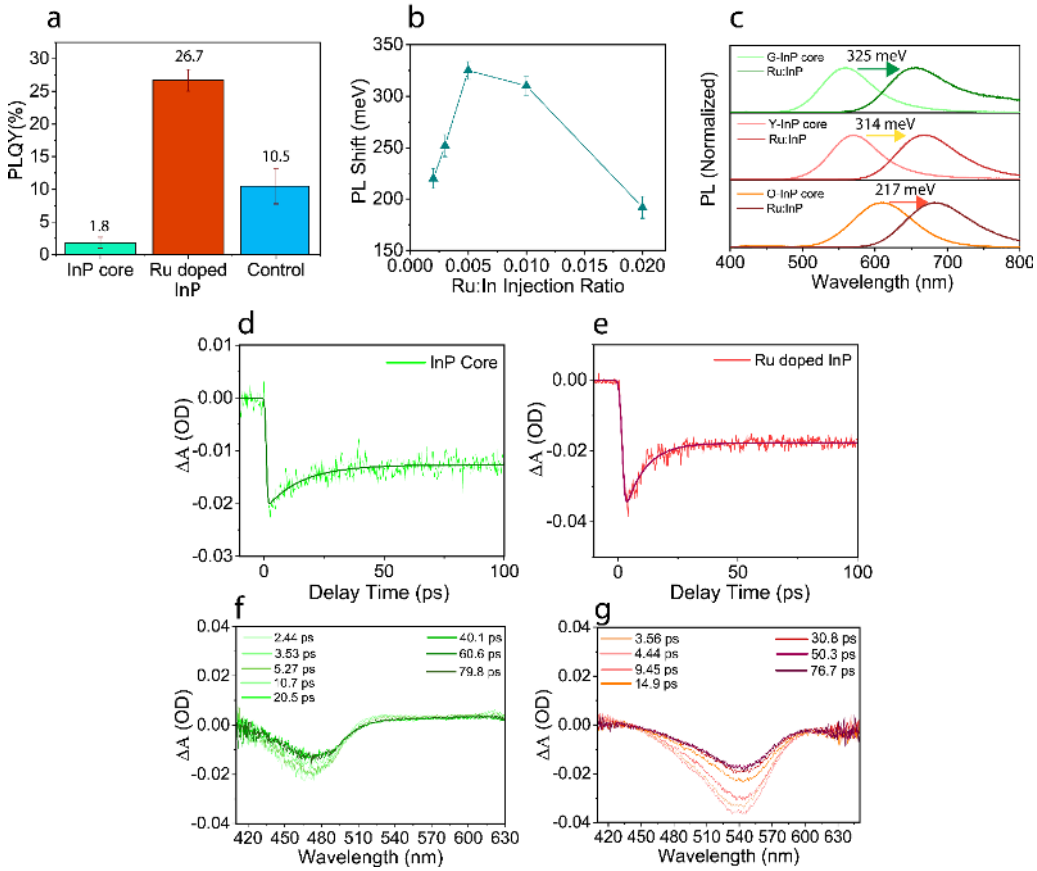

Figure 5. 3: (a) PLQY comparison between InP core, Ru:InP (Ru:In ratio of 0.003), and control group (InP core without addition of Ru dopant). (b) PL shift (meV) for G-InP

QDs at different Ru:In injection ratio. For the G-InP core QDs, the highest PL shift was 325 meV at Ru:In injection ratio (mmol) of 0.005. (c) PL peaks of G-InP, yellow-emitting (Y-InP), and orange-emitting (O-InP) core and maximum PL shift change (meV) after Ru doping at different Ru:In ratio. For the G-InP core QDs, the highest PL shift was 325 meV at Ru:In injection ratio (mmol) of 0.005, while for the Ru doped Y-InP and O-InP core QDs, maximum PL shift values were 314 meV and 217 meV with the Ru:In injection ratios of 0.01. (d) Measured variation of the nonlinear absorbance change (ΔA) as a function of the probe delay for InP QDs at 470 nm. (e) Measured variation of ΔA as a function of the probe delay for Ru-doped QDs at 540 nm. Measured variation of ΔA as a function of the (f) probe wavelength for InP QDs at different probe delays up to 80 ps, (g) probe wavelength for Ru-doped InP QDs at different probe delays up to 80 ps.

The effect of Ru doping on PLQY was investigated for the InP core QDs emitting at green, yellow, and orange spectral range (i.e, G- InP, Y-InP, O-InP) (see Appendix B). As a general trend, PLQY values dropped with increasing Ru:In injection ratio and we consider that loosely adsorbed dopant ions might start to act as non-radiative recombination centers at higher ratios, which decrease the PLQY [205]. Among different combinations, we selected the Ru:InP QD emitting at green (with the Ru:In ratio of 0.003), which exhibits a PLQY of 26.7% for further studies. We also evaluated the PLQY of doped and undoped QD samples before and after the purification and observed that the PLQY slightly increased after purification process (see Appendix B). After the Ru doping, additional mid-gap states are introduced into the energy levels of InP QDs [206] and thus, a significant redshift of the PL peak was observed from 559 nm to 655 nm, which corresponds to 325 meV with the Ru:In injection ratio of 0.005 (Figure 5.3b and Figure 5.3c). The excess Ru dopant (at higher Ru:In ratio) led to smaller redshift in PL emission, possibly due to the saturation of available sites for Ru doping and formation of excess oxidation layer on InP core surface (Figure 5.3b) [207]. For yellow and orange-emitting QDs, maximum PL shift values were 314 meV and 217 meV, respectively. Similarly, smaller redshift in PL emission was observed at higher Ru:In ratio for yellow and orange-emitting QDs (see Figure 5.3c & Appendix B). In the context of explaining the redshift mechanism in PL emission, we consider that Ru impurity is located above the valence band edge of the InP QDs based on its electronegativity [206], and thus the Ru dopant impurity state acts as a hole acceptor [206] similar to the Cu dopant [19, 208]. As

a result, the photo-generated holes at the Ru dopant level radiatively recombine with the electrons from the conduction-band of InP nanocrystals, resulting in a red shift of the Ru:InP QD PL emission [109, 208]. To further confirm this effect, ultrafast pump-probe spectroscopy of the undoped and Ru-doped InP QDs was studied, and a single-exponential fit was applied to compare the picosecond decay time (τ) of the QDs. In these measurements, the change ΔA in the nonlinear absorbance was measured as a function of probe delay and probe wavelength. For the undoped InP QDs τ was measured as 14.8 ps (Figure 5.3d), and for Ru-doped InP QDs τ decreased to 8.65 ps (Figure 5.3e), which is due to the introduction of the mid-gap states that increase the interband decay rates. Moreover, introduction of the Ru dopant led to the formation of the mid-gap state above the valence band edge of InP QDs giving rise to the observed red shift of the ΔA spectrum from 470 to 540 nm (Figure 5.3f and Figure 5.3g).

5.2.4 Optimization of quantum yield

Since efficient light generation is an important goal for a wide variety of optoelectronic applications such as lighting, bioimaging and lasing, the optimization of PLQY was performed. In this regard, to increase the PLQY of the Ru:InP QDs further, optimization studies of ZnS shell growth were performed by using controlled delivery of zinc-sulfur precursor solution into the reaction medium. The highest PLQY of 77.6% was observed for the Ru:InP/ZnS core/shell QDs at 30 min under the injection rate of 2 mL/h (Figure 5.4a). At longer times, PLQY value started to decrease due to interfacial strain effects, [137] and after 60 min it fell down below 50% (Figure 5.4a). The absorption and PL emission peaks of the optimized G-InP, Ru:InP, and Ru:InP/ZnS QDs showed red-shift after each step (Figure 5.4b). Moreover, we also checked the maximum-attainable PLQY of InP/ZnS core/shell QDs via the same synthesis approach and it was 61.2%, which is lower than the Ru-doped QDs. Similarly, in previous studies PLQY values up to 60% was reported [134]. Hence, ruthenium doping holds promise to obtain efficient red emitters.

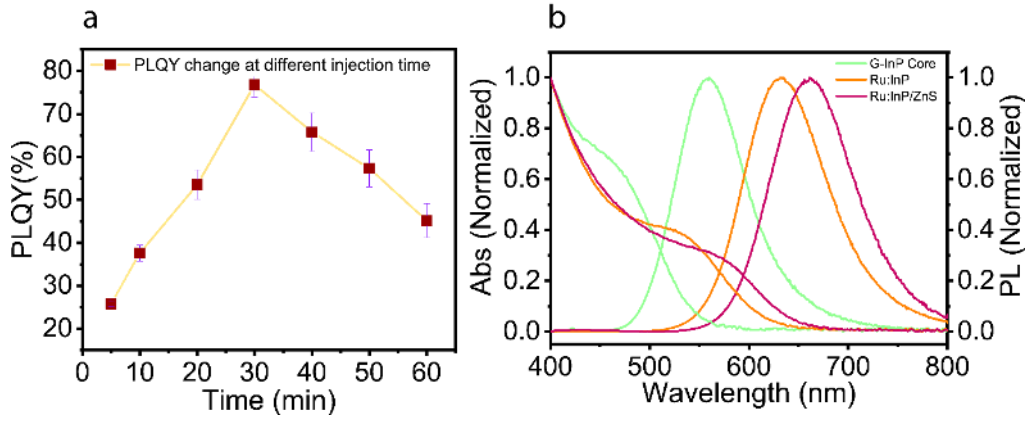

Figure 5. 4: (a) PLQY for different time intervals after ZnS shell precursor injection on Ru:InP (at Ru:In injection ratio of 0.003). (b) Absorbance and PL peaks of optimized G-InP core, Ru:InP (at Ru:In injection ratio of 0.003), and Ru:InP/ZnS core/shell QDs.

5.3 Ru:InP/ZnS core/shell quantum dot-based LED

We selected lighting as a potential application for Ru doped InP/ZnS core/shell QDs. For that, we integrated the QDs on blue LED chips (with a wavelength of 460 nm) in liquid state to conserve the PLQY and reduce the host material effect [44, 201]. We selected polydimethylsiloxane (PDMS) elastomer to prepare transparent polymeric lens due to its scalable and low-cost production [62]. Moreover, PDMS can recover its surface after the injection and hold the liquid on top of the blue LED chip without any leakage. After the production of polymeric lens, the lens on top of the blue LED chip was placed and sealed the edges by UV-curable polymer. Once the curing process is finished, we injected the Ru:InP/ZnS core/shell QDs in toluene using a micro syringe (Figure 5.5a). When the blue LED is turned on, the blue electroluminescence generated from the blue LED die optically pumps the QDs in the solution state, generating photoluminescence in the red spectral region (Figure 5.5b). As the optical density increased, the (x, y) tristimulus coordinates shift toward the red region on the chromaticity diagram (Commission International de l'Eclairage, CIE) and at the optical density of 0.94, strong red emission was observed. The change in the (x, y) tristimulus coordinates (Δx and Δy) were measured as 0.42 and 0.19, respectively, when the optical density increased from 0.15 to 0.94 OD (Figure 5.5c). We analyzed the optical performance of the fabricated LED at different OD levels and the external quantum efficiency (EQE) (Figure 5.5d) was measured according to Equation B.1 (see Appendix B) [209]. The resulting EQE dropped due to re-absorption while the

optical density increased and finally the red LED had an EQE of 7.9%. We also observed that the spectral profile did not significantly change when the current injection level increases from 5 to 100 mA (Figure 5.5e).

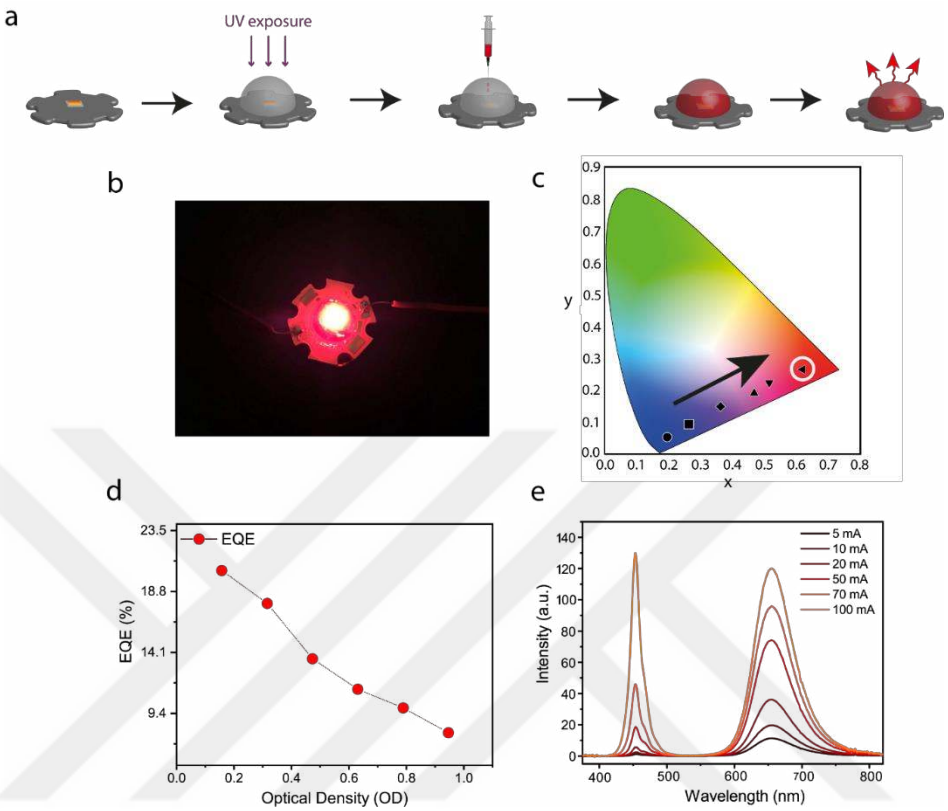

Figure 5. 5: (a) Schematic illustration of LED fabrication incorporating QD liquid. (b) Image of QD-LED when LED is turned on. (c) (x, y) color coordinates of the QD-LEDs at different optical densities. (d) EQE of Ru doped QD integrated LED at different optical densities. (e) Intensity spectra of the Ru:InP/ZnS QD-based LED with an optical density of 0.94 at different current injection levels ranging from 5 to 100 mA.

We performed chemical stability tests on an LED integrated with Ru-doped InP/ZnS core/shell QDs and compared it with the LED using QDs without doping. To prevent any evaporation and lens interaction, blue LEDs were combined with QDs in a glass lens. The T50 lifetime for the Ru-doped InP/ZnS QDs was 1433 hours, indicating that they had a longer lifetime than undoped InP/ZnS QDs having T50 of 461 hours. Moreover, the shift of the CIE coordinates for the doped QDs (Δx= 0.011, Δy=0.009) is lower than the undoped ones (i.e., Δx= 0.019, Δy=0.021) (see Appendix B). The result shows that ruthenium doping of InP/ZnS can increase the stability of the LEDs.

5.4 Discussion

In terms of ruthenium doping mechanism, we proposed a three-step process, which includes the preparation of undoped QDs, then exposure to dopant ions and finally coverage with an additional shell [210]. We consider that the introduction of the dopants takes place via diffusion of ions from a ruthenium containing oxide phase. We investigated the oxidative phases on InP and we observed that the oxidation of the InP core QDs (i.e., $InPO_x$) realized due to the ketonization process at elevated temperatures, which is evidenced by XPS [93, 95]. For the InP core structure, the P-2p spectrum displays two doublets, corresponding to two distinct phosphorus chemical environments. The first doublet at 128.47 eV ($2p_{1/2}$) is the typical peak of InP QDs (see Appendix B) [93, 152] while the second dominant doublet with higher intensity at 133.03 eV ($2p_{3/2}$) is associated with an oxidized layer, mostly In-P-O interactions of $InPO_x$ phase (see Appendix B) [93, 156]. This process can be defined as the transformation of carboxylic acids (i.e., stearic acid in our synthesis) into ketones, releasing carbon dioxide and water as byproducts [211]. Therefore, the ketonization provides oxidative conditions, which affect the chemical and physical properties of the InP QDs. After introducing the Ru precursor into the system, $Ru(acac)_3$ decomposes to RuO_2 and acetylacetonate at elevated temperature [212]. Afterwards, due to their similar electronegativity values (Ru:2.20, P:2.19), they form a complex bridge with oxygen (Ru-O-P), resulting in a decrease in binding energy of $InPO_x$ phase related P-2p spectrum ($2p_{3/2}$) (see Appendix B). Moreover, oxidized form of ruthenium is also observable with the binding energies of Ru-3d and 3p peaks at 280.06 eV and 461.98 eV, respectively (see Appendix B) [213]. We assume that the forming of Ru-O-P complex bridges also caused this binding energy shift. In brief, XPS results demonstrates that the ruthenium dopant is doped with oxidation state +4 (Ru^{+4}) inside the InP nanocrystal structure [213, 214]. After the ZnS shell growth at elevated growth, ruthenium is still observable showing the incorporation of ruthenium into the QDs. In addition, for the Ru:InP/ZnS, the Zn $2p_{3/2}$ and $2p_{1/2}$ peaks are at 1021.59 eV and 1044.64 eV (see Appendix B); whereas S 2p spectrum exhibited two peaks located at 161.18 eV and 162.46 eV (see Appendix B), confirming the ZnS shell formation on Ru:InP core QDs [93].

Up until now, only a few reports have studied doped InP-based QDs for LEDs. Yang and co-workers synthesized dual emissive InP:Cu/ZnS/InP/ZnS QDs to use in LED

application as light converter material. The PLQY of multi-heterojunction nanostructure had a PLQY of 35% [32]. Further, Yang and co-workers demonstrated Ag doped InP/ZnS core/shell QDs with high PLQY up to 75% [20]. They integrated Ag:InP/ZnS core/shell QDs on a commercial gallium nitride (GaN)-based blue LEDs. Similar study of Ag doped InP/ZnS QDs with PLQY of 77% were reported by Yang and co-workers [215]. In our case, red-emitting ruthenium doped QDs show a PLQY of 77.6% at similar level of Ag doped InP/ZnS QDs [215] that have emission peak in the yellow spectral region. Therefore, we believe that doping of InP with ruthenium is an alternative technique to produce efficient red-emitters. In this regard, to further boost the efficiency of Ru:InP-based QDs in red spectral region, shelling strategies with ZnSe [216] and GaP [217] as intermediate layers between InP and ZnS might be effective approaches for future LED studies.

5.5 Conclusion

In conclusion, we demonstrated ruthenium doping into InP quantum dots for the first time. Ru doping enabled significant red shift of emission and increase in the interband decay rate. The optimization of Ru doping and ZnS shell growth facilitated a high PLQY. Ru doping was structurally confirmed via XRD, EDX, XPS and ICP-MS. Finally, we applied QDs for lighting application. Ruthenium doping emerges as an alternative strategy for emission in red spectral range. Moreover, there exists significant room to grow a wide variety of shells such as ZnSe, ZnO, GaP to further engineer the optoelectronic properties for targeted applications.

Chapter 6: Antibacterial Activity of Type-II InP/ZnO QDs Against Bacterial Infections

The lack of new antibiotics has worsened the issue of antibiotic-resistant bacteria which are a threat to global health around the world. Therefore, considerable novel research against antibiotic-resistant bacteria have been conducted. Recent advances in nanotechnology and chemistry have paved the way for novel materials to be used in this field. Colloidal semiconductor QDs offer great potential as effective photocatalyst against antibiotic-resistant bacteria infections due to their high capacity of producing reactive oxygen species (ROS). In this study, we synthesized environmentally benign InP/ZnO core/shell QDs which have quasi-type-II heterostructure with multiple ZnO shell growth using hot-injection technique. In order to separate the charge carriers effectively and enhance the photocatalytic activity, we performed a ligand exchange, replacing oleylamine (OLA) with short-chain sulfide (S^{-2}) ligand. The highest ROS production was obtained by InP/1ZnO core/shell QDs compared to InP/2ZnO and InP/3ZnO QDs. As a result, under low intensity green light stimulation (3 $mW.cm^{-2}$) the optimized core/shell QDs (sulfide-capped InP/1ZnO) displayed high antibacterial activity of 99% inhibition against *Pseudomonas aeruginosa.*

6.1 Introduction

The emergence of antibacterial drug resistance is one of the most significant health concerns of the twenty-first century [218]. According to a recent study from the World Health Organization (WHO), antibiotic-resistant bacteria kill about 700,000 people every year, and this number is expected to rise to 10 million by 2050 [7]. Among the antibiotic-resistant bacteria, *Pseudomonas aeruginosa* which has the capacity to infect various parts of body such as blood and lungs poses a significant risk to human health [219, 220].

Semiconductor-based photocatalysis is emerging technique as effective antibacterial protection application [4, 11]. The photocatalysis mechanism of the semiconductor materials is based on the generation of reactive oxygen species (ROS) such as singlet oxygen ($^1O_2$), superoxide ($^{\bullet}O_2^-$), hydroxyl radical ($^{\bullet}OH$), and hydrogen peroxide (H_2O_2) after excitation of the photocatalyst [68]. More recently, there has been a growing interest in colloidal semiconductor QDs for the treatment of antibiotic-resistant bacteria. To date, various types of colloidal QDs have been introduced for antibacterial application,

including InP [15], ZnO [221], CdTe [222]. However, antibacterial activity of the type-II based QDs, in which electron and hole wavefunctions are spatially separated, have not been studied yet.

In this study, we demonstrated InP/ZnO core/shell QD which has quasi-type-II heterostructure as an effective antibacterial agent. In this regard, first, we synthesized the InP core by hot-injection technique. Then, we grew multiple ZnO shells on the InP core structure by thermal decomposition process to obtain quasi-type-II heterostructure, enabling electron and hole wavefunctions are spatially separated. For the antibacterial application, we performed ligand exchange by replacing oleylamine (OLA) with sulfide ligand. We observed that sulfide-capped InP/1ZnO core/shell QDs exhibited highest ROS generation, including superoxide ($^{\bullet}O_2^-$), hydroxyl radical ($^{\bullet}OH$); whereas sulfide-capped InP/2ZnO and InP/3ZnO QDs exhibited lower ROS generation efficiency. Thus, for the antibacterial studies we used the InP/1ZnO core/shell QDs and they displayed high antibacterial activity of 99% inhibition against *Pseudomonas aeruginosa* under low intensity green light stimulation (3 $mW.cm^{-2}$).

6.2 Results and discussion

6.2.1 Synthesis and structural characterization of InP and InP/ZnO QDs

InP core QDs were synthesized by hot-injection technique of tris(trimethylsilyl)phosphine ($P(TMS)_3$) on indium chloride ($InCl_3$) at elevated temperature in the presence of the oleic acid (OA) and oleylamine (OLA) ligands with the 1-octadecene (ODE) solvent. ZnO shell growth was performed via thermal decomposition process of zinc acetylacetonate monohydrate [$Zn(acac)_2.xH_2O$] [223]. For the consecutive ZnO shelling growth, shell precursor solution was added into the reaction mixture at 100º C and temperature is increased to 245º C. The schematic figure of the resulting core/shell QDs was illustrated in Figure 6.1a. The diffraction peaks are observed at 2θ values of 25.86º, 43.35º, and 51.78º corresponding to (111), (220), and (311) planes, respectively, indicating that cubic zinc blende structure of InP remained after ZnO shell growth (Figure 6.1b). Transmission electron microscopy (TEM) images showed that after first ZnO (1-ZnO) shell the size of QDs increased from 3.05 nm ± 0.35 to 3.54 nm ± 0.42, indicating that 0.49 nm shell was grown (see Figure 6.1c and Figure 6.1d). The formation

of a third ZnO (3-ZnO) shell led to the increase in size of QDs to 6.25 ± 0.73 nm (Figure 6.1e).

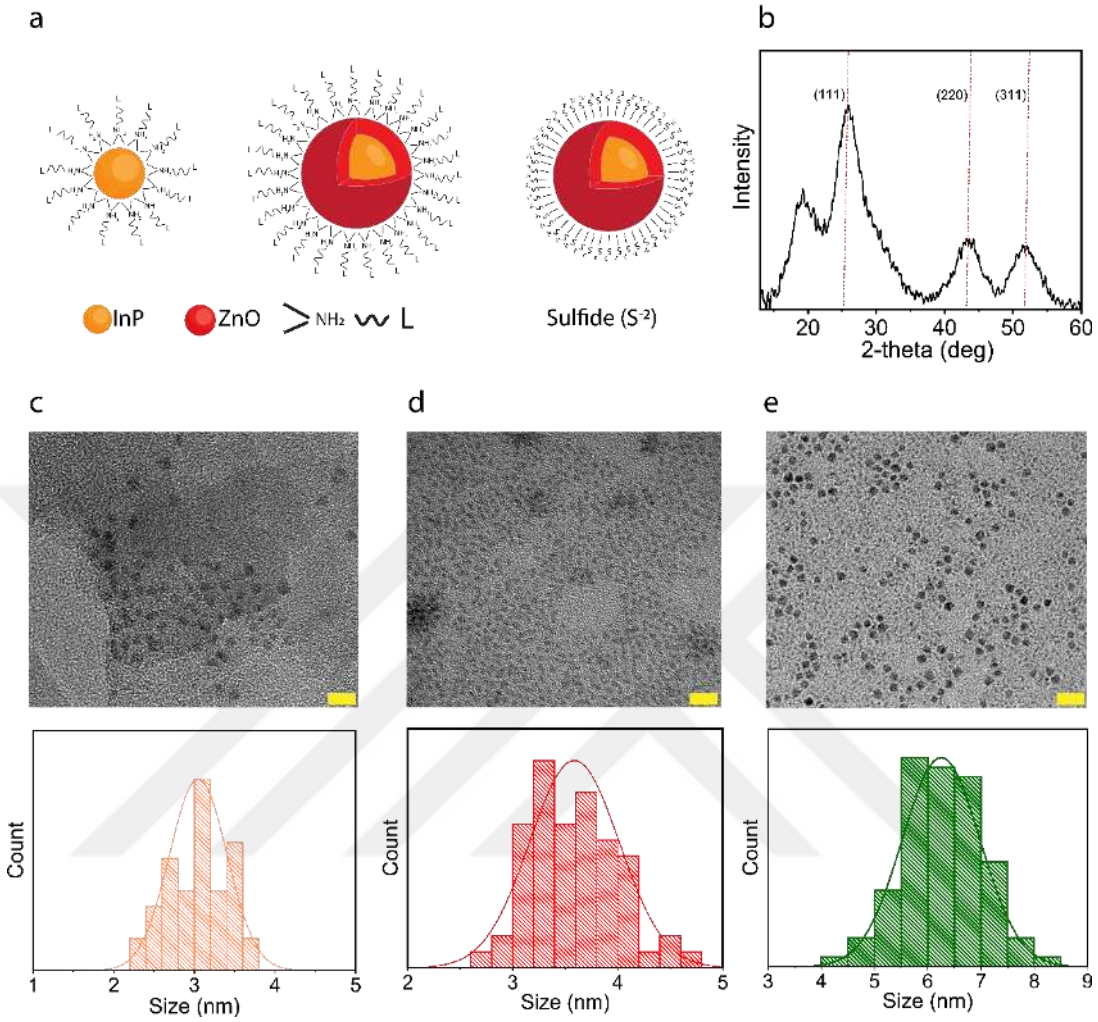

Figure 6. 1: (a) Schematic illustration of InP/ZnO core/shell QDs before and after ligand exchange. (b) X-ray diffraction pattern of InP/ZnO core/shell QDs. TEM images and size distributions of (c) InP core (3.05 nm ± 0.35), (d) InP/1ZnO (3.54 nm ± 0.42), and (e) InP/3ZnO core/shell QDs (6.25 ± 0.73 nm). For the particle size distribution, a minimum of 200 particles were counted. The scale bar is 10 nm for InP core TEM image, while for InP/1ZnO and InP/3ZnO QD TEM image the scale bar is 20 nm.

To investigate the chemical composition of as-synthesized InP core and InP/ZnO core/shell QDs we conducted X-ray photoelectron spectroscopy (XPS) measurement (Figure 6.2). For the analysis, binding energies in the XPS data were calibrated with reference to the C–C bond in the C 1s spectrum (284.6 eV). The corresponding XPS results of InP/1ZnO core/shell QDs have been demonstrated in Figure 6.2 (For XPS

results of InP core see Appendix C). It has been observed that In-3d and P-2p peaks (see Figure 6.2a and Figure 6.2b) shifted towards higher binding energies which indicates the additional oxidation layer formation by the presence of ZnO shell on the InP core structure. In addition to this result, Zn-2p and O-1s peaks also confirm the ZnO shell growth (see Figure 6.2c and Figure 6.2d).

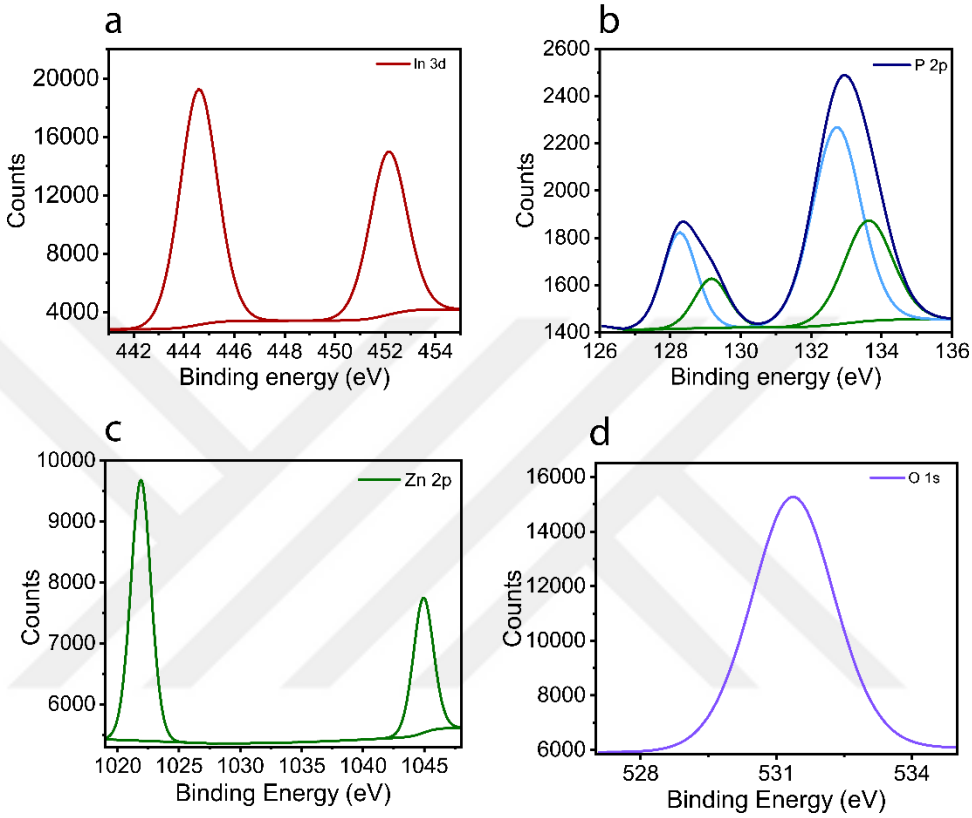

Figure 6. 2: XPS results of InP/1ZnO core/shell QDs. (a) In-3d, (b) P-2p, (c) Zn-2p, and (d) O-1s. For the In-3d spectrum, we obtained two distinct peaks located at 444.59 and 452.15 eV; whereas the P-2p spectrum displayed two doublets located at 128.38 and 132.93 eV, which represent the chemical environment of phosphorus as introduced in previous studies [94].

6.2.2 Optical characterization results of InP/ZnO core/shell QDs

A ligand exchange process was employed after the synthesis of InP/ZnO core/shell QDs to investigate the reactive oxygen species (ROS) generation efficiency. The energy bandgap diagram of InP core and quasi-type-II InP/ZnO core/shell QDs are given in Figure 6.3a. For the ligand exchange, we used short-chain sulfide ligand (S^{-2}) to enhance the charge carrier separation and increase the ROS efficiency. The ligand exchange

process was carried out by mixing the InP/ZnO QDs dissolved in hexane with sodium sulfide nonahydrate ($Na_2S \cdot 9H_2O$) which is dissolved in a high polar solvent N-methyl-formamide (NMF) at room temperature. The final sulfide-capped QDs were dissolved in water. The images of QD solution under ambient and UV light before and after ligand exchange process were shown in Figure 6.3b and Figure 6.3c.

The absorbance and photoluminescence spectra of the InP/ZnO core/shell QDs before and after ligand exchange were investigated (see Figure 6.3d, Figure 6.3e and Appendix C). It has been observed that ZnO shell formation caused red-shift of the emission peak of the InP core from 598 nm to 618 nm (~70 meV) (Figure 6.3e). The red-shift in emission peak indicates that hole is confined in the InP core structure, while the electron delocalizes entire core/shell QDs.

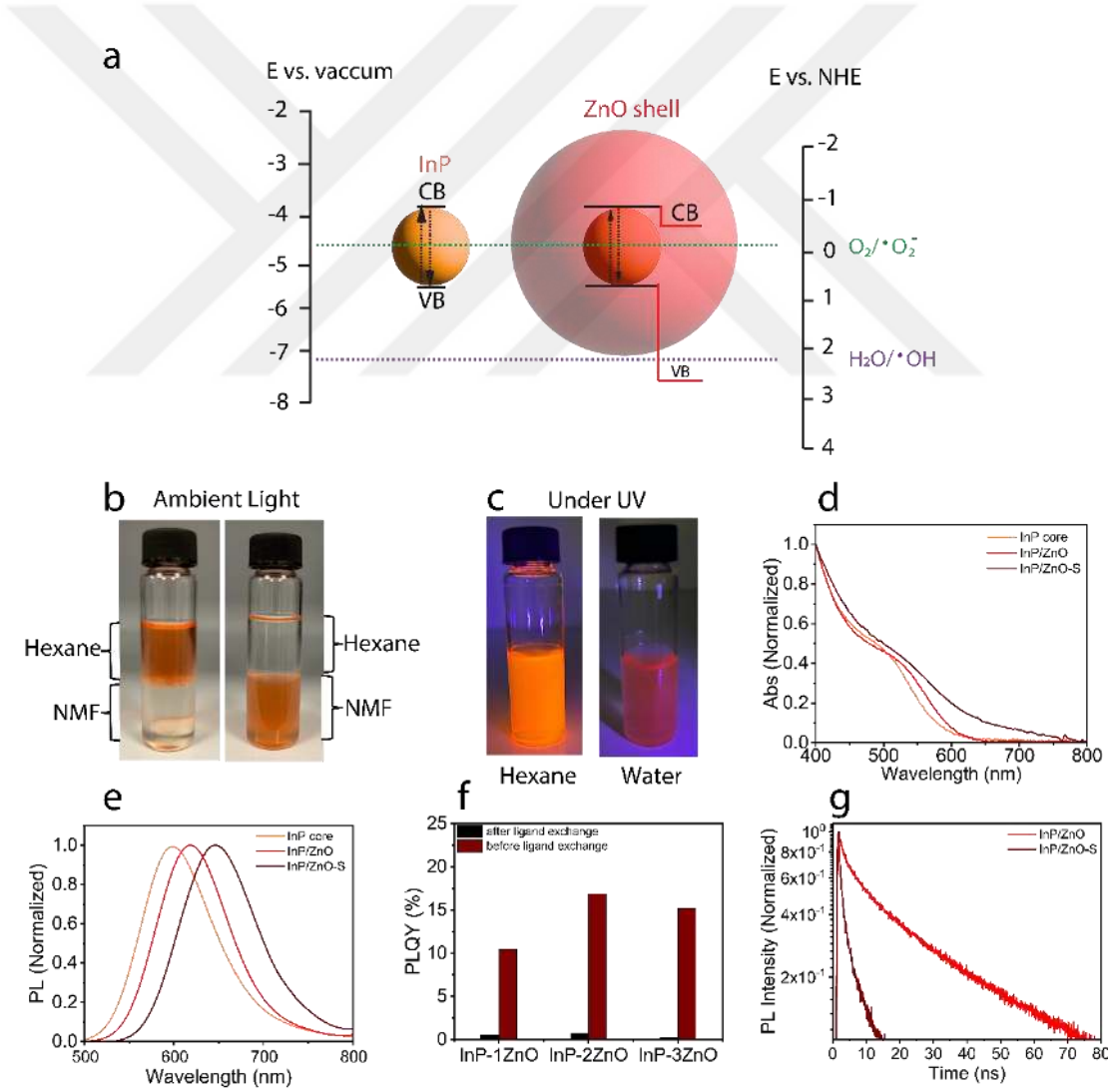

Figure 6. 3: (a) The energy bandgap diagram of InP and InP/1ZnO QDs with redox potentials for the generation of reactive oxygen species. (b) The images of ligand exchange process. Before ligand exchange with sulfide ligand, OLA capped InP/1ZnO QDs are dissolved in hexane. After the ligand exchange process in the presence of NMF and sodium sulfide nonahydrate ($Na_2S{\cdot}9H_2O$) QDs become soluble in water. (c)The images of InP/1ZnO QDs under UV light before and after ligand exchange process. (d) and (e) Abs and PL emission of InP core and InP/1ZnO capped with OLA and sulfide ligand. (f) The bar chart of PLQY values for InP/1ZnO, InP/2ZnO, and InP/3ZnO core/shell QDs capped with OLA and sulfide ligand. After the ligand exchange process, PLQY drastically decreased by the exterior surface trap states which are generated by short-chain sulfide ligand. (g) Recombination decay rate of InP/1ZnO QDs capped with OLA (red colored) and sulfide ligand (brown colored).

We also investigated the shell thickness effect on photoluminescence quantum yield (PLQY) attribute of QDs. We observed that as the shell thickness increases from 1-ZnO to 2-ZnO, PLQY value also increased from 10.5% to 16.9% due to better passivation of surface trap states [48]. However, further increase in ZnO shell thickness (3-ZnO) caused strain effects in the crystal structure, leading to lower PLQY value (Figure 6.3f) [137]. The ligand exchange with short-chain sulfide ligand (S^{-2}) resulted in further red-shift in the emission peak of QDs from 618 nm to 646 nm, possibly as a result of enhanced charge transfer toward sulfide ions (S^{2-}) and further separation of charges as demonstrated in Figure 6.3e [224]. It should be also pointed out that after ligand exchange with sulfide ligand caused decrease in PLQY of QDs due to the formation of increased amount of trap states and nonradiative relaxation processes (Figure 6.3f) [65, 224].

Figure 6.3g demonstrates the recombinaton lifetime of InP/1ZnO QDs before and after ligand exchange process. It was fitted by using a biexponential decay function and the average lifetime of InP/1ZnO core/shell QDs was calculated using Equation (6.1) as follows:

$$\tau_{ave} = \frac{(A_1 \times \tau_1^2 + A_2 \times \tau_2^2)}{(A_1 \times \tau_1 + A_2 x \tau_2)} \tag{6.1}$$

where τ_i respresents the PL-decay time constants; A_i respresents the amplitudes of the corresponding decay components. After ligand exchange with sulfide ligand the

recombination lifetime decreased from 13.9 ns to 3.5 ns, indicating the formation of excess nonraditive trap states by the presence of sulfide [65].

6.3 Reactive Oxygen Species (ROS) studies

For the ROS generation studies of the InP/ZnO QDs with multiple ZnO shells, we used 2′,7′-dichlorofluorescein diacetate (DCFH-DA) as sensor molecule [225]. By the presence of ROS in the medium, this sensor molecule is converted into dichlorofluorescein (DCF) which is a fluorescent molecule that emits at 525 nm (see Appendix C). Therefore, the change in fluorescence intensity of this sensor molecule provides information about the ROS generation in different time intervals. In this regard, after ligand exchange with sulfide, we illuminated the resulting InP/ZnO core/shell QDs with green light with a wavelength of 530 nm and measured the fluorescence intensity of dichlorofluorescein (DCF). We observed that sulfide-capped InP/1ZnO QDs exhibited the highest ROS generation compared to InP/2ZnO and InP/3ZnO QDs (Figure 6.4a). This suggests that with increasing the ZnO shell formation the charge carrier transfer towards sulfide ligand becomes harder.

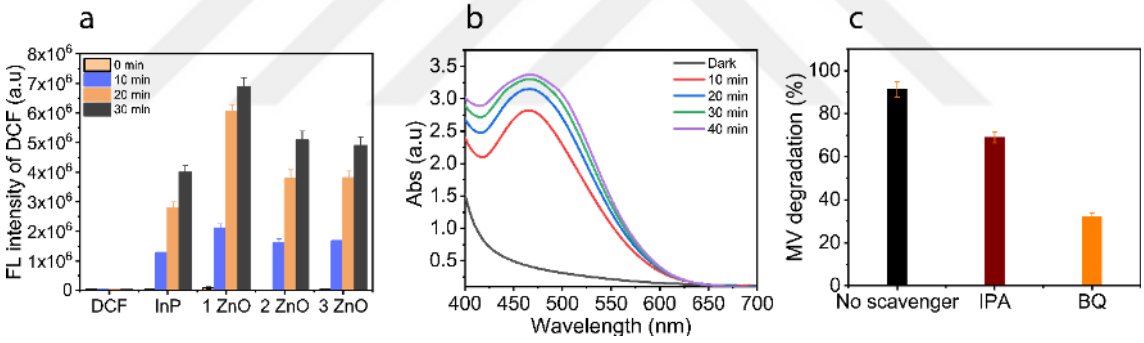

Figure 6. 4: Detection and quantification of Reactive Oxygen Species (ROS) generated by InP/ZnO QDs. For the excitation of QDs, green light with wavelength of 530 nm was used. (a) The effect of ZnO shell number on ROS generation efficiency. During experiment, DCFH-DA sensor molecule is used at a concentration of 10 µM. The highest ROS efficiency was obtained by InP/1ZnO core/shell QDs. (b) The absorbance result of XTT-formazan which is related to generation of superoxide radical ($^{\bullet}O_2^-$). (c) Methyl violet degradation experiment which is based on isopropanol (IPA) and benzoquinone (BQ) as scavengers.

Since all the ROS molecules generated by semiconductor photocatalysis are sensitive to DCFH-DA sensor molecule, it is important to differentiate the types of generated ROS molecules. In this regard, we conducted several experiments. First, we used XTT (sodium 3′-[1-[(phenylamino)carbonyl]-3,4-tetrazolium]-bis(4-methoxy-6-nitro)benzene sulfonic acid hydrate) [226] to detect the superoxide radical ($^{\bullet}O_2^-$) produced by QDs. The presence of the superoxide radical ($^{\bullet}O_2^-$) in the medium enables the transformation of XTT to XTT-formazan [227] which is an orange-colored water-soluble compound that can be detected spectrophotometrically by monitoring the increase in absorbance at 470 nm. Upon green light irradiation for every 10 mins time intervals, we observed that the absorbance intensity of the XTT-formazan increased, which shows the superoxide radical ($^{\bullet}O_2^-$) generation at the concentration of 114 ± 7.34 μM by InP/ZnO QDs (Figure 6.4b). Additionally, we did not observe any absorbance in the absence of light irradiation (Figure 6.4b). Second, we performed an experiment which is based on methyl violet (MV) dye to detect other possible ROS molecules, except superoxide radical ($^{\bullet}O_2^-$). For that, we used isopropanol (IPA) and 1,4-benzoquinone (BQ) as scavengers for hydroxyl ($^{\bullet}OH$) and superoxide radicals ($^{\bullet}O_2^-$), respectively [228]. It was observed that both hydroxyl ($^{\bullet}OH$) and superoxide radicals ($^{\bullet}O_2^-$) are responsible for the photodegradation of MV dye as shown in Figure 6.4c. Moreover, an experiment which is based on InP/ZnS QDs and MV dye as control groups was carried out to confirm the presence of hydroxyl ($^{\bullet}OH$) radical. It was observed that the absorbance of MV did not change substantially after 30 minutes of irradiation which verifies that hydroxyl ($^{\bullet}OH$) radical is generated by the presence of ZnO shell (see Appendix C) [229]. Based on these experiments, photocatalytic mechanism of InP/ZnO QD is as follows: when the QD is excited electron-hole pair is created. Electrons that delocalize entire core/shell InP QD structure interact with oxygen molecule (O_2) to generate superoxide ($^{\bullet}O_2^-$) (Equation 6.2), while holes are captured by sulfide ligand to generate hydroxyl ($^{\bullet}OH$) radicals (Equation 6.3) [65, 230].

$$O_2 + e^- \rightarrow^{\bullet} O_2^- \tag{6.2}$$

$$H_2O + h^+ \rightarrow H^+ + {}^{\bullet}OH \tag{6.3}$$

As a result, it can be referred that quasi-type-II sulfide-capped InP/ZnO core/shell QDs exhibit photocatalytic activity based on the generation of hydroxyl ($^{\bullet}OH$) and superoxide ($^{\bullet}O_2^-$) radicals (see Figure 6.3a).

6.4 Antibacterial studies

For the antibacterial experiments of sulfide capped InP/ZnO QDs, we determined the antibacterial effect against *P. aeruginosa* at different QD concentrations, ranging from 50 to 125 µM under green light exposure (λ_{peak} = 530 nm) at a low intensity level of 3 $mW.cm^{-2}$ (see Figure 6.5). In the dark, InP/ZnO QDs exhibited no growth-inhibiting property, indicating that the concentration of QD is below the inherent toxicity. Despite we observed no growth inhibition at a QD concentration of 50 µM (mean CFU/ml $1.83x10^4$), increasing the concentration of QDs to 75 µM enabled growth inhibition of up to 91.7% under green light exposure. The highest growth inhibitions of 95.5% (mean CFU/ml $1.02x10^2$ & p: 0.0069) and 98.7% (mean CFU/ml $3.90x10^2$ & p: 0.0053) were obtained at QD concentrations of 100 µM and 125 µM, respectively. Additionally, we conducted scanning electron microscopy (SEM) characterization technique to investigate the cellular morphology change (see Figure 6.5). SEM images demonstrated that cellular morphology is not altered in the case of control and QD-treated groups in the dark. However, for the QD-treated groups which were exposed to green light, the cellular morphology changed as shown in the SEM images (marked with red circles-see Figure 6.5e), indicating that sulfide capped InP/ZnO QDs can be activated through externally applied light.

We also performed cytotoxicity assay for the InP/ZnO QDs using Vero E6 cells under in the dark and we observed that the cell viability remained above 90% at QD concentrations ranging from 50 µM to 125 µM (see Figure 6.6). Thus, it can be concluded that InP/ZnO QDs can be considered as an effective biocompatible material for antibacterial applications.

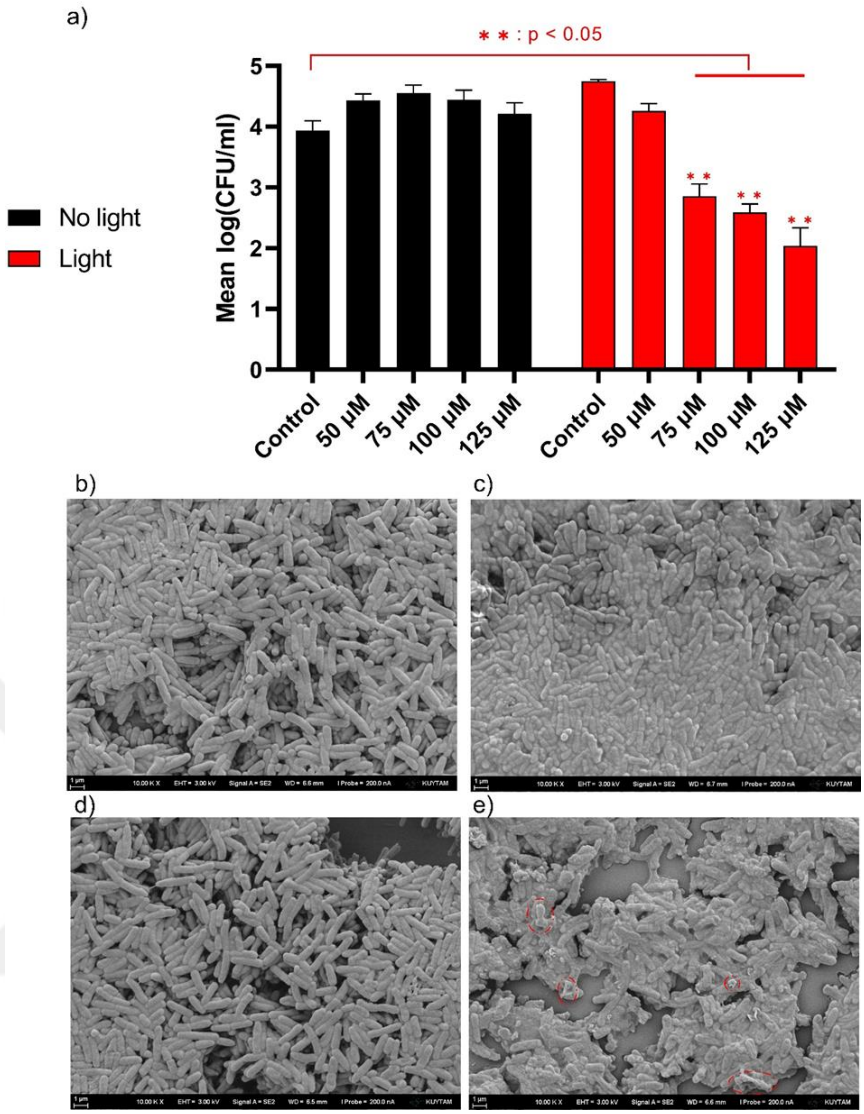

Figure 6. 5: (a) Antibacterial experiments of sulfide capped InP/ZnO QDs against P. aeruginosa at different QD concentrations, ranging from 50 to 125 µM in the dark and under low intensity green light stimulation (3 mW cm^{-2}). (b) SEM image of untreated bacteria. As control group, bacteria were not treated with QD concentration or light exposure. (c) SEM image of bacteria which is incubated with InP/ZnO QDs at a concentration of 125 µM in the dark. (d) SEM image of bacteria exposed to low intensity green light. (e) SEM image of bacteria which is incubated with InP/ZnO QDs at a concentration of 125 µM under low green light exposure.

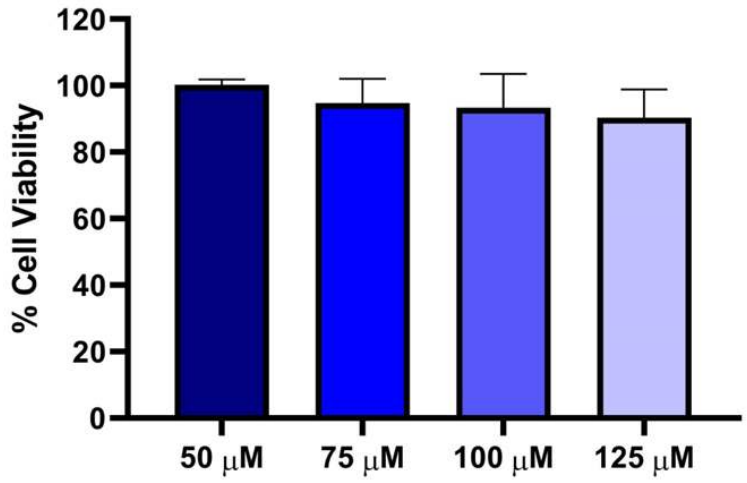

Figure 6. 6: Dark cytotoxicity of sulfide capped InP/ZnO QDs on Vero E6 cells.

6.5 Conclusion

In conclusion, we demonstrated quasi-type-II InP/ZnO core/shell QDs with multiple ZnO shells for antibacterial application against *P. aeruginosa*. In order to separate charge carriers further and enhance the ROS efficiency, amine groups were successfully replaced with short-chain sulfide ligands via ligand exchange process. It has been observed that InP/ZnO QDs have the potential to generate ROS, specifically superoxide ($^{\bullet}O_2^-$) and hydroxyl radicals ($^{\bullet}OH$). Moreover, InP/ZnO QDs with 1-ZnO shell exhibited the highest ROS efficiency compared to 2-ZnO and 3-ZnO shells. Furthermore, upon low intensity green light stimulation (3 $mW.cm^{-2}$) the optimized core/shell QDs displayed high antibacterial activity of 99% inhibition against *Pseudomonas aeruginosa.*

Chapter 7: Conclusion

In conclusion, in this thesis work, we have shown novel InP-based QDs and their light-emitting diode (LED) and antibacterial applications. In this regard, we first introduced highly efficient quasi-type-II InP/ZnO/ZnS core/shell/shell QDs with PLQY of more than 90%. ZnO and ZnS shell formation were confirmed by optical analysis that is supported by quantum mechanical simulations. Further, using small angle X-ray scattering (SAXS) measurement we described that ZnS shell formation enables the transition of the NC ensemble from spherical to elliptical shapes. We also suppressed the host material effect in QD-based light-emitting diodes by simple liquid-state integration that lead to an external quantum efficiency (EQE) of 9.4% and power conversion efficiency (PCE) of 6.8%, respectively. Then, we introduced ruthenium doping which can be an alternative strategy to obtain efficient red-emitters in InP crystal structure for the first time. We confirmed the ruthenium presence inside the InP crystal structure by several characterization techniques such as x-ray photoelectron spectroscopy (XPS), energy-dispersive X-ray analysis (EDX). In order to enhance the PLQY of ruthenium doped InP QDs (Ru:InP) we grew ZnS shell and the final Ru:InP/ZnS QDs exhibited PLQY of 77.6% in the red spectral region. We also observed that in the absence of ruthenium the PLQY of QDs was measured around 60%. The integration of Ru:InP/ZnS QDs into LEDs in a liquid matrix led to an external quantum efficiency of 7.9%.

As the final study of this thesis, for the first time, we demonstrated quasi-type-II InP/ZnO core/shell QDs with multiple ZnO shells as efficient photocatalysts for the generation of reactive oxygen species (ROS). We used hot injection and thermal decomposition methods to synthesize InP/ZnO core/shell QDs. Quasi-type-II heterostructure by ZnO shell led to red-shift in emission peak from 598 nm to 618 nm (~70 meV). We conducted ligand exchange process to replace amine group with short-chain sulfide ligand. InP/ZnO QDs with 1-ZnO shell exhibited the highest ROS efficiency compared to 2-ZnO and 3-ZnO shells. Furthermore, upon low intensity green light stimulation (3 $mW.cm^{-2}$) the optimized core/shell QDs exhibited high antibacterial activity of 99% inhibition against *Pseudomonas aeruginosa.*

As a result of our studies, I published 4 articles as first-author in such journals including *ACS Applied Materials & Interfaces*, *ACS Applied Nano Materials*, *AIP Chemical*

Physics Reviews, and STAR Protocols, and co-authored eight more journal papers published in *ACS Nano, Nano Letters, ACS Photonics, Scientific Reports, Advanced Healthcare Materials, Advanced Materials Technologies, and Frontiers in Neuroscience.*

Appendix A

A.1 Synthesis of InP/ZnO/ZnS core/shell/shell QDs

A.1.1 Synthesis of InP QDs

Firstly, 43 mg of zinc undecylenate, 32 µL oleic acid (OA), 66 µL oleylamine (OAM), 22 mg $InCl_3$ were mixed in 3 mL ODE and heated to 120° C. The flask was degassed 20 min at 120° C and refilled with nitrogen. Afterwards it was heated to 200° C and 500 µL phosphine stock solution ($P(TMS)_3$-ODE 0.2 mmol mL^{-1}) was rapidly injected and mixed 30 min at 200° C. Then the solution was cooled down to 80° C and aliquot was taken from sample.

A.1.2 Synthesis of InP/ZnO and QD-4ZnS core/shell/shell NCs

In order to prepare the ZnO stock solution 245 µL OAM, 8 µL OA and 6,5 mg $Zn(acac)_2$ were mixed in 1.6 mL ODE at 80° C. 500 µL ZnO stock solution was added to InP core solution at 80° C and heated to 250° C. It was mixed 30 min at this temperature and cooled to 170° C. For the zinc (Zn) and sulphur (S) precursor solutions were prepared separately. 510 mg $Zn(St)_2$ and 27 mg S powder were dissolved in 8 mL ODE and 8 mL TOP, respectively. It should be noted that for fully dissolving of sulphur in TOP we applied heat which was around 100°C. After preparation of stock solutions, they were added to InP/ZnO solution in a row and heated to 250° C. The solution was mixed at 250° C for 30 min. For each shelling procedure same method was employed. The injection amounts of precursors were shown in Table A.2.

A.2 InP/ZnO/ZnS-based QD-LEDs

A.2.1 Lens making procedure

In order to make hemi-spherical lens with outer diameter of 9 nm and inner diameter of 7 nm, PDMS-SYLGARD 184 Elastomer was mixed with of SYLGARD 184 curing agent with ratio of 10:1, then the mixture was stirred vigorously until the bubbles appear. Afterwards to dispel the bubbles completely the mixture was degassed 20 min. The mixture was poured into the aluminum mold and cured at 70° C 1 hour. After curing, lens was taken out from mold. The thickness of the as-prepared lens is 1 mm.

A.2.2 Fabrication of LED Device and Close-Packed LEDs

Before soldering of the electrical wires for connection to the voltage supply, the blue chip was mounted on board. Afterward, PDMS lens was attached on LEDs by using an NOA 68 UV curable polymer. To cure LEDs with PDMS lens were kept under UV radiation at 365 nm for 20 min. To prevent any leakage from PDMS lens, dripping of curable polymer and keeping under radiation was made two times.

A.2.3 LED measurements

For LED measurement, an EP-B4040F-A3 InGaN GaN blue LED chip from Secol Company with an illumination wavelength at 465 nm was used. LED measurements were performed with a multi-port Ocean Optics integrating sphere. The detector was an Ocean Optics Torus with optical resolution of 1.6 nm FWHM. The signal to noise ratio was 250:1. The external quantum efficiency was calculated based on literature as mentioned above.

A.3 Structural and optical characterizations of QDs

Powder X-ray diffraction (XRD) measurements of the InP, InP/ZnO, and QD-4ZnS NCs were performed by Bruker D8 eco X-ray diffractometer [$\lambda_{Cu\text{-}K\alpha}$=1.54 Å radiation] with a scan speed of 0.14° min^{-1}. Before XRD measurements, they were purified three times to remove excess impurities. Then, the colloidal NC dispersion was drop casted on a Si-miscut wafer, a zero-background holder. XRD measurement was carried out at room temperature. Steady-state absorbance and PL measurements were performed by using Edinburgh Instruments FL-50 spectrofluorometer by excitation wavelength of 375 nm. QE measurements were carried out by using an integrating sphere with an inner diameter of 150 mm.

For TEM measurement, samples were deposited as 10 µL of 1 mM of QD in hexane solution on a copper support grid. Transmission electron microscopy (TEM) analysis was performed using a JEOL JEM-ARM200CFEG UHR microscope with a spherical aberration-corrected probe and equipped with a Gatan UltraScan camera model 994 US1000X.

Bright-field images were collected using an accelerating voltage of 200 keV. For the small angle x-ray scattering (SAXS) measurements about 100 µl of NC-dispersions have

been filled in quartz glass capillaries with 1.5 mm diameter and have been sealed with epoxy resin. The capillaries have been inserted into our laboratory SAXS system (*Nanostar* from Bruker AXS) and have been measured in vacuum to suppress air scattering. Two-dimensional (2D) SAXS images have been recorded using Cu-K_α X-ray radiation with a wavelength of 1.5 Å and a 2D Vantec detector. The 2D scattering patterns have been azimuthal integrated to obtain 1D scattering intensity *I(q)* data as a function of the reciprocal scattering vector *q*. All 1D data have been corrected for the different x-ray transmission values.

Transient absorption (TA) studies were performed with an ultrafast pump-probe spectrometer to measure the change ΔA in the nonlinear absorbance spectrum ($\Delta A = A_{pumped} - A_{unpumped}$; A_{pumped}=absorbance spectrum of the pumped sample and $A_{unpumped}$=small-signal absorbance spectrum). Further details of the pump-probe setup and measurement procedure are described in reference [34].Here, free charge carriers were excited with a 320-nm femtosecond pump pulse (fluence of 480 μJ.cm^{-2}) and the resulting nonlinear absorbance change was measured with a femtosecond white-light probe in the 450-800 nm spectral window.

Table A. 1: PLQY values according to injected ZnO precursor amount into InP Core solution.

	ZnO precursor solution injection amount	Zn/In ratio (mmol)	PLQY of InP/ZnO Core/shell QDs (%)
Concentration-1	300 μL	0.38 x 10^{-2}	14.6
Concentration-2	400 μL	0.51 x 10^{-2}	22.4
Concentration-3	500 μL	0.65 x 10^{-2}	25.8
Concentration-4	600 μL	0.77 x 10^{-2}	22

Table A. 2: Zinc and Sulphur precursor solution concentration for ZnS shells.

	Concentration (M)	QD-1ZnS	QD-2ZnS	QD-3ZnS	QD-4ZnS	QD-5ZnS	QD-6ZnS
$ZnSt_2$-ODE	0.1	600 µL	825 µL	1050 µL	1365 µL	1775 µL	2310 µL
S-TOP	0.1	600 µL	825 µL	1050 µL	1365 µL	1775 µL	2310 µL

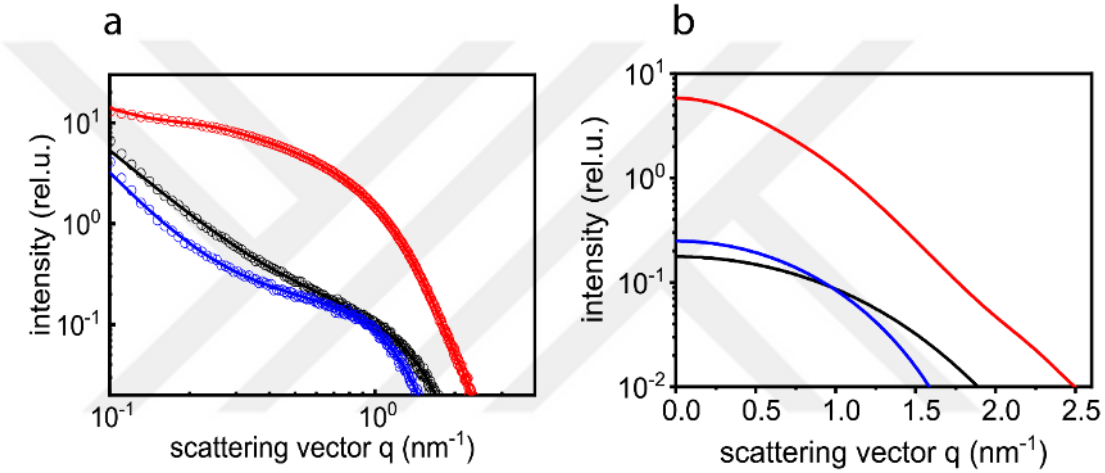

Figure A. 1: SAXS data (symbols) and fits of InP core, InP/ZnO and QD-4ZnS. In (a) the experimental SAXS data together with resulting fits (lines) are shown. For describing the partly aggregated NCs we fitted simultaneously the structure factor S(q) and the form factor P(q). (b) Here the resulting form factor alone is shown containing information on particle size, shape, and size distribution.

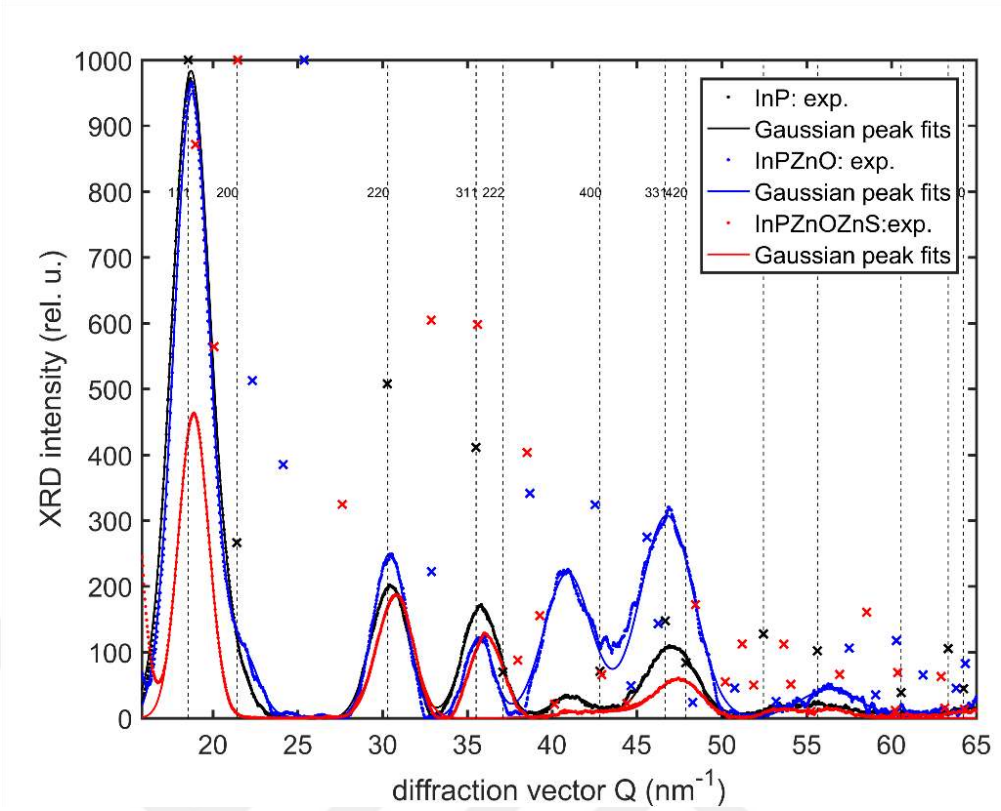

Figure A. 2: X-ray diffraction (XRD) of InP (black), InP/ZnO (blue) and of InP/ZnO/ZnS (QD-4ZnS) core/shell/shell QDs. The lines are Gaussian peak fits on a splined background to the XRD data (dots). The black vertical dashed lines and black crosses marks the positions of InP (ICDD 00-032-0452), the blue crosses of hexagonal ZnO (ICDD 00-036-1451) and the red crosses of hexagonal wurtzite ZnS (ICDD 00-036-1450) in its relaxed bulk crystal phases.

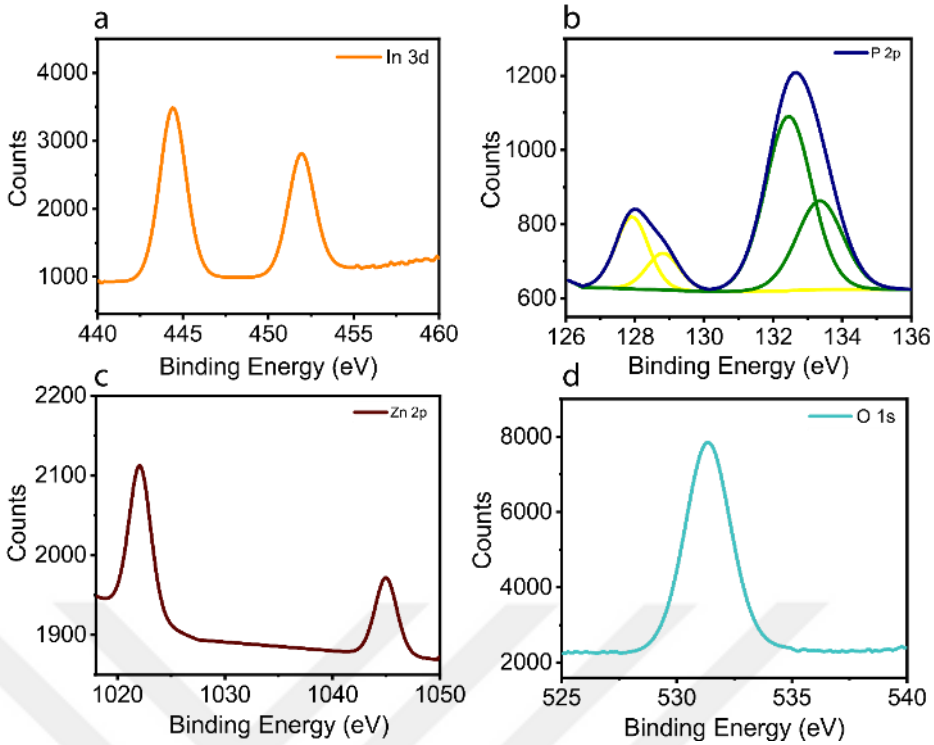

Figure A. 3: X-ray photoelectron spectroscopy analysis of InP/ZnO core/shell QDs. a) In 3d spectrum, b) P 2p spectrum, (c) Zn 2p spectrum, and (d) O 1s spectrum.

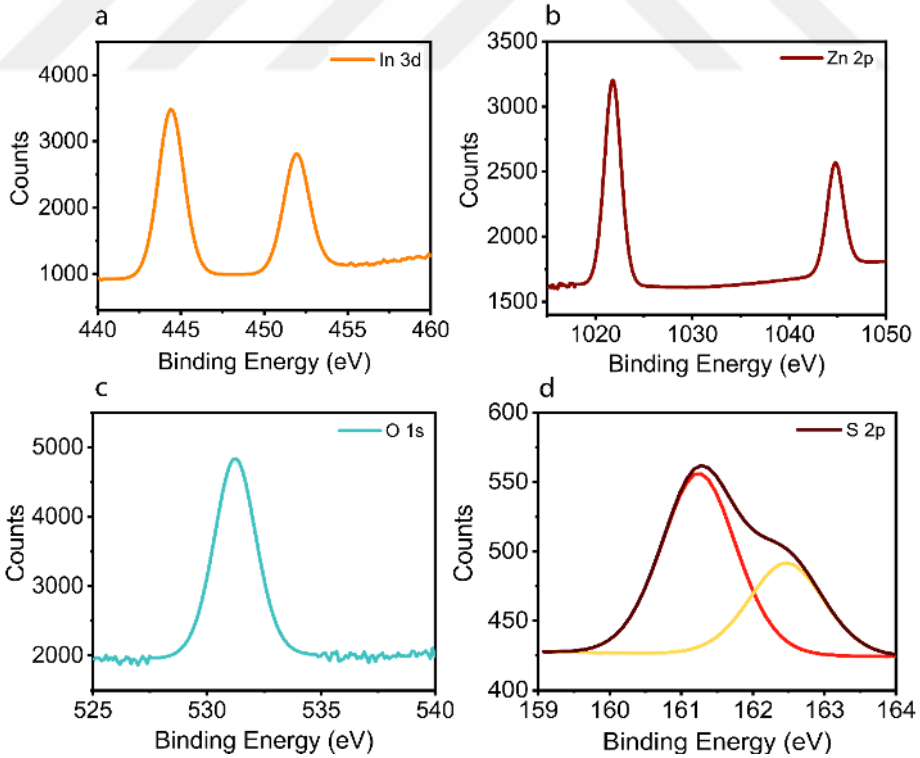

Figure A. 4: X-ray photoelectron spectroscopy analysis of QD-4ZnS core/shell/shell QDs. a) In 3d spectrum, b) Zn 2p spectrum, (c) O 1s spectrum, and (d) S 2p spectrum.

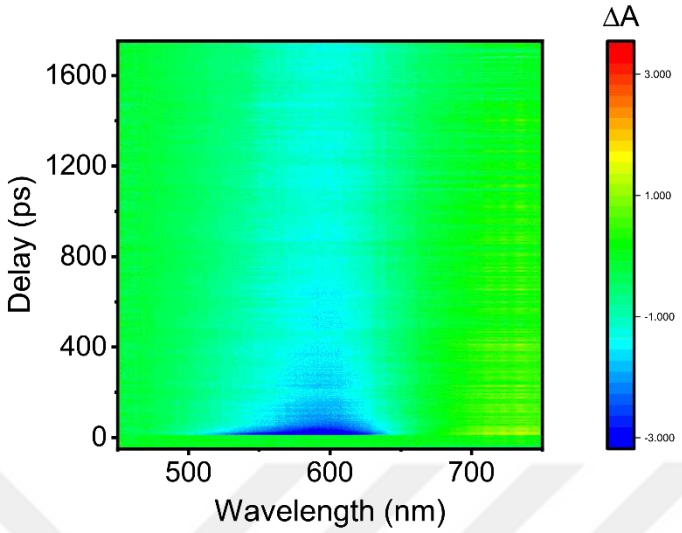

Figure A. 5: Surface plot of the measured ΔA with respect to the probe wavelength and delay up to 1.7 ns for the QD-4ZnS NCs.

Appendix B

B.1 Synthesis of Ru:InP/ZnS QDs

B.1.1 Zinc oleate (0.5 M) stock solution preparation

5504 mg zinc acetate (30 mmol), 20 mL OAm, and 40 mL ODE were mixed at room temperature and degassed at 120º C for 60 min. After degassing, the temperature increased to 170º C under argon atmosphere and mixed at 170º C for 30 min. It was cooled down to room temperature and centrifuged at 9000 rpm, 6 min using hexane. Centrifugation process was repeated 3 times. The resulting white powder was kept in glove-box.

B.1.2 Ruthenium (0.01 M) stock solution preparation

4 mg $Ru(acac)_3$ was dissolved in 1 mL anhydrous chloroform.

B.1.3 Synthesis of InP Core QDs with different core sizes

For the synthesis of green-emitting InP core QDs, 22 mg (0.1 mmol) $InCl_3$, 48 mg (0.2 mmol) HDA, 43 mg (0.1 mmol) zinc undecylenate and 28 mg (0.1 mmol) SA were mixed in 3 ml ODE in a three-neck 50 ml round bottom reaction flask. The solution was firstly degassed at 120 °C for 1.5 h, then heated up to 220º C under nitrogen atmosphere. 0.5 ml of the $P(TMS)_3$ stock solution was injected into the solution at this temperature. The solution was kept at 210º C for 20 min and then cooled down to room temperature. For the synthesis of yellow and orange-emitting InP core structure, same chemical amounts were used. Injection temperature for yellow and orange-emitting InP QDs were 230º C and 235º C, respectively. After injection of phosphine precursor, they were mixed at 220 and 225º C for 20 min, respectively. After 20 min, they were cooled down to room temperature. Then, the solutions were centrifuged at 9000 rpm, 20 min using hexane-ethanol. Centrifugation process was repeated 2 times. The final QD solutions were redispersed in hexane.

B.1.4 Synthesis of Ru:InP QDs

After 20 min, instead of cooling down to room temperature, solutions were cooled down to 150º C. At 150º C, Ru precursor solution with different Ru:In ratio was injected into the main solution and the reaction flask was heated to 230º C. After injection of ruthenium

precursor, the solution color became darker. It was mixed at 230° C for 20 min, cooled down to room temperature. Then, the solution was centrifuged at 9000 rpm, 20 min using hexane-ethanol. Centrifugation process was repeated 2 times. The final QD solution was redispersed in hexane.

B.1.5 Synthesis of Ru:InP/ZnS core/shell QDs

Instead of cooling down to room temperature, Ru:InP solution was cooled down to 160° C. 259 mg zinc oleate and 93 mg sulfur were dissolved in 2 mL TOP. Solution temperature increased to 220° C and zinc precursor solution was injected dropwise into the flask at a rate of 2 mL/h using a syringe pump. Then, the solution was kept at 220° C for 60 min for growing the shell. Finally, the solution was cooled down to room temperature. Afterwards, hexane was added into the flask and the resulting crude solution was centrifuged at 11000 rpm, 3 min. Centrifugation at 11000 rpm was repeated 3 times to minimize the amount of zinc-based organic parts. Then, the QD solution was mixed hexane and ethanol with a volume ratio of 1:2:4 and precipitated at 9000 rpm for 10 min. Precipitation process was repeated 2 times. The final QDs solution was redispersed in toluene.

B.2 Ru:InP/ZnS-based QD-LED

B.2.1 Lens making procedure

In order to make hemi-spherical lens with outer diameter of 9 mm and inner diameter of 7 mm, PDMS-SYLGARD 184 Elastomer was mixed with of SYLGARD 184 curing agent with ratio of 10:1, then the mixture was stirred vigorously until the bubbles appear. Afterwards to dispel the bubbles completely the mixture was degassed 20 min. The mixture was poured into the aluminum mold and cured at 70° C for 1 hour. After curing, the lens was taken out from mold. The thickness of the as-prepared lens is 1 mm.

B.2.2 Fabrication of LED Device

Before soldering of the electrical wires for connection to the voltage supply, the blue chip was mounted on board. Afterward, PDMS lens was attached to LEDs by using an NOA 68 UV curable polymer. To cure LEDs with PDMS lens were kept under UV radiation at 365 nm for 20 min. To prevent any leakage from PDMS lens, dripping of curable polymer and keeping under radiation were made two times.

B.2.3 LED Measurements

Ocean Optics integrating spheres were used for LED characterizations. An Ocean Optics Torus was used as a detector with a wavelength range of 300 to 900 nm with an optical resolution of 1.6 nm FWHM over the spectra range. An Ocean Insight HL-3P-INT-CAL was used as a calibration source.

B.3 Structural and Optical Characterizations of QDs

X-ray diffraction (XRD) of InP core, Ru:InP, and Ru:InP/ZnS QDs were carried out using a Rigaku Miniflex XRD $\lambda_{Cu\ K\alpha}$ = 1.54 Å with a 5° min^{-1} scan rate. XRD samples were prepared by drop-casting QDs dissolved in hexane onto 1 cm × 1 cm silicon wafers and heated to 100° C and kept at this temperature for 1 h to dry liquid QDs on the silicon wafers. XRD measurements were carried out at room temperature. The lattice parameters of the samples were determined by least-squares refinement on 3 reflection positions corresponding to (111), (220) and (311) planes, using WinCSD software package [231]. For the X-ray photoelectron spectroscopy (XPS) measurement, the same sample preparation method was followed. XPS measurements were performed using a Thermo Scientific K-α (Al Kα source) surface analysis tool at ultrahigh vacuum conditions. For the analysis, binding energies in the XPS data were calibrated with reference to the C–C bond in the C 1s spectrum (284.6 eV). ICP-MS measurement was performed to investigate the chemical composition of the QDs. For the ICP-MS analysis, Agilent 7700x inductively coupled plasma-mass spectrometer was used. The powder samples were digested in 10 mL of aqua regia (8 mL HNO_3 + 2 mL HCl) via a Start D Milestone Microwave Digestion system and obtained each samples diluted with a deionized water (18.2 Mohm) by a ratio of 1:3. For TEM measurement, samples were deposited as 10 μL of a 1 mM QD in a hexane solution on a copper support grid. TEM measurements were performed using Hitachi HT7800 (100 kV). HRTEM measurements were performed using FEI TALOS F200S TEM 200 kV. STEM images were collected using Hitachi HF5000 Cs corrected cold FEG 200 kV, equipped with EDX (Oxford Instruments).

Steady-state absorbance and PL measurements were performed using an Edinburgh Instruments, FS5 spectrofluorometer with a 150 W xenon lamp. The excitation wavelength was 375 nm. For absorbance and PL measurements, regular quartz cuvettes were used. PLQY measurements were carried out using an integrating sphere with an

inner diameter of 150 mm. For the femtosecond transient absorption spectroscopy (TAS) experiments, solutions containing QDs were excited with 320-nm femtosecond pulses, generated with an optical parametric amplifier (MKS Spectra-Physics TOPAS) which was pumped with a regeneratively amplified Ti:sapphire laser delivering 120-fs pulses (MKS Spectra-Physics, Spitfire Ace). The incident pump fluence was 480 μJ/cm^2. The resulting difference ΔA between the pumped and unpumped absorbance was measured as a function of probe delay by utilizing a femtosecond white-light probe in the 400−650 nm spectral window.

Table B. 1: ICP-MS analysis results for the Ru:InP core QDs.

Sample Amount (mg)	**In (wt%)**	**Ru (wt%)**	**P (wt%)**
56.4	0.36	0.005	0.071

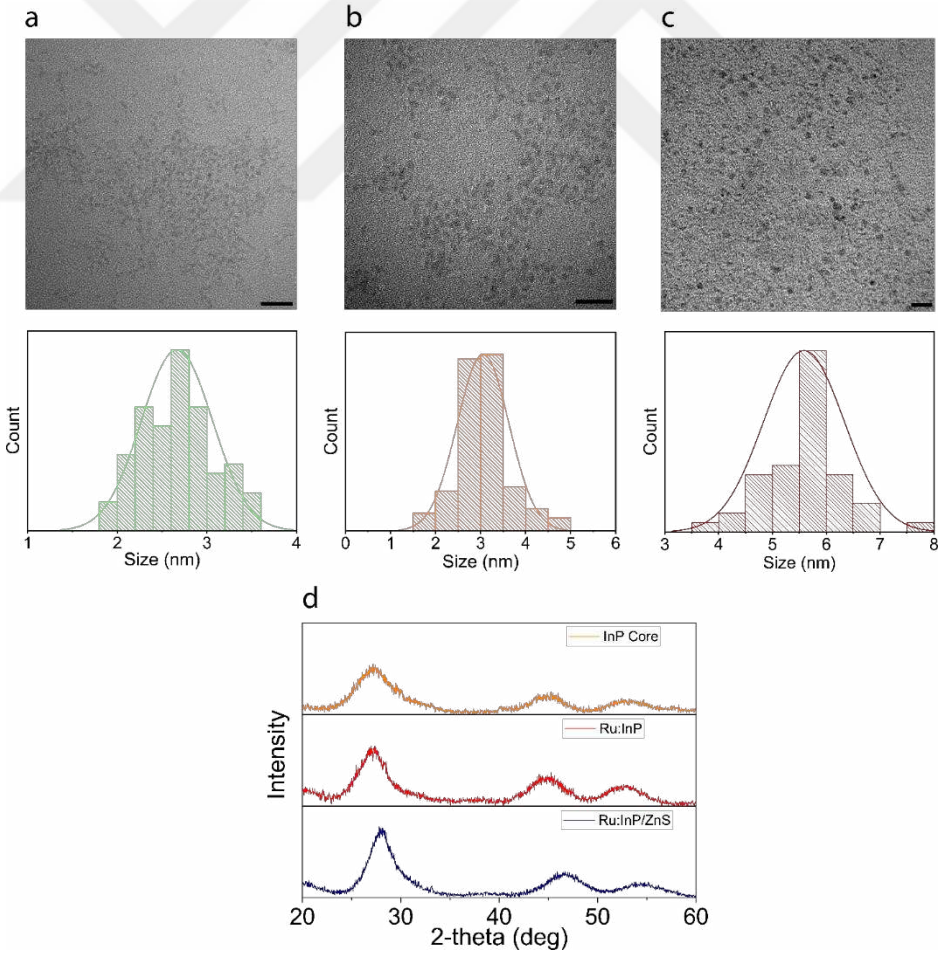

Figure B. 1: TEM and size distribution of the synthesized (a) G-InP core (2.67 nm ± 0.39), (b) Ru:InP (3.05 nm ± 0.57) (Ru:In ratio of 0.005), and (c) Ru:InP/ZnS core/shell QDs (5.58 nm ± 0.74). For the particle size distribution, a minimum of 200 particles were counted. The scale bar of the TEM images is 20 nm. (d) XRD pattern for the InP core, Ru:InP and Ru:InP/ZnS core/shell QDs. The XRD pattern for InP core QDs exhibited three well-defined peaks observed at 2θ values of 27.18°, 44.95°, and 52.97°, attributing to the (111), (220), and (311) planes of the zinc-blende crystal structure of InP (JCPDS32-0452). After the Ru incorporation (Ru:In ratio of 0.005), the diffraction peaks shifted to lower 2θ values of 27.10°, 44.77°, and 52.66° that indicate lattice filling of Ru dopant at the interstitial sites of the InP host structure. After the ZnS shell growth on the Ru-doped InP QDs, the diffraction peaks shifted toward higher 2θ values of 28.00°, 46.66°, and 54.46°, respectively.

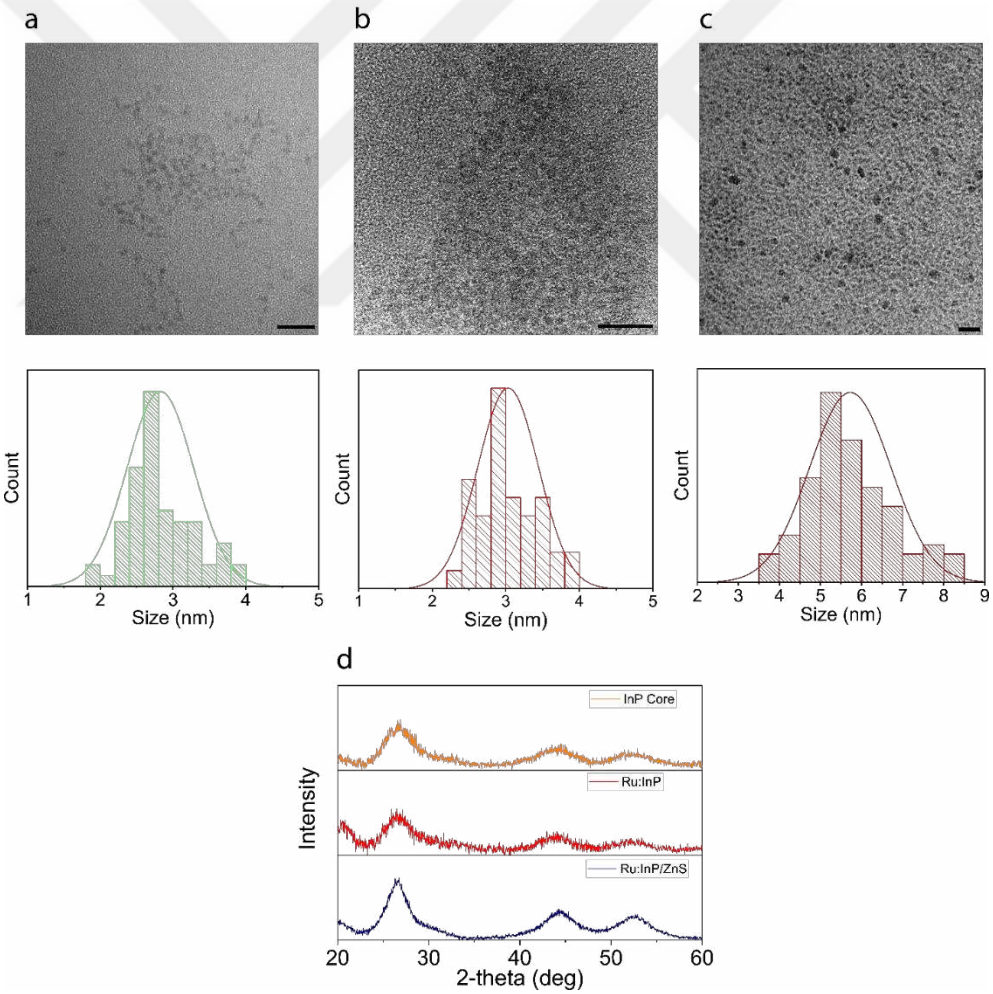

Figure B. 2: TEM and size distribution of the synthesized (a) G-InP core (2.81 nm ± 0.47), (b) Ru:InP (3.03 nm ± 0.40) (Ru:In ratio of 0.01), and (c) Ru:InP/ZnS core/shell QDs

(5.71 nm ± 0.98). For the particle size distribution, a minimum of 200 particles were counted. The scale bar of the TEM images is 20 nm. (d) XRD pattern for the InP core, Ru:InP and Ru:InP/ZnS core/shell QDs. The XRD pattern for InP core QDs exhibited three peaks observed at 2θ values of 26.65°, 44.14°, and 52.11°, attributing to the (111), (220), and (311) planes of the zinc-blende crystal structure of InP (JCPDS32-0452). After the Ru incorporation (Ru:In ratio of 0.01), the diffraction peaks shifted to lower 2θ values of 26.55°, 44.00°, and 52.07° that indicate lattice filling of Ru dopant at the interstitial sites of the InP host structure. After the ZnS shell growth on the Ru-doped InP QDs, the diffraction peaks shifted toward higher 2θ values of 26.60°, 44.41°, and 52.56°, respectively.

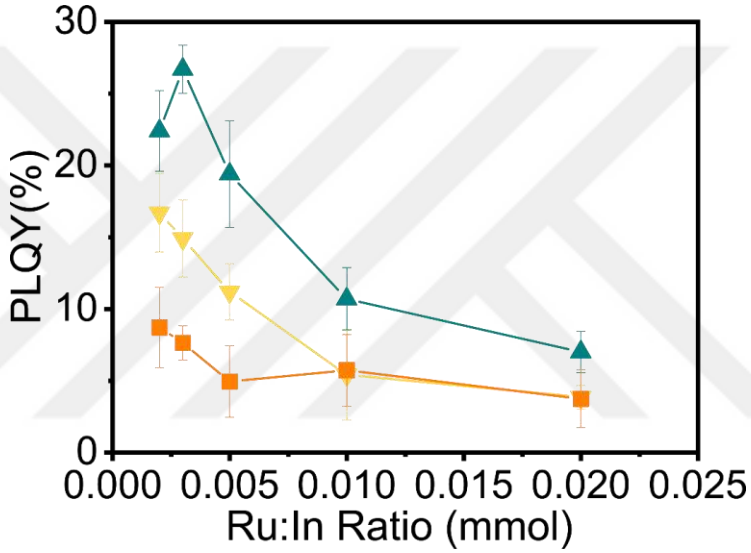

Figure B. 3: The effect of Ru doping on PLQY for the InP core QDs emitting at green, yellow, and orange spectral range.

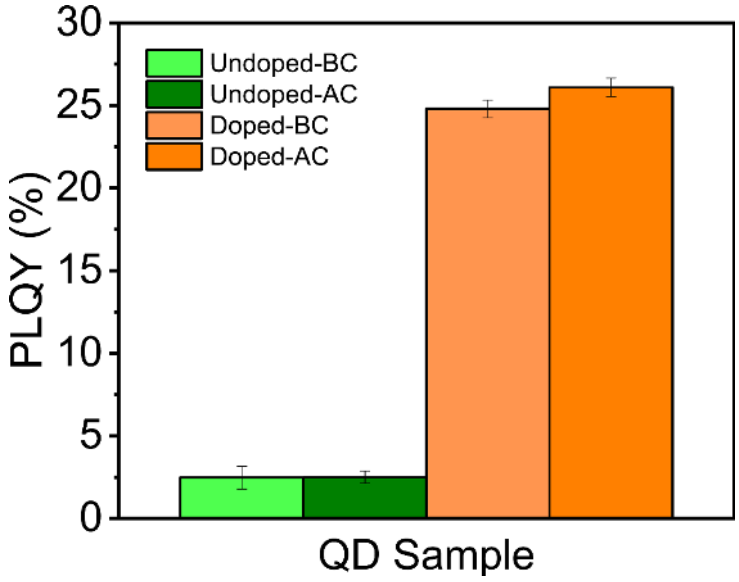

Figure B. 4: PLQY (%) change of undoped and doped QDs before centrifugation (BC) and after centrifugation (AC) process.

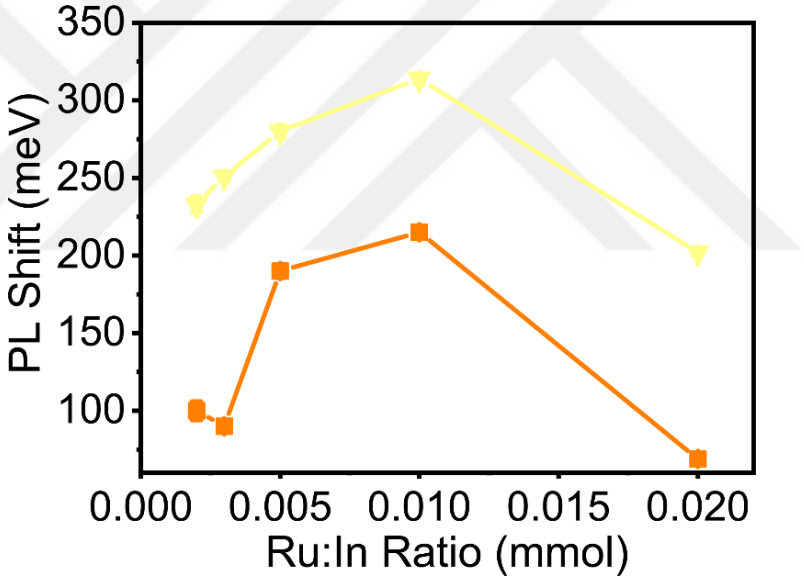

Figure B. 5: PL shift (meV) for Y-InP and O-InP core QDs according to different Ru:In injection ratio.

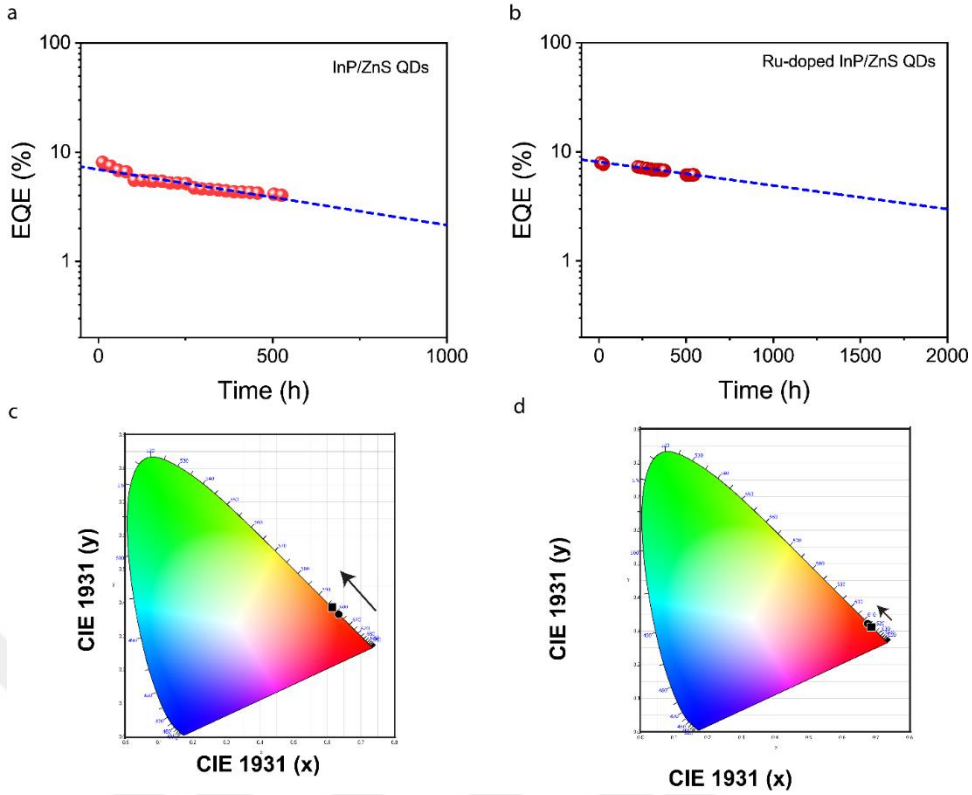

Figure B. 6: EQE of LEDs integrated with (a) InP/ZnS QDs and (b) Ru-doped InP/ZnS at 10 mA for 500 h. The CIE color coordinate changes of (c) bare InP/ZnS QDs and (d) Ru-doped InP/ZnS QDs.

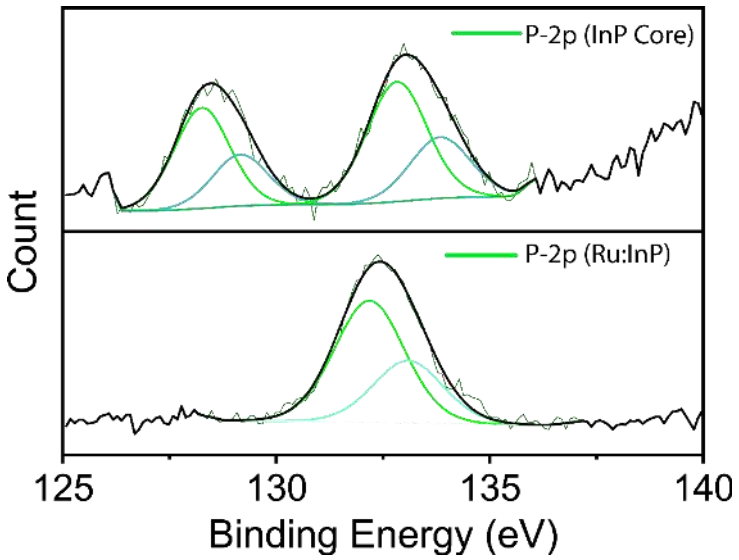

Figure B. 7: P-2p spectrum of the InP core and Ru:InP QDs.

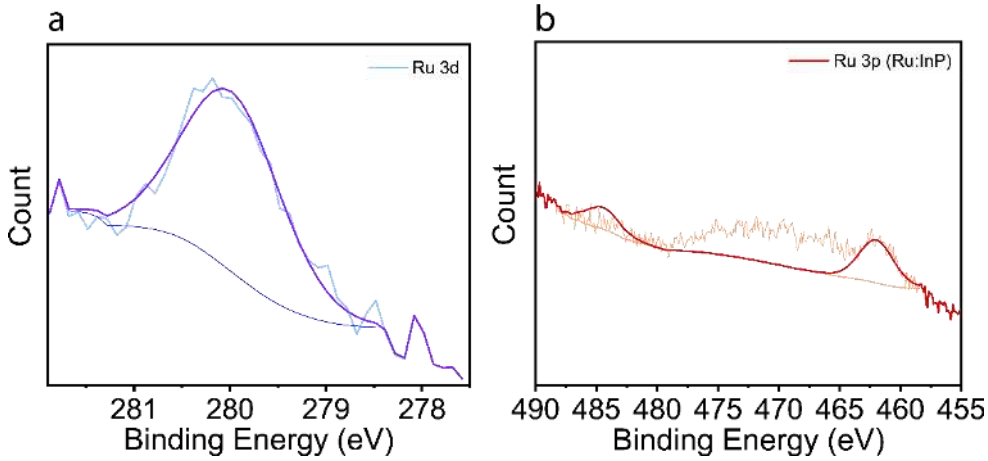

Figure B. 8: (a) Ru-3d and (b) Ru-3p spectrum of the Ru:InP QDs.

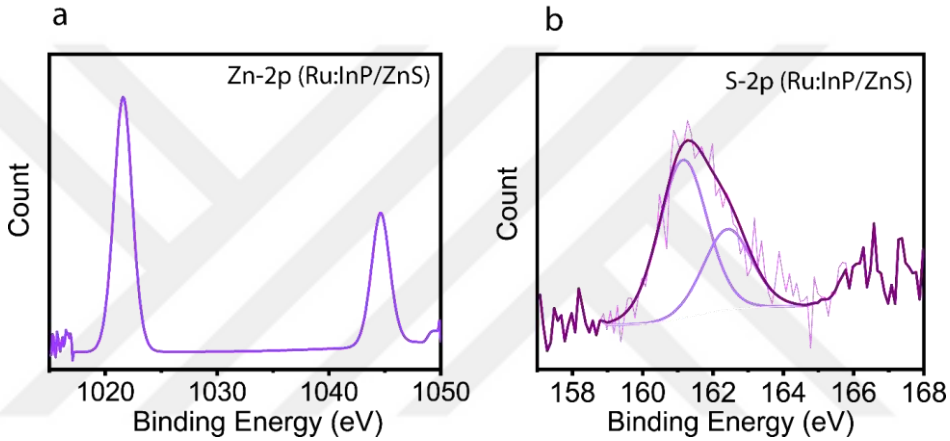

Figure B. 9: (a) Zn-2p spectrum, and (b) S-2p spectrum of Ru:InP/ZnS core/shell QD.

The EQE of the LEDs was measured from the following formula (Equation B.1) [209]

$$\eta_{ext} = \frac{\text{number of photons emitted into free space per second}}{\text{number of electrons injected into LED per second}} = \frac{P/(h\nu)}{I/e} \qquad \text{(B.1)}$$

where P is the optical power emitted into free space, also called radiant flux.

Appendix C

C.1 Synthesis of InP/ZnO core/shell QDs

C.1.1 Synthesis of InP core QDs

For InP core QD synthesis, zinc undecylenate (43 mg), oleic acid (OA) (32 µL), and oleylamine (OLA) (66 µL) were mixed with indium chloride ($InCl_3$) (22 mg) in ODE (3 mL) medium. Afterwards, it was degassed at 120° C for 1.5 hour and temperature is increased to 220° C under argon (Ar) environment. 500 µL phosphine solution [$P(TMS)_3$-ODE] (0.1 $mmol.ml^{-1}$) was rapidly injected into the main solution at 220° C and mixed at that temperature for 30 min. The solution was then cooled to 80° C, and an aliquot was taken for characterization purposes.

C.1.2 Synthesis of InP/ZnO core/shell QDs

In order to synthesize InP/ZnO core/shell QDs zinc acetylacetonate dehydrate [$Zn(acac)_2.xH_2O$] solution (6.5 mg) which includes oleylamine (OAM-245 µL), oleic acid (OA-8 µL) and 1.6 mL ODE was injected at 80° C and heated to 245° C. It was mixed at 245° C for 30 min, then it was cooled down to room temperature. For additional ZnO shell growth, same procedure was performed. The crude solution was cooled down to room temperature. Hexane was added into the flask and the resulting crude solution was centrifuged at 11000 rpm for 3 min to remove byproducts. The QD solution was mixed with hexane and ethanol. Then, it was centrifuged at 9000 rpm for 10 min. Precipitation process was repeated two times. The final QDs solution was redispersed in hexane.

C.2 Ligand exchange of InP/ZnO core/shell QDs

Ligand exchange process was carried out using $Na_2S{\cdot}9H_2O$ as sulfide source. InP/ZnO QDs which are dissolved in hexane with the concentration of 3-5 mg/mL were mixed with 0.05 M $Na_2S{\cdot}9H_2O$ solution dissolved in N-methyl-formamide (NMF) at room temperature. Once the transfer of QDs towards N-methyl-formamide (NMF) solution is completed, NMF solution was centrifuged using hexane to remove the remaining nonpolar organic species. Then, QDs were precipitated using acetone. Afterwards, QD precipitate was redissolved in water by ultrasonication process. Once a clear solution was obtained, centrifugation process was performed at 5000 rpm for 5 min to remove the impurities. The final QDs dissolved in water were stored at 2-6° C.

C.3 Optical and structural characterization

To determine the surface composition of the QDs, X-ray photoelectron spectroscopy (XPS) was employed, using a Thermo Scientific K-alpha (Al Kα source) surface analysis tool at ultrahigh vacuum conditions. XPS spectrometer with binding energy calibrated using the C 1s peak at 284.5 eV. For powder X-ray diffraction (XRD) analysis, a Rigaku miniflex XRD instrument with $\lambda_{Cu\ K\alpha}$ = 1.54° A and a scan rate of 5 min^{-1} was utilized. To prepare the samples for XPS and XRD analysis, the QDs were dissolved in hexane and deposited onto a 1 cm x 1 cm silicon wafer. The samples were then completely dried by heating to 110° C for 1 hour. TEM measurements were performed using FEI TALOS F200S TEM 200 kV. For TEM analysis, samples were deposited as 10 µL of a 1 mM QD in a hexane solution on a copper support grid.

Steady-state absorbance and photoluminescence measurements were taken using an Edinburgh Instruments (FS5 spectrofluorometer) with an excitation wavelength of 375 nm. Quantum efficiency was measured using an integrating sphere with an inner diameter of 150 mm. For the time-dependent PL decay measurements, a PicoQuant MicroTime 100 time resolved confocal fluorescence microscope with a diode laser (λexc = 375 nm) at a 60 MHz repetition rate coupled to a 40x objective lens was used. Bandpass filters with a bandwidth of 15 nm were utilized for spectrally resolved data.

C.4 ROS detection and quantification

For the ROS detection and quantification experiements, 2',7'-dichlorofluorescein diacetate (DCF-DA) was used as a sensor molecule at a concentration of 10 µM. A stock solution of 2',7'-dichlorofluorescein diacetate (DCF-DA) (10 mM) was prepared using dimethyl sulfoxide (DMSO) solvent, then it was diluted to 10 µM solution. QD solution and blank sample was irridiated by green light. The emission of the DCF molecule was monitored at 0, 10, 20, and 30 minutes. For the emission measurement, Edinburgh Instruments FS5 spectrofluorometer was used. During the measurements the excitation wavelength was adjusted to 490 nm. To quantify superoxide ($^{\bullet}O_2^-$) radical, sodium 3′-[1-[(phenylamino)-carbony]-3,4-tetrazolium]-bis(4-methoxy-6-nitro) benzene-sulfonic acid hydrate (XTT) was used. For the absorbance measurement of XTT-formazan Edinburgh Instruments FS5 spectrofluorometer was used. The molar concentration of each ROS species was determined using Equation C.1

$$C = \frac{\int_0^T C_0 - C_t dt}{T} \quad (C.1)$$

where C is the average molar concentration of ROS species, C_o is the initial concentration of the sensor molecule, C_t is the concentration of the sensor molecule at time t, T is the irradiation time.

Methyl violet (MV) dye degradation experiment was performed using isopropanol (IPA) and 1,4-benzoquinone (BQ) as scavengers for hydroxyl ($^{\bullet}OH$), superoxide anion ($^{\bullet}O_2^-$). Beer-Lambert law was used to calculate the concentration of MV dye.

C.5 Antibacterial study

The antibacterial activity of InP/ZnO QDs at different concentrations ranging from 50 to 125 µM was evaluated against *Pseudomonas aeruginosa* ATCC® 700829™ strain. To perform the assay, overnight bacterial cultures were diluted in 1 x PBS (Biowest) to obtain a final concentration of 105 CFU/ml. The diluted cultures were then incubated with the QDs for 1 hour at 37° C in 12-well Ibidi chambers, whereas control group was incubated with phosphate buffered saline (PBS) only. Green light source (λ_{max} = 530 nm) was utilized to excite the samples for 4 hours. To evaluate the antibacterial effect of QDs in the dark, a separate set of samples was prepared without light exposure. For control group, no QD treatment or light exposure was performed. For the quantification of the viable bacteria, serial diluted samples were prepared and plated on agar plates. The experiments were repeated three times.

For the bacteria-counting assay, bacteria suspensions (concentration of 10^6 per well) are first incubated with QDs for one hour, followed by green light exposure for four hours. Then, bacterial suspensions were centrifuged and the pellets were washed. The pellets were then stained with BacLight (L7007, Invitrogen) for 15 minutes at room temperature and fixated with 3.5% formaldehyde for 1 hour. The washed pellets were transferred to black flat bottom 96-well plates (Greiner), and the total cell counts were analyzed using the Celigo Image Cytometer.

Following the exposure to green light, the bacterial pellets were washed with 1x PBS and fixated in 2.5% glutaraldehyde for 1 hour. Then, the samples were dehydrated by incubating them in 50, 70, 80, 90, and 100% of ethanol for 10 min and they were transferred onto glass slides (10 µl of sample for each). Scanning electron microscope

(SEM) was used for the high-resolution image. Before SEM characterization, the samples were coated with gold to obtain clear image. The magnification was 10,000x.

For the cytotoxicity studies of the QDs, Vero-E6 cell lines were grown in high-glucose DMEM supplemented with 10% inactivated Fetal Bovine Serum and 1% Penicillin/Streptomycin/Amphotericin at 37° C under 5% CO_2. InP/ZnO QDs added to the Vero-E6 cell lines at concentrations of 50, 75, 100, and 125 µM. Afterwards, they were incubated for 5 hours at 37° C. Following the incubation process, the cells were treated with 0.5 mg/ml MTT for 2 hours at 37° C. Then, 200 µl of DMSO was added to the cells, and the absorbance was measured at 570 nm using a Multiskan GO plate reader.

C.6 Statistical analysis

Viable bacterial counts were compared with One-Way ANOVA test using Graphpad Prism 9. Inhibition caused by QD and / or light exposure were compared to control viable counts. The bacterial inhibition was considered as statistically significant for $p < 0.05$.

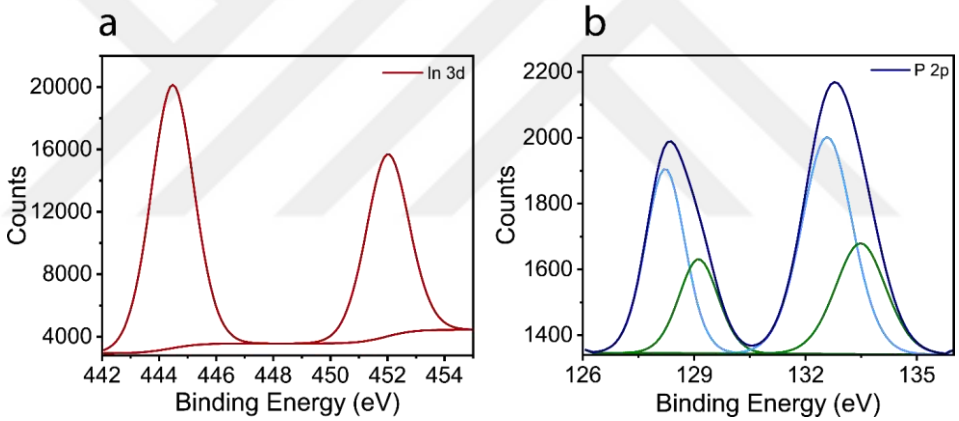

Figure C. 1: (a) In-3d and (b) P-2p spectrum of InP core QD.

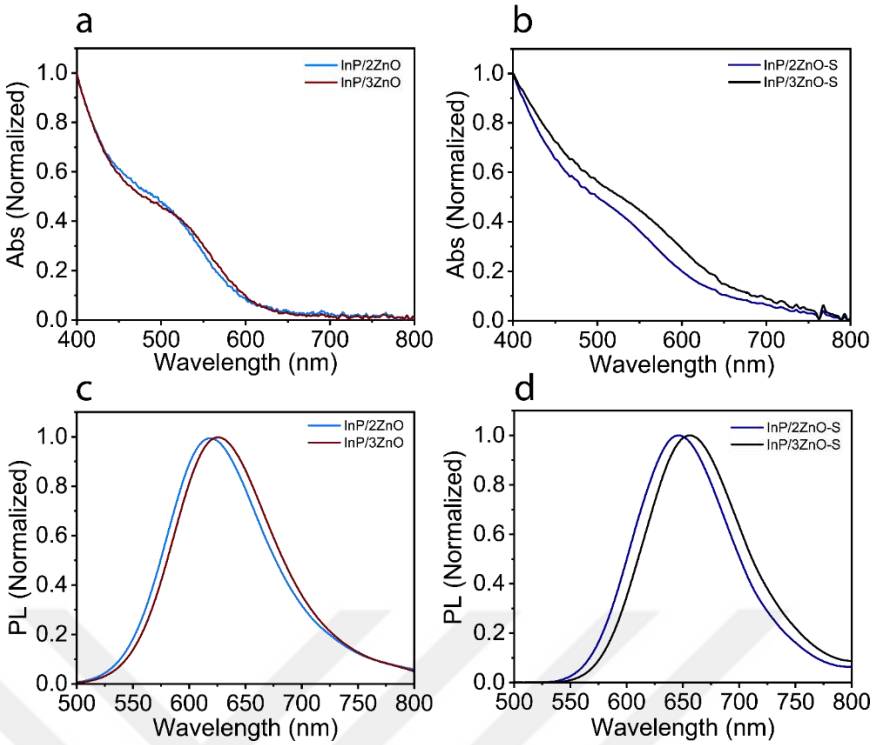

Figure C. 2: Photophysical properties of 2 and 3 ZnO shell grown on the top of InP core QDs (a) and (b) Abs spectra for before and after sulfide ligand exchange, respectively. (c) and (d) show PL spectra before and after sulfide ligand exchange, respectively.

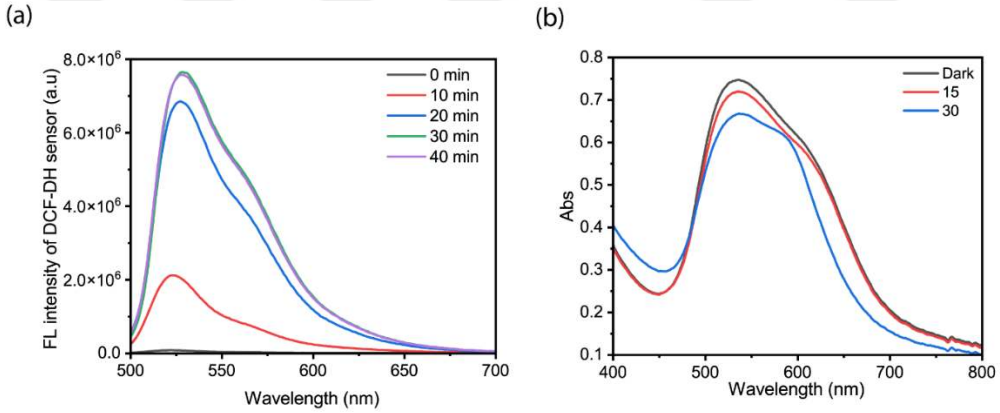

Figure C. 3: (a) DCF-DH spectrum in the presence of InP/ZnO QDs. For the experiment, DCF-DH (10 µM) sensor molecule and 0.5 mM InP/ZnO QDs was utilized under green light stimulation. (b) shows the absorbance spectrum of MV dye in the presence of InP/ZnS QDs under green light stimulation.

Appendix D

D.1 List of Publications

D.1.1 First-author publications in peer reviewed journals

Eren, G. O.; Onal, A.; Karatum, O.; Jahangiri, H.; Ozer, M. S.; Eroglu, Z.; Sundu, B.; Kaya, L.; Burcak, A. B.; Aydemir, U.; Metin, O.; Sennaroglu, A.; Nizamoglu, S; "Ruthenium-Doped InP Quantum Dots for Efficient Red Emission", *ACS Applied Nano Materials*, vol. 6, no. 12, pp. 10044-10053, 2023.

Sadeghi, S.*, **Eren, G. O.***, & Nizamoglu, S., "Strategies for improving performance, lifetime, and stability in light-emitting diodes using liquid medium", *Chemical Physics Reviews*, vol. 2, no. 4, 2021 (* equal contribution).

Eren, G. O.; Sadeghi, S.; Shahzad, M.; Nizamoglu, S., "Protocol on synthesis and characterization of copper-doped InP/ZnSe quantum dots as ecofriendly luminescent solar concentrators with high performance and large area", *STAR protocols*, vol. 2, no. 3, pp. 100664, 2021.

Eren, G. O., Sadeghi, S., Bahmani Jalali, H., Ritter, M., Han, M., Baylam, I., ... & Nizamoglu, S., "Cadmium-free and efficient type-II InP/ZnO/ZnS quantum dots and their application for LEDs", *ACS Applied Materials & Interfaces*, vol. 13, no. 27, pp. 32022-32030, 2021.

D.1.2 Co-author publications in peer reviewed journals

Onal, A., **Eren, G. O.**, Melikov, R., Kaya, L., & Nizamoglu, S., "Quantum Dot Enabled Efficient White LEDs for Wide Color Gamut Displays", *Advanced Materials Technologies*, vol. 8, no. 9, pp. 2201799, 2023.

Onal, A., Sadeghi, S., Melikov, R., Karatum, O., **Eren, G. O.**, & Nizamoglu, S., "Quantum Dot to Nanorod Transition for Efficient White-Light-Emitting Diodes with Suppressed Absorption Losses", *ACS Photonics*, vol. 9, no. 10, pp. 3268-3278, 2022.

Karatum, O., Kaleli, H. N., **Eren, G. O.**, Sahin, A., & Nizamoglu, S., "Electrical stimulation of neurons with quantum dots via near-infrared light", *ACS Nano*, vol. 16, no. 5, pp. 8233-8243, 2022.

Onal, A., **Eren, G. O.**, Sadeghi, S., Melikov, R., Han, M., Karatum, O., ... & Nizamoglu, S., "High-performance white light-emitting diodes over 150 lm/W using near-unity-emitting quantum dots in a liquid matrix", *ACS Photonics*, vol. 9, no. 4, pp. 1304-1314, 2022.

Han, M., Yildiz, E., Kaleli, H. N., Karaz, S., **Eren, G. O.**, Dogru-Yuksel, I. B., ... & Nizamoglu, S., "Tissue-like optoelectronic neural interface enabled by PEDOT: PSS hydrogel for cardiac and neural stimulation", *Advanced Healthcare Materials*, vol. 11, no. 8, pp. 2102160, 2022.

Karatum, O., Aria, M. M., **Eren, G. O.**, Yildiz, E., Melikov, R., Srivastava, S. B., ... & Nizamoglu, S., "Nanoengineering InP quantum dot-based photoactive biointerfaces for optical control of neurons", *Frontiers in Neuroscience*, vol. 15, pp. 652608, 2021.

Karatum, O., **Eren, G. O.**, Melikov, R., Onal, A., Ow-Yang, C. W., Sahin, M., & Nizamoglu, S., "Quantum dot and electron acceptor nano-heterojunction for photo-induced capacitive charge-transfer", *Scientific reports*, vol. 11, no. 1, pp. 2460, 2021.

Bahmani Jalali, H., Karatum, O., Melikov, R., Dikbas, U. M., Sadeghi, S., Yildiz, E., Dogru, I. B., **Eren, G. O.**, …& Nizamoglu, S., "Biocompatible quantum funnels for neural photostimulation", *Nano letters*, vol. 19, no. 9, pp. 5975-5981, 2019.

BIBLIOGRAPHY

[1] S. Pimputkar, J. S. Speck, S. P. DenBaars, and S. Nakamura, "Prospects for LED lighting," *Nature photonics,* vol. 3, no. 4, pp. 180-182, 2009.

[2] W. D. Van Driel, B. Jacobs, P. Watte, and X. Zhao, "Reliability of LED-based systems," *Microelectronics Reliability,* vol. 129, p. 114477, 2022.

[3] T. Erdem and H. V. Demir, *Color Science and Photometry for Lighting with LEDs and Semiconductor Nanocrystals*. Springer, 2019.

[4] B. Jia *et al.*, "Nanophysical antimicrobial strategies: a rational deployment of nanomaterials and physical stimulations in combating bacterial infections," *Advanced Science,* vol. 9, no. 10, p. 2105252, 2022.

[5] R. A. Fisher, B. Gollan, and S. Helaine, "Persistent bacterial infections and persister cells," *Nature Reviews Microbiology,* vol. 15, no. 8, pp. 453-464, 2017.

[6] M. Leeb, "Antibiotics: a shot in the arm," *Nature,* vol. 431, no. 7011, pp. 892-894, 2004.

[7] W. H. Organization, "Interagency Coordination Group on Antimicrobial Resistance," *No time to wait: securing the future from drug-resistant infections, Report to the secretary-general of the united nations,* vol. 1, p. 28, 2019.

[8] B. Turner, "Tackling antimicrobial resistance and climate change," *The Lancet,* vol. 392, no. 10163, pp. 2435-2436, 2018.

[9] L. Tan *et al.*, "In situ disinfection through photoinspired radical oxygen species storage and thermal-triggered release from black phosphorous with strengthened chemical stability," *Small,* vol. 14, no. 9, p. 1703197, 2018.

[10] W. H. Organization, "Prioritization of pathogens to guide discovery, research and development of new antibiotics for drug-resistant bacterial infections, including tuberculosis," World Health Organization, 9240026436, 2017.

[11] P. Ganguly, C. Byrne, A. Breen, and S. C. Pillai, "Antimicrobial activity of photocatalysts: Fundamentals, mechanisms, kinetics and recent advances," *Applied Catalysis B: Environmental,* vol. 225, pp. 51-75, 2018.

[12] H. Wang *et al.*, "Semiconductor heterojunction photocatalysts: design, construction, and photocatalytic performances," *Chemical Society Reviews,* vol. 43, no. 15, pp. 5234-5244, 2014.

[13] Y.-H. Won *et al.*, "Highly efficient and stable InP/ZnSe/ZnS quantum dot light-emitting diodes," *Nature,* vol. 575, no. 7784, pp. 634-638, 2019.

[14] B. Karadza *et al.*, "Bridging the Green Gap: Monochromatic InP-Based Quantum-Dot-on-Chip LEDs with over 50% Color Conversion Efficiency," *Nano Letters,* 2023.

[15] M. Levy, J. R. Bertram, K. A. Eller, A. Chatterjee, and P. Nagpal, "Near-infrared-light-triggered antimicrobial indium phosphide quantum dots," *Angewandte Chemie,* vol. 131, no. 33, pp. 11536-11540, 2019.

[16] C. R. McCollum, J. R. Bertram, P. Nagpal, and A. Chatterjee, "Photoactivated Indium Phosphide Quantum Dots Treat Multidrug-Resistant Bacterial Abscesses In Vivo," *ACS Applied Materials & Interfaces,* vol. 13, no. 26, pp. 30404-30419, 2021.

[17] C. M. Tyrakowski *et al.*, "Bright type II quantum dots," *Chemistry of Materials,* vol. 27, no. 21, pp. 7276-7281, 2015.

[18] Q. Lin *et al.*, "High-efficiency deep-red quantum-dot light-emitting diodes with type-II CdSe/CdTe core/shell quantum dots as emissive layers," *Journal of Materials Chemistry C,* vol. 4, no. 30, pp. 7223-7229, 2016.

[19] R. Xie and X. Peng, "Synthesis of Cu-doped InP nanocrystals (d-dots) with ZnSe diffusion barrier as efficient and color-tunable NIR emitters," *Journal of the American Chemical Society,* vol. 131, no. 30, pp. 10645-10651, 2009.

[20] W. Yang *et al.*, "Controllable synthesis of dual emissive Ag: InP/ZnS quantum dots with high fluorescence quantum yield," *Applied Surface Science,* vol. 423, pp. 686-694, 2017.

[21] O. Karatum, E. Yildiz, H. N. Kaleli, A. Sahin, B. Ulgut, and S. Nizamoglu, "RuO2 Supercapacitor Enabled Flexible, Safe, and Efficient Optoelectronic Neural Interface," *Advanced Functional Materials,* p. 2109365, 2022.

[22] A. R. Fatkulin, O. I. Afanasyev, A. A. Tsygankov, and D. Chusov, "Enhancing the efficiency of the ruthenium catalysts in the reductive amination without an external hydrogen source," *Journal of Catalysis,* vol. 405, pp. 404-409, 2022.

[23] C. M. Courtney, S. M. Goodman, J. A. McDaniel, N. E. Madinger, A. Chatterjee, and P. Nagpal, "Photoexcited quantum dots for killing multidrug-resistant bacteria," *Nature materials,* vol. 15, no. 5, pp. 529-534, 2016.

[24] S. Wen *et al.*, "Mechanism insight into rapid photodriven sterilization based on silver bismuth sulfide quantum dots," *ACS Applied Materials & Interfaces,* vol. 13, no. 18, pp. 21979-21993, 2021.

[25] V. Reshma and P. Mohanan, "Quantum dots: Applications and safety consequences," *Journal of Luminescence,* vol. 205, pp. 287-298, 2019.

[26] D. Zherebetskyy *et al.*, "Hydroxylation of the surface of PbS nanocrystals passivated with oleic acid," *Science,* vol. 344, no. 6190, pp. 1380-1384, 2014.

[27] F. W. Eagle, R. A. Rivera-Maldonado, and B. M. Cossairt, "Surface chemistry of metal phosphide nanocrystals," *Annual Review of Materials Research,* vol. 51, pp. 541-564, 2021.

[28] B. Chen, D. Li, and F. Wang, "InP quantum dots: synthesis and lighting applications," *Small,* vol. 16, no. 32, p. 2002454, 2020.

[29] J. Van Embden, A. S. Chesman, and J. J. Jasieniak, "The heat-up synthesis of colloidal nanocrystals," *Chemistry of Materials,* vol. 27, no. 7, pp. 2246-2285, 2015.

[30] Y. Zhou, H. Zhao, D. Ma, and F. Rosei, "Harnessing the properties of colloidal quantum dots in luminescent solar concentrators," *Chemical Society Reviews,* vol. 47, no. 15, pp. 5866-5890, 2018.

[31] E. Groeneveld *et al.*, "Tailoring ZnSe–CdSe colloidal quantum dots via cation exchange: from core/shell to alloy nanocrystals," *ACS nano,* vol. 7, no. 9, pp. 7913-7930, 2013.

[32] Z. Zhang *et al.*, "Dual emissive Cu: InP/ZnS/InP/ZnS nanocrystals: single-source “greener” emitters with flexibly tunable emission from visible to near-infrared and their application in white light-emitting diodes," *Chemistry of Materials,* vol. 27, no. 4, pp. 1405-1411, 2015.

[33] J.-H. Kim, B.-Y. Kim, and H. Yang, "Synthesis of Mn-doped CuGaS 2 quantum dots and their application as single downconverters for high-color rendering solid-state lighting devices," *Optical Materials Express,* vol. 8, no. 2, pp. 221-230, 2018.

[34] S. Sadeghi *et al.*, "High-performance, large-area, and ecofriendly luminescent solar concentrators using copper-doped InP quantum dots," *Iscience,* vol. 23, no. 7, p. 101272, 2020.

[35] C. S. Erickson, L. R. Bradshaw, S. McDowall, J. D. Gilbertson, D. R. Gamelin, and D. L. Patrick, "Zero-reabsorption doped-nanocrystal luminescent solar concentrators," *ACS nano,* vol. 8, no. 4, pp. 3461-3467, 2014.

[36] R. Buonsanti and D. J. Milliron, "Chemistry of doped colloidal nanocrystals," *Chemistry of Materials,* vol. 25, no. 8, pp. 1305-1317, 2013.

[37] N. Pradhan, D. Goorskey, J. Thessing, and X. Peng, "An alternative of CdSe nanocrystal emitters: pure and tunable impurity emissions in ZnSe nanocrystals," *Journal of the American Chemical Society,* vol. 127, no. 50, pp. 17586-17587, 2005.

[38] M. Makkar and R. Viswanatha, "Frontier challenges in doping quantum dots: synthesis and characterization," *RSC advances,* vol. 8, no. 39, pp. 22103-22112, 2018.

[39] P. V. Radovanovic and D. R. Gamelin, "Electronic absorption spectroscopy of cobalt ions in diluted magnetic semiconductor quantum dots: demonstration of an isocrystalline core/shell synthetic method," *Journal of the American Chemical Society,* vol. 123, no. 49, pp. 12207-12214, 2001.

[40] A. Saha, A. Shetty, A. Pavan, S. Chattopadhyay, T. Shibata, and R. Viswanatha, "Uniform doping in quantum-dots-based dilute magnetic semiconductor," *The Journal of Physical Chemistry Letters,* vol. 7, no. 13, pp. 2420-2428, 2016.

[41] D. Chen, R. Viswanatha, G. L. Ong, R. Xie, M. Balasubramaninan, and X. Peng, "Temperature dependence of “elementary processes” in doping semiconductor nanocrystals," *Journal of the American Chemical Society,* vol. 131, no. 26, pp. 9333-9339, 2009.

[42] C. J. Barrows, P. Chakraborty, L. M. Kornowske, and D. R. Gamelin, "Tuning Equilibrium Compositions in Colloidal Cd1–x Mn x Se Nanocrystals Using Diffusion Doping and Cation Exchange," *ACS nano,* vol. 10, no. 1, pp. 910-918, 2016.

[43] C. Pu, H. Qin, Y. Gao, J. Zhou, P. Wang, and X. Peng, "Synthetic control of exciton behavior in colloidal quantum dots," *Journal of the American Chemical Society,* vol. 139, no. 9, pp. 3302-3311, 2017.

[44] A. Onal *et al.*, "High-Performance White Light-Emitting Diodes over 150 lm/W Using Near-Unity-Emitting Quantum Dots in a Liquid Matrix," *ACS Photonics,* vol. 9, no. 4, pp. 1304-1314, 2022.

[45] R. Berera, R. van Grondelle, and J. T. Kennis, "Ultrafast transient absorption spectroscopy: principles and application to photosynthetic systems," *Photosynthesis research,* vol. 101, pp. 105-118, 2009.

[46] F. Meinardi *et al.*, "Large-area luminescent solar concentrators based on ‘Stokes-shift-engineered’nanocrystals in a mass-polymerized PMMA matrix," *Nature Photonics,* vol. 8, no. 5, pp. 392-399, 2014.

[47] Y. Zhou *et al.*, "Near infrared, highly efficient luminescent solar concentrators," *Advanced Energy Materials,* vol. 6, no. 11, p. 1501913, 2016.

[48] S. Sadeghi *et al.*, "Stokes-shift-engineered indium phosphide quantum dots for efficient luminescent solar concentrators," *ACS applied materials & interfaces,* vol. 10, no. 15, pp. 12975-12982, 2018.

[49] K. Wu, H. Li, and V. I. Klimov, "Tandem luminescent solar concentrators based on engineered quantum dots," *Nature Photonics,* vol. 12, no. 2, pp. 105-110, 2018.

[50] B. B. Srivastava, S. Jana, and N. Pradhan, "Doping Cu in semiconductor nanocrystals: some old and some new physical insights," *Journal of the American Chemical Society,* vol. 133, no. 4, pp. 1007-1015, 2011.

[51] H. Wang *et al.*, "ZnSe/ZnS Core–Shell Quantum Dots Doped with Mn2+ Ions for Magnetic State-Manipulated Light Sources," *ACS Applied Nano Materials,* 2022.

[52] A. R. AbouElhamd, K. A. Al-Sallal, and A. Hassan, "Review of core/shell quantum dots technology integrated into building's glazing," *Energies,* vol. 12, no. 6, p. 1058, 2019.

[53] G. S. Selopal, H. Zhao, Z. M. Wang, and F. Rosei, "Core/shell quantum dots solar cells," *Advanced Functional Materials,* vol. 30, no. 13, p. 1908762, 2020.

[54] D. Zhu *et al.*, "ZnCl2 Mediated Synthesis of InAs Nanocrystals with Aminoarsine," *Journal of the American Chemical Society,* vol. 144, no. 23, pp. 10515-10523, 2022.

[55] N. Holonyak Jr and S. F. Bevacqua, "Coherent (visible) light emission from Ga (As1− x P x) junctions," *Applied Physics Letters,* vol. 1, no. 4, pp. 82-83, 1962.

[56] S. Nakamura, T. Mukai, and M. Senoh, "Candela-class high-brightness InGaN/AlGaN double-heterostructure blue-light-emitting diodes," *Applied Physics Letters,* vol. 64, no. 13, pp. 1687-1689, 1994.

[57] V. L. Colvin, M. C. Schlamp, and A. P. Alivisatos, "Light-emitting diodes made from cadmium selenide nanocrystals and a semiconducting polymer," *Nature,* vol. 370, no. 6488, pp. 354-357, 1994.

[58] X. Wang, X. Yan, W. Li, and K. Sun, "Doped quantum dots for white-light-emitting diodes without reabsorption of multiphase phosphors," *Advanced Materials,* vol. 24, no. 20, pp. 2742-2747, 2012.

[59] J.-S. Li, Y. Tang, Z.-T. Li, X.-R. Ding, L.-S. Rao, and B.-H. Yu, "Effect of quantum dot scattering and absorption on the optical performance of white light-emitting diodes," *IEEE Transactions on Electron Devices,* vol. 65, no. 7, pp. 2877-2884, 2018.

[60] D. Zhou *et al.*, "Conquering aggregation-induced solid-state luminescence quenching of carbon dots through a carbon dots-triggered silica gelation process," *Chemistry of Materials,* vol. 29, no. 4, pp. 1779-1787, 2017.

[61] Y. Shirasaki, G. J. Supran, M. G. Bawendi, and V. Bulović, "Emergence of colloidal quantum-dot light-emitting technologies," *Nature photonics,* vol. 7, no. 1, pp. 13-23, 2013.

[62] S. Sadeghi, B. G. Kumar, R. Melikov, M. M. Aria, H. B. Jalali, and S. Nizamoglu, "Quantum dot white LEDs with high luminous efficiency," *Optica,* vol. 5, no. 7, pp. 793-802, 2018.

[63] E. F. Schubert, *Light-emitting diodes*. Cambridge university press, 2006.

[64] A. Fujishima and K. Honda, "Electrochemical photolysis of water at a semiconductor electrode," *nature,* vol. 238, no. 5358, pp. 37-38, 1972.

[65] S. Yu *et al.*, "Efficient photocatalytic hydrogen evolution with ligand engineered all-inorganic InP and InP/ZnS colloidal quantum dots," *Nature communications,* vol. 9, no. 1, p. 4009, 2018.

[66] C. Liu *et al.*, "Red emissive carbon dot superoxide dismutase nanozyme for bioimaging and ameliorating acute lung injury," *Advanced Functional Materials,* p. 2213856, 2023.

[67] B. Yang, Y. Chen, and J. Shi, "Reactive oxygen species (ROS)-based nanomedicine," *Chemical reviews,* vol. 119, no. 8, pp. 4881-4985, 2019.

[68] Y. Nosaka and A. Y. Nosaka, "Generation and detection of reactive oxygen species in photocatalysis," *Chemical reviews,* vol. 117, no. 17, pp. 11302-11336, 2017.

[69] Z. M. Markovic *et al.*, "Graphene quantum dots as autophagy-inducing photodynamic agents," *Biomaterials,* vol. 33, no. 29, pp. 7084-7092, 2012.

[70] R. Yadav, Y. Kwon, C. Rivaux, C. Saint-Pierre, W. L. Ling, and P. Reiss, "Narrow Near-Infrared Emission from InP QDs Synthesized with Indium (I) Halides and Aminophosphine," *Journal of the American Chemical Society,* vol. 145, no. 10, pp. 5970-5981, 2023.

[71] S. Tamang, C. Lincheneau, Y. Hermans, S. Jeong, and P. Reiss, "Chemistry of InP nanocrystal syntheses," *Chemistry of Materials,* vol. 28, no. 8, pp. 2491-2506, 2016.

[72] S. M. Click and S. J. Rosenthal, "Synthesis, Surface Chemistry, and Fluorescent Properties of InP Quantum Dots," *Chemistry of Materials,* 2023.

[73] J. Zhang, J. Wang, T. Yan, Y. Peng, D. Xu, and D. Deng, "InP/ZnSe/ZnS quantum dots with strong dual emissions: visible excitonic emission and near-infrared surface defect emission and their application in in vitro and in vivo bioimaging," *Journal of Materials Chemistry B,* vol. 5, no. 41, pp. 8152-8160, 2017.

[74] Y. H. Suh *et al.*, "Engineering Core Size of InP Quantum Dot with Incipient ZnS for Blue Emission," *Advanced Optical Materials,* vol. 10, no. 7, p. 2102372, 2022.

[75] M. D. Healy, P. E. Laibinis, P. D. Stupik, and A. R. Barron, "The reaction of indium (III) chloride with tris (trimethylsilyl) phosphine: a novel route to indium phosphide," *Journal of the Chemical Society, Chemical Communications,* no. 6, pp. 359-360, 1989.

[76] O. Micic *et al.*, "Synthesis and characterization of InP, GaP, and GaInP2 quantum dots," *The Journal of Physical Chemistry,* vol. 99, no. 19, pp. 7754-7759, 1995.

[77] H. Van Avermaet *et al.*, "Full-Spectrum InP-Based Quantum Dots with Near-Unity Photoluminescence Quantum Efficiency," *ACS nano,* vol. 16, no. 6, pp. 9701-9712, 2022.

[78] D. Battaglia and X. Peng, "Formation of high quality InP and InAs nanocrystals in a noncoordinating solvent," *Nano Letters,* vol. 2, no. 9, pp. 1027-1030, 2002.

[79] Y. Li *et al.*, "Stoichiometry-controlled InP-based quantum dots: synthesis, photoluminescence, and electroluminescence," *Journal of the American Chemical Society,* vol. 141, no. 16, pp. 6448-6452, 2019.

[80] M. D. Tessier, K. De Nolf, D. Dupont, D. Sinnaeve, J. De Roo, and Z. Hens, "Aminophosphines: a double role in the synthesis of colloidal indium phosphide quantum dots," *Journal of the American Chemical Society,* vol. 138, no. 18, pp. 5923-5929, 2016.

[81] M. D. Tessier, D. Dupont, K. De Nolf, J. De Roo, and Z. Hens, "Economic and Size-Tunable Synthesis of InP/ZnE (E= S, Se) Colloidal Quantum Dots," *Chemistry of Materials,* vol. 27, no. 13, pp. 4893-4898, 2015.

[82] W.-S. Song *et al.*, "Amine-derived synthetic approach to color-tunable InP/ZnS quantum dots with high fluorescent qualities," *Journal of nanoparticle research,* vol. 15, pp. 1-10, 2013.

[83] O. Mićić *et al.*, "Size-dependent spectroscopy of InP quantum dots," *The Journal of Physical Chemistry B,* vol. 101, no. 25, pp. 4904-4912, 1997.

[84] L. Li and P. Reiss, "One-pot synthesis of highly luminescent InP/ZnS nanocrystals without precursor injection," *Journal of the American Chemical Society,* vol. 130, no. 35, pp. 11588-11589, 2008.

[85] B. J. Beberwyck and A. P. Alivisatos, "Ion exchange synthesis of III–V nanocrystals," *Journal of the American Chemical Society,* vol. 134, no. 49, pp. 19977-19980, 2012.

[86] L. De Trizio *et al.*, "Cu3-x P nanocrystals as a material platform for near-infrared plasmonics and cation exchange reactions," *Chemistry of Materials,* vol. 27, no. 3, pp. 1120-1128, 2015.

[87] X. Shan, B. Li, and B. Ji, "Synthesis of wurtzite In and Ga phosphide quantum dots through cation exchange reactions," *Chemistry of Materials,* vol. 33, no. 13, pp. 5223-5232, 2021.

[88] J. A. Gerbec, D. Magana, A. Washington, and G. F. Strouse, "Microwave-enhanced reaction rates for nanoparticle synthesis," *Journal of the American Chemical Society,* vol. 127, no. 45, pp. 15791-15800, 2005.

[89] O. B. Achorn, D. Franke, and M. G. Bawendi, "Seedless continuous injection synthesis of indium phosphide quantum dots as a route to large size and low size dispersity," *Chemistry of Materials,* vol. 32, no. 15, pp. 6532-6539, 2020.

[90] Y. Chen, S. Yu, X.-B. Fan, L.-Z. Wu, and Y. Zhou, "Mechanistic insights into the influence of surface ligands on quantum dots for photocatalysis," *Journal of Materials Chemistry A,* vol. 11, no. 16, pp. 8497-8514, 2023.

[91] N. Kirkwood *et al.*, "Finding and fixing traps in II–VI and III–V colloidal quantum dots: the importance of Z-type ligand passivation," *Journal of the American Chemical Society,* vol. 140, no. 46, pp. 15712-15723, 2018.

[92] I. Lee *et al.*, "Photodynamic treatment of multidrug-resistant bacterial infection using indium phosphide quantum dots," *Biomaterials Science,* vol. 10, no. 24, pp. 7149-7161, 2022.

[93] H. Virieux *et al.*, "InP/ZnS nanocrystals: coupling NMR and XPS for fine surface and interface description," *Journal of the American Chemical Society,* vol. 134, no. 48, pp. 19701-19708, 2012.

[94] M. D. Tessier *et al.*, "Interfacial oxidation and photoluminescence of InP-based core/shell quantum dots," *Chemistry of Materials,* vol. 30, no. 19, pp. 6877-6883, 2018.

[95] A. Cros-Gagneux, F. Delpech, C. Nayral, A. Cornejo, Y. Coppel, and B. Chaudret, "Surface chemistry of InP quantum dots: a comprehensive study," *Journal of the American Chemical Society,* vol. 132, no. 51, pp. 18147-18157, 2010.

[96] O. I. Mićić, J. Sprague, Z. Lu, and A. J. Nozik, "Highly efficient band-edge emission from InP quantum dots," *Applied Physics Letters,* vol. 68, no. 22, pp. 3150-3152, 1996.

[97] S. Adam *et al.*, "The effect of nanocrystal surface structure on the luminescence properties: Photoemission study of HF-etched InP nanocrystals," *The Journal of chemical physics,* vol. 123, no. 8, p. 084706, 2005.

[98] T.-G. Kim *et al.*, "Trap passivation in indium-based quantum dots through surface fluorination: mechanism and applications," *ACS nano,* vol. 12, no. 11, pp. 11529-11540, 2018.

[99] E. Cho, T. Kim, S.-m. Choi, H. Jang, K. Min, and E. Jang, "Optical characteristics of the surface defects in InP colloidal quantum dots for highly efficient light-

emitting applications," *ACS Applied Nano Materials,* vol. 1, no. 12, pp. 7106-7114, 2018.

[100] E. Jang, Y. Kim, Y.-H. Won, H. Jang, and S.-M. Choi, "Environmentally friendly InP-based quantum dots for efficient wide color gamut displays," *ACS Energy Letters,* vol. 5, no. 4, pp. 1316-1327, 2020.

[101] S. Haubold, M. Haase, A. Kornowski, and H. Weller, "Strongly luminescent InP/ZnS core–shell nanoparticles," *ChemPhysChem,* vol. 2, no. 5, pp. 331-334, 2001.

[102] R. Xie, D. Battaglia, and X. Peng, "Colloidal InP nanocrystals as efficient emitters covering blue to near-infrared," *Journal of the American Chemical Society,* vol. 129, no. 50, pp. 15432-15433, 2007.

[103] J. Lim *et al.*, "InP@ ZnSeS, core@ composition gradient shell quantum dots with enhanced stability," *Chemistry of Materials,* vol. 23, no. 20, pp. 4459-4463, 2011.

[104] O. I. Mićić, B. B. Smith, and A. J. Nozik, "Core− shell quantum dots of lattice-matched ZnCdSe2 shells on InP cores: experiment and theory," *The Journal of Physical Chemistry B,* vol. 104, no. 51, pp. 12149-12156, 2000.

[105] K. Wu, N. Song, Z. Liu, H. Zhu, W. Rodríguez-Córdoba, and T. Lian, "Interfacial charge separation and recombination in InP and quasi-type II InP/CdS core/shell quantum dot-molecular acceptor complexes," *The Journal of Physical Chemistry A,* vol. 117, no. 32, pp. 7561-7570, 2013.

[106] H. Bahmani Jalali *et al.*, "Effective neural photostimulation using indium-Based type-II quantum dots," *ACS nano,* vol. 12, no. 8, pp. 8104-8114, 2018.

[107] S. Kim *et al.*, "Reverse Type-I ZnSe/InP/ZnS Core/Shell/Shell Nanocrystals: Cadmium-Free Quantum Dots for Visible Luminescence," *Small,* vol. 7, no. 1, pp. 70-73, 2011.

[108] S. Mei *et al.*, "Color-tunable optical properties of cadmium-free transition metal ions doped InP/ZnS quantum dots," *Journal of Luminescence,* vol. 212, pp. 264-270, 2019.

[109] M. Lim *et al.*, "Synthesis of far-red-and near-infrared-emitting Cu-doped InP/ZnS (core/shell) quantum dots with controlled doping steps and their surface functionalization for bioconjugation," *Nanoscale,* vol. 11, no. 21, pp. 10463-10471, 2019.

[110] X. Wei *et al.*, "Optical and Morphological Properties of Single-Phased and Dual-Emissive InP/ZnS Quantum Dots via Transition Metallic and Inorganic Ions," *Langmuir,* vol. 36, no. 34, pp. 10244-10250, 2020.

[111] T. Chen *et al.*, "Cytotoxicity of InP/ZnS quantum dots with different surface functional groups toward two lung-derived cell lines," *Frontiers in pharmacology,* vol. 9, p. 763, 2018.

[112] K.-T. Yong *et al.*, "Imaging pancreatic cancer using bioconjugated InP quantum dots," *ACS nano,* vol. 3, no. 3, pp. 502-510, 2009.

[113] H. Bahmani Jalali *et al.*, "Biocompatible quantum funnels for neural photostimulation," *Nano letters,* vol. 19, no. 9, pp. 5975-5981, 2019.

[114] G. Liu, R. Mazzaro, Y. Wang, H. Zhao, and A. Vomiero, "High efficiency sandwich structure luminescent solar concentrators based on colloidal quantum dots," *Nano Energy,* vol. 60, pp. 119-126, 2019.

[115] F. Meinardi *et al.*, "Highly efficient large-area colourless luminescent solar concentrators using heavy-metal-free colloidal quantum dots," *Nature nanotechnology,* vol. 10, no. 10, pp. 878-885, 2015.

[116] A. L. Rogach *et al.*, "Light-emitting diodes with semiconductor nanocrystals," *Angewandte Chemie International Edition,* vol. 47, no. 35, pp. 6538-6549, 2008.
[117] Y. Shirasaki, G. J. Supran, M. G. Bawendi, and V. Bulović, "Emergence of colloidal quantum-dot light-emitting technologies," *Nature Photonics,* vol. 7, no. 1, p. 13, 2013.
[118] S. Sadeghi *et al.*, "High quality quantum dots polymeric films as color converters for smart phone display technology," *Materials Research Express,* vol. 6, no. 3, p. 035015, 2018.
[119] R. P. Sabatini *et al.*, "Temperature-induced self-compensating defect traps and gain thresholds in colloidal quantum dots," *ACS nano,* vol. 13, no. 8, pp. 8970-8976, 2019.
[120] Y. Wang *et al.*, "Robust whispering-gallery-mode microbubble lasers from colloidal quantum dots," *Nano letters,* vol. 17, no. 4, pp. 2640-2646, 2017.
[121] C. Murray, D. J. Norris, and M. G. Bawendi, "Synthesis and characterization of nearly monodisperse CdE (E= sulfur, selenium, tellurium) semiconductor nanocrystallites," *Journal of the American Chemical Society,* vol. 115, no. 19, pp. 8706-8715, 1993.
[122] Y. Yin and D. Talapin, "The chemistry of functional nanomaterials," *Chemical Society Reviews,* vol. 42, no. 7, pp. 2484-2487, 2013.
[123] X. Dai *et al.*, "Solution-processed, high-performance light-emitting diodes based on quantum dots," *Nature,* vol. 515, no. 7525, pp. 96-99, 2014.
[124] M. Han, H. B. Jalali, E. Yildiz, M. H. Qureshi, A. Şahin, and S. Nizamoglu, "Photovoltaic neurointerface based on aluminum antimonide nanocrystals," *Communications Materials,* vol. 2, no. 1, pp. 1-10, 2021.
[125] Y. Zhang, Y. Li, and X.-P. Yan, "Photoactivated CdTe/CdSe quantum dots as a near infrared fluorescent probe for detecting biothiols in biological fluids," *Analytical chemistry,* vol. 81, no. 12, pp. 5001-5007, 2009.
[126] C. M. Gentle, Y. Wang, T. N. Haddock, C. P. Dykstra, and R. M. van der Veen, "Internal Atomic-Scale Structure Determination and Band Alignment of II–VI Quantum Dot Heterostructures," *The Journal of Physical Chemistry C,* vol. 124, no. 6, pp. 3895-3904, 2020.
[127] T. Long, J. Cao, and Z.-J. Jiang, "Predictable spectroscopic properties of type-II ZnTe/CdSe nanocrystals and electron/hole quenching," *Physical Chemistry Chemical Physics,* vol. 21, no. 10, pp. 5824-5833, 2019.
[128] N. Ca *et al.*, "Photoluminescence properties of CdTe/CdTeSe/CdSe core/alloyed/shell type-II quantum dots," *Journal of Alloys and Compounds,* vol. 787, pp. 823-830, 2019.
[129] X. Jin *et al.*, "Bright alloy type-II quantum dots and their application to light-emitting diodes," *Journal of colloid and interface science,* vol. 510, pp. 376-383, 2018.
[130] N. Chen *et al.*, "The cytotoxicity of cadmium-based quantum dots," *Biomaterials,* vol. 33, no. 5, pp. 1238-1244, 2012.
[131] A. M. Derfus, W. C. Chan, and S. N. Bhatia, "Probing the cytotoxicity of semiconductor quantum dots," *Nano letters,* vol. 4, no. 1, pp. 11-18, 2004.
[132] C. Kirchner *et al.*, "Cytotoxicity of colloidal CdSe and CdSe/ZnS nanoparticles," *Nano letters,* vol. 5, no. 2, pp. 331-338, 2005.

[133] J. Bang *et al.*, "ZnTe/ZnSe (core/shell) type-II quantum dots: their optical and photovoltaic properties," *Chemistry of Materials,* vol. 22, no. 1, pp. 233-240, 2010.
[134] S. Xu, J. Ziegler, and T. Nann, "Rapid synthesis of highly luminescent InP and InP/ZnS nanocrystals," *Journal of Materials Chemistry,* vol. 18, no. 23, pp. 2653-2656, 2008.
[135] H. Bahmani Jalali *et al.*, "Biocompatible Quantum Funnels for Neural Photostimulation," *Nano Letters,* vol. 19, no. 9, pp. 5975-5981, 2019/09/11 2019, doi: 10.1021/acs.nanolett.9b01697.
[136] B. G. Kumar *et al.*, "Structural control of InP/ZnS core/shell quantum dots enables high-quality white LEDs," *Nanotechnology,* vol. 29, no. 34, p. 345605, 2018.
[137] A. M. Smith, A. M. Mohs, and S. Nie, "Tuning the optical and electronic properties of colloidal nanocrystals by lattice strain," *Nature nanotechnology,* vol. 4, no. 1, pp. 56-63, 2009.
[138] O. Karatum, H. B. Jalali, S. Sadeghi, R. Melikov, S. B. Srivastava, and S. Nizamoglu, "Light-emitting devices based on type-II InP/ZnO quantum dots," *ACS Photonics,* vol. 6, no. 4, pp. 939-946, 2019.
[139] Y. Shirasaki, G. J. Supran, M. G. Bawendi, and V. Bulovic, "Emergence of colloidal quantum-dot light-emitting technologies," *Nature Photonics,* vol. 7, no. 1, pp. 13-23, Jan 2013, doi: 10.1038/nphoton.2012.328.
[140] X. L. Dai *et al.*, "Solution-processed, high-performance light-emitting diodes based on quantum dots," *Nature,* vol. 515, no. 7525, pp. 96-99, Nov 2014, doi: 10.1038/nature13829.
[141] J. Liu *et al.*, "Synthesis of relatively monodisperse ZnO nanocrystals from a precursor zinc 2, 4-pentanedionate," *Materials Letters,* vol. 61, no. 13, pp. 2837-2840, 2007.
[142] Y. Barak, I. Meir, A. Shapiro, Y. Jang, and E. Lifshitz, "Fundamental properties in colloidal quantum dots," *Advanced Materials,* vol. 30, no. 41, p. 1801442, 2018.
[143] S. L. Lin, N. Pradhan, Y. J. Wang, and X. G. Peng, "High quality ZnSe and ZnS nanocrystals formed by activating zinc carboxylate precursors," *Nano Letters,* vol. 4, no. 11, pp. 2261-2264, Nov 2004, doi: 10.1021/nl048650e.
[144] S. Rawalekar, S. Kaniyankandy, S. Verma, and H. N. Ghosh, "Effect of Surface States on Charge-Transfer Dynamics in Type II CdTe/ZnTe Core-Shell Quantum Dots: A Femtosecond Transient Absorption Study," *Journal of Physical Chemistry C,* vol. 115, no. 25, pp. 12335-12342, Jun 2011, doi: 10.1021/jp202916v.
[145] O. Glatter, *Scattering methods and their application in colloid and interface science*. Elsevier, 2018.
[146] G. Fritz and O. Glatter, "Structure and interaction in dense colloidal systems: evaluation of scattering data by the generalized indirect Fourier transformation method," *Journal of Physics: Condensed Matter,* vol. 18, no. 36, p. S2403, 2006.
[147] G. Fritz and A. Bergmann, "Interpretation of small-angle scattering data of inhomogeneous ellipsoids," *Journal of applied crystallography,* vol. 37, no. 5, pp. 815-822, 2004.
[148] G. Cantele, G. Piacente, D. Ninno, and G. Iadonisi, "Optical anisotropy of ellipsoidal quantum dots," *Physical Review B,* vol. 66, no. 11, p. 113308, 2002.

[149] M. van den Broek and F. Peeters, "Confined states in two-dimensional flat elliptic quantum dots and elliptic quantum wires," *Physica E: Low-dimensional Systems and Nanostructures,* vol. 11, no. 4, pp. 345-355, 2001.

[150] R. T. Lechner *et al.*, "Crystal phase transitions in the shell of PbS/CdS core/shell nanocrystals influences photoluminescence intensity," *Chemistry of materials,* vol. 26, no. 20, pp. 5914-5922, 2014.

[151] H. Virieux *et al.*, "InP/ZnS nanocrystals: coupling NMR and XPS for fine surface and interface description," *Journal of the American Chemical Society,* vol. 134, no. 48, pp. 19701-19708, 2012.

[152] L. Kazmerski, P. Ireland, P. Sheldon, T. Chu, S. Chu, and C. Lin, "Comparison of low-temperature oxides on polycrystalline InP by AES, SIMS, and XPS," *Journal of Vacuum Science and Technology,* vol. 17, no. 5, pp. 1061-1066, 1980.

[153] F. Pietra *et al.*, "Tuning the lattice parameter of In X Zn Y P for highly luminescent lattice-matched core/shell quantum dots," *Acs Nano,* vol. 10, no. 4, pp. 4754-4762, 2016.

[154] L. Xi *et al.*, "Effect of zinc incorporation on the performance of red light emitting InP core nanocrystals," *Inorganic chemistry,* vol. 55, no. 17, pp. 8381-8386, 2016.

[155] D. Granada-Ramirez *et al.*, "Chemical synthesis and optical, structural, and surface characterization of InP-In2O3 quantum dots," *Applied surface science,* vol. 530, p. 147294, 2020.

[156] P. Mohapatra, M. X. Dung, J.-K. Choi, S.-H. Jeong, and H.-D. Jeong, "Effects of curing temperature on the optical and charge trap properties of InP quantum dot thin films," *Bulletin of the Korean Chemical Society,* vol. 32, no. 1, pp. 263-272, 2011.

[157] O. Karatum *et al.*, "Quantum dot and electron acceptor nano-heterojunction for photo-induced capacitive charge-transfer," *Scientific reports,* vol. 11, no. 1, pp. 1-9, 2021.

[158] J. Moulder, W. Stickle, P. Sobol, and K. Bomben, "A reference book of standard spectra for identification and interpretation of XPS data," *Perkin-Elmer Corporation,* 1995.

[159] D. Gao, Z. Zhang, J. Fu, Y. Xu, J. Qi, and D. Xue, "Room temperature ferromagnetism of pure ZnO nanoparticles," *Journal of Applied Physics,* vol. 105, no. 11, p. 113928, 2009.

[160] Y.-C. Liang and C.-C. Wang, "Surface crystal feature-dependent photoactivity of ZnO–ZnS composite rods via hydrothermal sulfidation," *RSC advances,* vol. 8, no. 9, pp. 5063-5070, 2018.

[161] Y. I. Choi *et al.*, "Fabrication of ZnO, ZnS, Ag-ZnS, and Au-ZnS microspheres for photocatalytic activities, CO oxidation and 2-hydroxyterephthalic acid synthesis," *Journal of Alloys and Compounds,* vol. 675, pp. 46-56, 2016.

[162] T. Kim, S. W. Kim, M. Kang, and S.-W. Kim, "Large-scale synthesis of InPZnS alloy quantum dots with dodecanethiol as a composition controller," *The journal of physical chemistry letters,* vol. 3, no. 2, pp. 214-218, 2012.

[163] I. Baylam, M. Cizmeciyan, N. Kakenov, C. Kocabas, and A. Sennaroglu, "Ultrafast spectroscopy of voltage reconfigurable graphene saturable absorbers in the visible and near infrared," *2D Materials,* vol. 6, no. 3, p. 035013, 2019.

[164] H. Zhu, N. Song, W. Rodríguez-Córdoba, and T. Lian, "Wave function engineering for efficient extraction of up to nineteen electrons from one

CdSe/CdS quasi-type II quantum dot," *Journal of the American Chemical Society,* vol. 134, no. 9, pp. 4250-4257, 2012.

[165] S. Rawalekar, S. Kaniyankandy, S. Verma, and H. N. Ghosh, "Ultrafast Charge Carrier Relaxation and Charge Transfer Dynamics of CdTe/CdS Core− Shell Quantum Dots as Studied by Femtosecond Transient Absorption Spectroscopy," *The Journal of Physical Chemistry C,* vol. 114, no. 3, pp. 1460-1466, 2010.

[166] A. Dutta, R. Bera, A. Ghosh, and A. Patra, "Ultrafast carrier dynamics of photo-induced Cu-doped CdSe nanocrystals," *The Journal of Physical Chemistry C,* vol. 122, no. 29, pp. 16992-17000, 2018.

[167] P. Peng, B. Sadtler, A. P. Alivisatos, and R. J. Saykally, "Exciton dynamics in CdS− Ag2S nanorods with tunable composition probed by ultrafast transient absorption spectroscopy," *The Journal of Physical Chemistry C,* vol. 114, no. 13, pp. 5879-5885, 2010.

[168] V. Klimov, S. Hunsche, and H. Kurz, "Biexciton effects in femtosecond nonlinear transmission of semiconductor quantum dots," *Physical Review B,* vol. 50, no. 11, p. 8110, 1994.

[169] V. I. Klimov, D. McBranch, C. Leatherdale, and M. Bawendi, "Electron and hole relaxation pathways in semiconductor quantum dots," *Physical Review B,* vol. 60, no. 19, p. 13740, 1999.

[170] C. Burda, S. Link, T. Green, and M. El-Sayed, "New transient absorption observed in the spectrum of colloidal CdSe nanoparticles pumped with high-power femtosecond pulses," *The Journal of Physical Chemistry B,* vol. 103, no. 49, pp. 10775-10780, 1999.

[171] J. C. McDonald and G. M. Whitesides, "Poly (dimethylsiloxane) as a material for fabricating microfluidic devices," *Accounts of chemical research,* vol. 35, no. 7, pp. 491-499, 2002.

[172] D. Cai, A. Neyer, R. Kuckuk, and H. Heise, "Optical absorption in transparent PDMS materials applied for multimode waveguides fabrication," *Optical materials,* vol. 30, no. 7, pp. 1157-1161, 2008.

[173] E. F. Schubert, T. Gessmann, and J. K. Kim, "Light emitting diodes," *Kirk-Othmer Encyclopedia of Chemical Technology,* 2000.

[174] K. Gungor, J. Du, and V. I. Klimov, "General Trends in the Performance of Quantum Dot Luminescent Solar Concentrators (LSCs) Revealed Using the “Effective LSC Quality Factor”," *ACS Energy Letters,* vol. 7, no. 5, pp. 1741-1749, 2022.

[175] E. H. Sargent, "Colloidal quantum dot solar cells," *Nature photonics,* vol. 6, no. 3, pp. 133-135, 2012.

[176] J. Zhou, Y. Liu, J. Tang, and W. Tang, "Surface ligands engineering of semiconductor quantum dots for chemosensory and biological applications," *Materials Today,* vol. 20, no. 7, pp. 360-376, 2017.

[177] Q. Wu *et al.*, "Efficient Tandem Quantum-Dot LEDs Enabled by An Inorganic Semiconductor-Metal-Dielectric Interconnecting Layer Stack," *Advanced Materials,* vol. 34, no. 4, p. 2108150, 2022.

[178] F. Cao, S. Wang, F. Wang, Q. Wu, D. Zhao, and X. Yang, "A layer-by-layer growth strategy for large-size InP/ZnSe/ZnS core–shell quantum dots enabling high-efficiency light-emitting diodes," *Chemistry of Materials,* vol. 30, no. 21, pp. 8002-8007, 2018.

[179] F. Sousa Velosa, H. Van Avermaet, P. Schiettecatte, L. Mingabudinova, P. Geiregat, and Z. Hens, "State Filling and Stimulated Emission by Colloidal InP/ZnSe Core/Shell Quantum Dots," *Advanced Optical Materials,* vol. 10, no. 18, p. 2200328, 2022.

[180] H. Bahmani Jalali, R. Melikov, S. Sadeghi, and S. Nizamoglu, "Excitonic energy transfer within InP/ZnS quantum dot Langmuir–Blodgett assemblies," *The Journal of Physical Chemistry C,* vol. 122, no. 22, pp. 11616-11622, 2018.

[181] N. Pradhan and X. Peng, "Efficient and color-tunable Mn-doped ZnSe nanocrystal emitters: control of optical performance via greener synthetic chemistry," *Journal of the American Chemical Society,* vol. 129, no. 11, pp. 3339-3347, 2007.

[182] D. J. Norris, N. Yao, F. T. Charnock, and T. A. Kennedy, "High-quality manganese-doped ZnSe nanocrystals," *Nano Letters,* vol. 1, no. 1, pp. 3-7, 2001.

[183] S. Wageh, A. A. Al-Ghamdi, A. Al-Zahrani, and H. Driss, "High quantum yield Cu doped CdSe quantum dots," *Materials Research Express,* vol. 6, no. 8, p. 0850d4, 2019.

[184] F. V. Mikulec, M. Kuno, M. Bennati, D. A. Hall, R. G. Griffin, and M. G. Bawendi, "Organometallic synthesis and spectroscopic characterization of manganese-doped CdSe nanocrystals," *Journal of the American Chemical Society,* vol. 122, no. 11, pp. 2532-2540, 2000.

[185] B. B. Srivastava *et al.*, "Highly luminescent Mn-doped ZnS nanocrystals: gram-scale synthesis," *The Journal of Physical Chemistry Letters,* vol. 1, no. 9, pp. 1454-1458, 2010.

[186] R. Sahraei, F. Mohammadi, E. Soheyli, and M. Roushani, "Synthesis and photoluminescence properties of Ru-doped ZnS quantum dots," *Journal of Luminescence,* vol. 187, pp. 421-427, 2017.

[187] V. K. Sharma, B. Guzelturk, T. Erdem, Y. Kelestemur, and H. V. Demir, "Tunable white-light-emitting Mn-doped ZnSe nanocrystals," *ACS applied materials & interfaces,* vol. 6, no. 5, pp. 3654-3660, 2014.

[188] X. Yang *et al.*, "Full visible range covering InP/ZnS nanocrystals with high photometric performance and their application to white quantum dot light-emitting Diodes," *Advanced Materials,* vol. 24, no. 30, pp. 4180-4185, 2012.

[189] H. B. Jalali, S. Sadeghi, I. B. Dogru Yuksel, A. Onal, and S. Nizamoglu, "Past, present and future of indium phosphide quantum dots," *Nano Research,* vol. 15, no. 5, pp. 4468-4489, 2022.

[190] D. Majumdar, T. Maiyalagan, and Z. Jiang, "Recent progress in ruthenium oxide-based composites for supercapacitor applications," *ChemElectroChem,* vol. 6, no. 17, pp. 4343-4372, 2019.

[191] S. Korkmaz, İ. A. Kariper, C. Karaman, and O. Karaman, "MWCNT/Ruthenium hydroxide aerogel supercapacitor production and investigation of electrochemical performances," *Scientific reports,* vol. 12, no. 1, pp. 1-8, 2022.

[192] P. Konda *et al.*, "Photodynamic therapy of melanoma with new, structurally similar, NIR-absorbing ruthenium (II) complexes promotes tumor growth control via distinct hallmarks of immunogenic cell death," *American Journal of Cancer Research,* vol. 12, no. 1, p. 210, 2022.

[193] M. Zhang *et al.*, "Copper Ion and Ruthenium Complex Codoped Polydopamine Nanoparticles for Magnetic Resonance/Photoacoustic Tomography Imaging-Guided Photodynamic/Photothermal Dual-Mode Therapy," *ACS Applied Bio Materials,* vol. 5, no. 5, pp. 2365-2376, 2022.

[194] O. Karatum, E. Yildiz, H. N. Kaleli, A. Sahin, B. Ulgut, and S. Nizamoglu, "RuO2 Supercapacitor Enables Flexible, Safe, and Efficient Optoelectronic Neural Interface," *Advanced Functional Materials,* vol. 32, no. 31, p. 2109365, 2022.

[195] O. Karatum, H. N. Kaleli, G. O. Eren, A. Sahin, and S. Nizamoglu, "Electrical stimulation of neurons with quantum dots via near-infrared light," *Acs Nano,* vol. 16, no. 5, pp. 8233-8243, 2022.

[196] A. V. Stavitskaya *et al.*, "Ru/CdS Quantum Dots Templated on Clay Nanotubes as Visible-Light-Active Photocatalysts: Optimization of S/Cd Ratio and Ru Content," *Chemistry–A European Journal,* vol. 26, no. 57, pp. 13085-13092, 2020.

[197] S. Taniguchi and M. Green, "The synthesis of CdTe/ZnS core/shell quantum dots using molecular single-source precursors," *Journal of Materials Chemistry C,* vol. 3, no. 32, pp. 8425-8433, 2015.

[198] N. A. Hamizi *et al.*, "Lattice strain analysis of a Mn-doped CdSe QD system using crystallography techniques," *Processes,* vol. 7, no. 10, p. 639, 2019.

[199] W.-C. Kwak, Y.-M. Sung, T. G. Kim, and W.-S. Chae, "Synthesis of Mn-doped zinc blende CdSe nanocrystals," *Applied physics letters,* vol. 90, no. 17, p. 173111, 2007.

[200] J. Jasinski *et al.*, "Rapid oxidation of InP nanoparticles in air," *Solid state communications,* vol. 141, no. 11, pp. 624-627, 2007.

[201] G. O. Eren *et al.*, "Cadmium-free and efficient type-II InP/ZnO/ZnS quantum dots and their application for LEDs," *ACS Applied Materials & Interfaces,* vol. 13, no. 27, pp. 32022-32030, 2021.

[202] P. Sakthivel, S. Muthukumaran, and M. Ashokkumar, "Structural, band gap and photoluminescence behaviour of Mn-doped ZnS quantum dots annealed under Ar atmosphere," *Journal of Materials Science: Materials in Electronics,* vol. 26, pp. 1533-1542, 2015.

[203] H. Li *et al.*, "Silver ion-doped CdTe quantum dots as fluorescent probe for Hg 2+ detection," *RSC advances,* vol. 10, no. 64, pp. 38965-38973, 2020.

[204] S. Jung *et al.*, "Enhancement of photoluminescence quantum yield and stability in CsPbBr3 perovskite quantum dots by trivalent doping," *Nanomaterials,* vol. 10, no. 4, p. 710, 2020.

[205] S. K. Panda, S. G. Hickey, H. V. Demir, and A. Eychmuller, "Bright white-light emitting manganese and copper co-doped ZnSe quantum dots," *Angewandte Chemie International Edition,* vol. 50, no. 19, pp. 4432-4436, 2011.

[206] K. Li, J. Shao, and D. Xue, "Calculation of impurity energy levels of transition metal ions in inorganic crystals based on electronegativity," *Materials Research Innovations,* vol. 17, no. 4, pp. 218-223, 2013.

[207] L. Liu, Q. Peng, and Y. Li, "An effective oxidation route to blue emission CdSe quantum dots," *Inorganic chemistry,* vol. 47, no. 8, pp. 3182-3187, 2008.

[208] M. E. Mundy, F. W. Eagle, K. E. Hughes, D. R. Gamelin, and B. M. Cossairt, "Synthesis and spectroscopy of emissive, surface-modified, copper-doped indium phosphide nanocrystals," *ACS Materials Letters,* vol. 2, no. 6, pp. 576-581, 2020.

[209] E. F. Schubert, *Light-Emitting Diodes (2006)*. E. Fred Schubert, 2006.

[210] A. W. Wills *et al.*, "Synthesis and characterization of Al-and In-doped CdSe nanocrystals," *Journal of Materials Chemistry,* vol. 22, no. 13, pp. 6335-6342, 2012.

[211] T. N. Pham, T. Sooknoi, S. P. Crossley, and D. E. Resasco, "Ketonization of carboxylic acids: mechanisms, catalysts, and implications for biomass conversion," *Acs Catalysis,* vol. 3, no. 11, pp. 2456-2473, 2013.

[212] R. Mahfouz, M. Siddiqui, S. A. Al-Ahmari, and W. Alkayali, "Kinetic Analysis of Thermal Decomposition of Unirradiated and γ-Irradiated Tris (ACEtylacetonato)-Ruthenium (III)[Ru (acac) 3]," *Progress in reaction Kinetics and Mechanism,* vol. 32, no. 1, pp. 1-27, 2007.

[213] D. J. Morgan, "Resolving ruthenium: XPS studies of common ruthenium materials," *Surface and Interface Analysis,* vol. 47, no. 11, pp. 1072-1079, 2015.

[214] K. Kim and N. Winograd, "X-Ray photoelectron spectroscopic studies of ruthenium-oxygen surfaces," *Journal of Catalysis,* vol. 35, no. 1, pp. 66-72, 1974.

[215] W. Yang, W. Zhang, G. Zhang, J. Zhu, G. He, and R. Guo, "Super-high color rendering properties of color temperature tunable white LEDs based on high quality InP/ZnS quantum dots via myristic acid passivation and Ag doping," *Optics Communications,* vol. 418, pp. 46-50, 2018.

[216] Q. Wu *et al.*, "Quasi-Shell-Growth Strategy Achieves Stable and Efficient Green InP Quantum Dot Light-Emitting Diodes," *Advanced Science,* vol. 9, no. 21, p. 2200959, 2022.

[217] Y. Xu *et al.*, "Preparation of Highly Stable and Photoluminescent Cadmium-Free InP/GaP/ZnS Core/Shell Quantum Dots and Application to Quantitative Immunoassay," *Particle & Particle Systems Characterization,* vol. 37, no. 3, p. 1900441, 2020.

[218] K. Bush *et al.*, "Tackling antibiotic resistance," *Nature Reviews Microbiology,* vol. 9, no. 12, pp. 894-896, 2011.

[219] P. Stewart and T. Bjarnsholt, "Risk factors for chronic biofilm-related infection associated with implanted medical devices," *Clinical Microbiology and Infection,* vol. 26, no. 8, pp. 1034-1038, 2020.

[220] E. Banin, D. Hughes, and O. P. Kuipers, "Bacterial pathogens, antibiotics and antibiotic resistance," *FEMS microbiology reviews,* vol. 41, no. 3, pp. 450-452, 2017.

[221] S. Gangadoo *et al.*, "Probing nanoscale interactions of antimicrobial zinc oxide quantum dots on bacterial and fungal cell surfaces," *Advanced Materials Interfaces,* vol. 9, no. 3, p. 2101484, 2022.

[222] D. A. Ananth *et al.*, "Antibacterial potential of rutin conjugated with thioglycolic acid capped cadmium telluride quantum dots (TGA-CdTe QDs)," *Spectrochimica acta part A: molecular and biomolecular spectroscopy,* vol. 138, pp. 684-692, 2015.

[223] S. Musić, A. Šarić, and S. Popović, "Formation of nanosize ZnO particles by thermal decomposition of zinc acetylacetonate monohydrate," *Ceramics International,* vol. 36, no. 3, pp. 1117-1123, 2010.

[224] H. J. Yun, T. Paik, M. E. Edley, J. B. Baxter, and C. B. Murray, "Enhanced charge transfer kinetics of CdSe quantum dot-sensitized solar cell by inorganic ligand exchange treatments," *ACS applied materials & interfaces,* vol. 6, no. 5, pp. 3721-3728, 2014.

[225] M. P. Murphy *et al.*, "Guidelines for measuring reactive oxygen species and oxidative damage in cells and in vivo," *Nature Metabolism,* vol. 4, no. 6, pp. 651-662, 2022.

[226] Y. Li, W. Zhang, J. Niu, and Y. Chen, "Mechanism of photogenerated reactive oxygen species and correlation with the antibacterial properties of engineered metal-oxide nanoparticles," *ACS nano,* vol. 6, no. 6, pp. 5164-5173, 2012.

[227] A. A. Boghossian *et al.*, "Application of nanoparticle antioxidants to enable hyperstable chloroplasts for solar energy harvesting," *Advanced Energy Materials,* vol. 3, no. 7, pp. 881-893, 2013.

[228] X. Zhang *et al.*, "A bifunctional hydrogel incorporated with CuS@ MoS2 microspheres for disinfection and improved wound healing," *Chemical Engineering Journal,* vol. 382, p. 122849, 2020.

[229] A. Basu *et al.*, "Photocatalytic disinfection of extended-spectrum beta-lactamase producing Escherichia coli using Alumina/ZnO heterostructures," *Journal of Environmental Chemical Engineering,* vol. 9, no. 6, p. 106334, 2021.

[230] Y. Liu *et al.*, "Inorganic ligands-mediated hole attraction and surface structural reorganization in InP/ZnS QD photocatalysts studied via ultrafast visible and midinfrared spectroscopies," *Science China Materials,* vol. 65, no. 9, pp. 2529-2539, 2022.

[231] L. Akselrud and Y. Grin, "WinCSD: software package for crystallographic calculations (Version 4)," *Journal of Applied Crystallography,* vol. 47, no. 2, pp. 803-805, 2014.